UC Riverside
UC Riverside Electronic Theses and Dissertations

Title
Study of Phonon Engineering Using Neutron Scattering

Permalink
https://escholarship.org/uc/item/89x1q0kp

Author
Chen, Shuonan

Publication Date
2022

Copyright Information
This work is made available under the terms of a Creative Commons Attribution License, availalbe at https://creativecommons.org/licenses/by/4.0/

Peer reviewed|Thesis/dissertation

eScholarship.org Powered by the California Digital Library
University of California

UNIVERSITY OF CALIFORNIA
RIVERSIDE

Study of Phonon Engineering Using Neutron Scattering

A Dissertation submitted in partial satisfaction
of the requirements for the degree of

Doctor of Philosophy

in

Mechanical Engineering

by

Shuonan Chen

December 2022

Dissertation Committee:
  Dr. Chen Li, Chairperson
  Dr. Lorenzo Mangolini
  Dr. Tom Stahovich

Copyright by
Shuonan Chen
2022

The Dissertation of Shuonan Chen is approved:

Committee Chairperson

University of California, Riverside

ACKNOWLEDGEMENTS

I would like to express first my profound gratitude to my advisor, Prof. Chen Li for his continuous guidance and support during my Ph.D. studies. I would not complete my Ph.D. nor find a nice job without his help. I am also very grateful to all our collaborators, Prof. Lorenzo Mangolini, Dr. Devin Coleman, Joseph Schwan, Dr. Tao Hong, Dr. Douglas L. Abernathy, Dr. Arnab Banerjee, Dr. Luke L. Daemen, Dr. Qiang Zhang, Dr. Javier E. Garay, and Dr. Fariborz Kargar. I also would like to express my gratitude to my committee members, Prof. Lorenzo Mangolini and Prof. Tom Stahovich.

I am also grateful to the University of California, Riverside where I lived and studied, the Oak Ridge National Laboratory where I carried out most of my experiments, and all my groupmates for all their help and collaborations: Bin Wei, Yuemei Zhang, Qingan Cai, Qiyang Sun, Songrui Hou, and Yaokun Su.

Last but not least, I express my most profound appreciation for my family, and all those pushing me forward, yet there with open arms when I fall back.

The text of this dissertation, in part, is a reprint of the material as it appears in Shuonan Chen, et al. Giant Low-Temperature Anharmonicity in Silicon Nanocrystals. *Phys. Rev. Mater.* **2020**, *4* (5), 56001, and Shuonan Chen, et al. Distinct Acoustic and Optical Phonon Dependences on Particle Size, Oxidation, and Temperature in Silicon Nanocrystals. *J. Phys. Chem. C* **2022**, *126* (30), 12704–12711. The co-author Chen Li listed in those publications directed and supervised the research which forms the basis for this dissertation.

ABSTRACT OF THE DISSERTATION

Study of Phonon Engineering Using Neutron Scattering

by

Shuonan Chen

Doctor of Philosophy, Graduate Program in Mechanical Engineering
University of California, Riverside, December 2022
Dr. Chen Li, Chairperson

Phonon, a quantized lattice vibration, plays an important role in the materials' physical and mechanical properties. This makes investigations on phonon dynamics an indispensable subject for better understanding the physical world. For decades, people have been seeking ways to manipulate phonon dynamics, which are closely related to atomic structures and electromagnetic properties of materials, for the development of novel materials with desired properties and more insights into fundamental physics. This dissertation discusses the studies of phonon engineering in spatially confined silicon systems, which have been widely used in the biomedical filed and have great potential applications in the optoelectronic industry, as well as bulk sapphire systems using inelastic neutron scatterings.

The dissertation starts with introducing the basic information about phonon dynamics and neutron scatterings which are the two primary subjects of my graduate research. In Chapters 2 to 4, the inelastic neutron scattering experiments and discussions on the effects of particle size, temperature, surface oxidization, and surface functionalization on the phonon dynamics of silicon nanocrystals are presented. These effects are found to be greater on the transverse acoustic phonon modes than the optical phonon modes in silicon nanocrystals. In Chapter 5, the atomic structures of 3-nm spherical silicon nanocrystals were measured with elastic neutron scattering for the first time. The diffraction spectra show huge anisotropic structure variations inside the silicon nanocrystals compared to their bulk counterpart. In Chapter 6, the effect of the low-concentration dopants on the phonon dynamics of sapphire was studied using inelastic neutron scattering. This dissertation sheds light on the phonon dynamics, as well as their dependence on the intrinsic and extrinsic effects, of materials with great potential applications and will contribute to further investigations on the phonon engineering of various materials.

CONTENTS

2. Giant Low-Temperature Anharmonicity in Silicon Nanocrystals

3. Distinct Acoustic and Optical Phonon Responses to Particle Size, Oxidation, and Temperature in Silicon Nanocrystals

4. Hydrogen-Dominated Phonon Dynamics in Surface Functionalized Silicon Nanocrystals

5. Anisotropic Structure Variations in Silicon Nanocrystals

6. Trivial Modifications of Acoustic Phonon Group Velocity in Lightly Cr-doped and Lightly Ti-doped Sapphires

List of Figures

List of Tables

Chapter 1

Introduction

Atoms spontaneously vibrate in nature. The atomic vibrations are closely related to materials' physical and mechanical properties. This makes studying atomic dynamics an indispensable subject for better understanding the physical world. In analogy with the photon of the electromagnetic wave, phonon is introduced as a quantized elastic wave to mathematically describe lattice dynamics of materials. The energy of an elastic mode of angular frequency ω is

$$E = (n + \frac{1}{2})\hbar\omega \tag{1.1}$$

where n and $\hbar$ are the number of phonon modes and reduced Planck constant, respectively.[1] The term $\frac{1}{2}\hbar\omega$ is the zero point energy of the mode (Energy at 0 K). Phonon not only carries heat and dominates thermal properties such as heat capacity and thermal conductivity in many ceramic materials, but it can also interact with other quasiparticles such as electrons and magnons to influence the electromagnetic properties of materials. The study of phonon dynamics can help people obtain fundamental insights into material properties, explain material performances, and explore materials' potential for broader applications in contemporary industry.

The following sections will include a brief introduction to phonon dynamics and neutron scattering as a powerful technique used to study phonon dynamics and other physical properties of materials.

1.1 Acoustic and optical phonon modes

To better understand phonon, we consider a one-dimensional linear chain model of N atoms connected by elastic springs at separation a, as shown in Figure. 1.1.

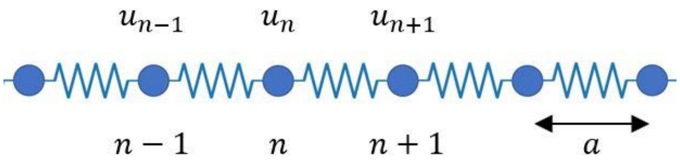

Figure 1.1 One-dimensional linear chain of atoms.

With harmonic approximation and only considering nearest neighbor interactions for brevity, the force act on the nth atom is:

$$F_n = \mathrm{C}(u_{n+1} - u_n) + \mathrm{C}(u_n - u_{n-1}) \tag{1.2}$$

where C and u are the force constant and atomic displacement from its equilibrium position, respectively. The equation of motion can be written as:

$$M\frac{\partial^2 u}{\partial t^2} = -\mathrm{C}(2u_n - u_{n+1} - u_{n-1}) \tag{1.3}$$

where M and t are atomic mass and time, respectively. Now we look for a solution of the form:

$$u(x,t) = Ae^{i(qx_n - \omega t)} \tag{1.4}$$

where x_n, q and A are the equilibrium position of the nth atom $x_n = na$, the phonon wavevector, and the amplitude, respectively. With Equation 1.3 and 1.4, we obtain phonon dispersion which describes the relations between phonon frequencies and wavevectors of this one-dimensional linear chain model:

$$\omega = 2\sqrt{\frac{C}{M}}\left|sin\frac{qa}{2}\right| \tag{1.5}$$

These phonon modes describe in phase atomic vibrations as long-wavelength acoustical vibrations and are called acoustical modes. The phonon group velocity defined by $v_g = \frac{\partial w}{\partial q}$ of the acoustic phonon branch equals the velocity of sound in the small q or the long wavelength limit.

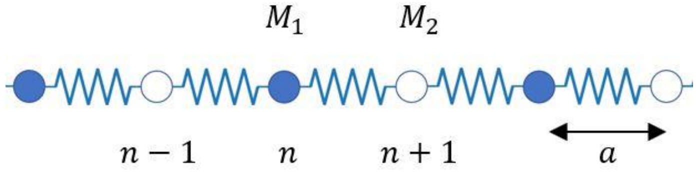

Figure 1.2 One-dimensional linear chain of two types of atoms.

We now suppose the previous model contains two types of atoms with atomic masses of M_1 and M_2 per primitive basis, as shown in Figure 1.2. With similar assumptions, we can write two equations of motion:

$$M_1 \frac{\partial^2 u_n}{\partial t^2} = -\mathrm{C}(2u_n - u_{n+1} - u_{n-1}) \tag{1.6}$$
$$M_2 \frac{\partial^2 u_{n+1}}{\partial t^2} = -\mathrm{C}(2u_{n+1} - u_{n+2} - u_n)$$

We look for solutions of the form with amplitudes A_1 and A_2:

$$u_n = A_1 e^{i(qna - \omega t)} \tag{1.7}$$
$$u_{n+1} = A_2 e^{i(q(n+1)a - \omega t)}$$

On substitution of Equation (1.7) in Equation (1.6) we have:

$$\omega^2 = C(\frac{1}{M_1} + \frac{1}{M_2}) \pm C\sqrt{(\frac{1}{M_1} + \frac{1}{M_2})^2 - \frac{4sin^2 qa}{M_1 M_2}} \tag{1.8}$$

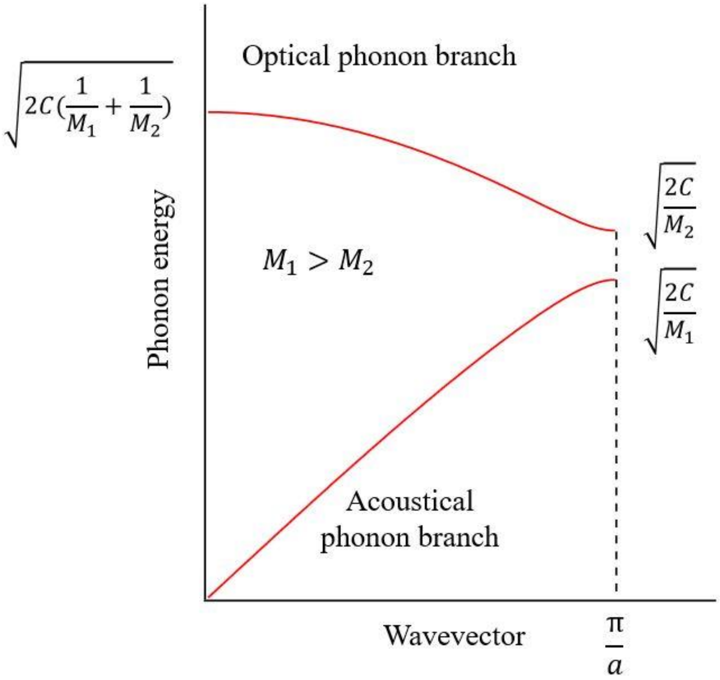

Figure 1.3 Optical and acoustical branches of the dispersion relation for a one-dimensional diatomic linear chain model.

Figure 1.3 shows such phonon dispersions in the first Brillouin zone which, in three-dimensional space, is the smallest volume entirely enclosed by planes that are the perpendicular bisectors of the reciprocal lattice vectors drawn from the origin. The lower

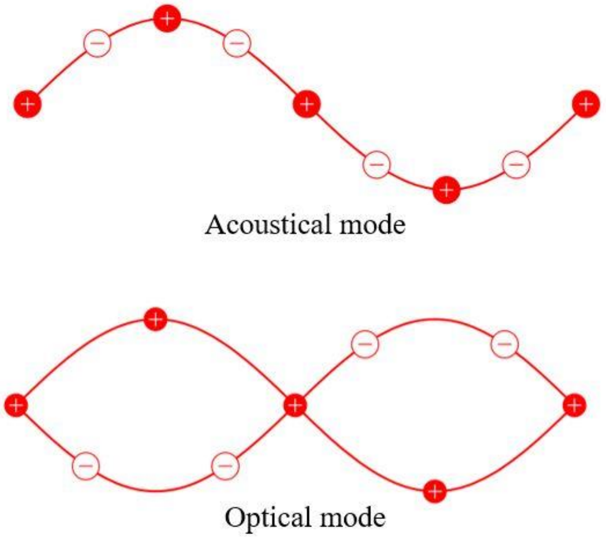

Figure 1.4 Acoustical and optical waves in a one-dimensional diatomic linear chain model.

curve is the acoustic phonon branch which describes in phase atomic vibrations. The upper curve describes movements where atoms vibrate out of phase. If the two atoms carry opposite charges, the atomic motion described by the upper curve can be excited with the electric field of a light wave, as shown in Figure 1.4. So, these phonon modes are called optical modes.

1.2 Neutron scattering fundamentals

Phonon dynamics can be measured with neutron scatterings. Because of many unique properties of neutrons, neutron scattering has become a powerful technique to study not only phonon dynamics but also atomic structures and magnetic properties of materials and has been widely applied in many areas of science. The fact that neutrons carry no charge allows them to penetrate deeply through Coulomb barriers into the target and be scattered by nuclear forces. This makes neutron scattering a better tool to study light elements compared to electron and photon scatterings which are more dependent on electromagnetic interactions.

A neutron is normally treated as a classic particle in neutron scatterings due to its relatively large mass (1.675×10^{-27} kg). The kinetic energy of thermal neutrons (5-100 meV) is of the same order as phonon energies in condensed matter so that neutron scatterings can provide accurate information on phonon dynamics in the scattering system through inelastic interactions.[2] In addition, the value of the mass of the neutron results in the de Broglie wavelength of thermal neutrons being of the order of interatomic distances in solids and liquids so that neutron scatterings are able to yield structure information of the scattering system through elastic interactions. Neutrons also carry magnetic moments.

This means that neutrons can interact with unpaired electrons in magnetic atoms and provide information on magnetic excitations and time-dependent spin correlations in the scattering system.

A typical neutron scattering experiment requires a source of neutron, interesting samples, and detectors, as schematically shown in Figure 1.5, where $\mathbf{k_i}$, $\mathbf{k_f}$, and $\mathbf{Q}$ are the wavevector of the incident neutron, the wavevector of the scattered neutron, and the change in wavevector, respectively. In the case of elastic scattering, neutrons do not exchange energy with the sample and $|\mathbf{k_i}| = |\mathbf{k_f}|$. In the case of an inelastic scattering when a neutron transfers its energy to the sample and creates a phonon, the phonon wavevector equals $\mathbf{Q}$ and the phonon energy equals to $\mathbf{E_i} - \mathbf{E_f}$, where $\mathbf{E_i}$ and $\mathbf{E_f}$ are the energy of the incident neutron and the energy of the scattered neutron, respectively. The relations between the momentum P and the energy E of the created phonon and the neutron can be summarized as:

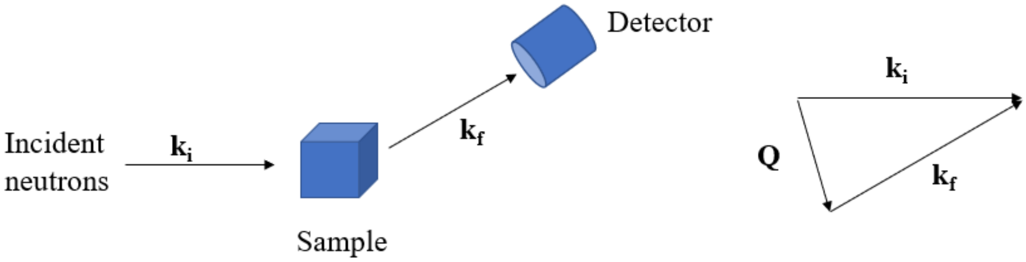

Figure 1.5 A schematic of neutron scattering principles.

$$P = -\hbar\mathbf{Q} = \hbar(\mathbf{k_i} - \mathbf{k_f}) = m_n(v_i - v_f) \tag{1.9}$$
$$E = \mathbf{E_i} - \mathbf{E_f} = \frac{\hbar^2}{2m_n}(\mathbf{k_i}^{\mathbf{2}} - \mathbf{k_f}^2)$$

where m_n, v_i, and v_f are neutron mass, the velocity of the incident neutron, and the velocity of the scattered neutron, respectively.

1.3 Reference

(1) Kittel, C. *Introduction to Solid State Physics*, 8th ed.; Wiley, 2004.

(2) Squires, G. L. *Introduction to the Theory of Thermal Neutron Scattering*; Courier Corporation, 1996.

Chapter 2

Giant Low-Temperature Anharmonicity in Silicon Nanocrystals

2.1 Abstract

The phonon density of states of silicon nanocrystals with particle size between 4 and 7.5 nm was measured by inelastic neutron scattering for the first time in the 5~600 K temperature range. The narrow particle size distributions enable the unprecedented study of size effects on phonon dynamics. Giant energy decreases and broadenings of phonon features, and the disappearance of intermediate-energy phonon modes were observed with decreasing nanocrystal size. Such particle size effects are mostly attributed to the structure variations within the nanocrystals. The phonon modes in silicon nanocrystals show temperature dependence opposite to the bulk silicon, explained by the large anharmonicity of the under-constrained near-surface phonon features. This is supported by the abnormal atomic mean-square-displacement and low energy phonon population in small silicon nanocrystals. This work provides crucial information on the phonon dynamics in spatially confined materials.

2.2 Introduction

Semiconductor nanocrystals have attracted interest because their properties are different from those of their bulk counterparts. Silicon, a semiconductor with an indirect electron band gap, is widely used in various applications, including electronics and photovoltaics, along with chemical industry and medical treatment.[1] Nanostructures are often found in silicon-based devices, such as those fabricated in the state-of-the-art 5 nm process. The increasing range of applications of nano silicon motivates the need for a better understanding of its properties. In particular, a more detailed understanding of the thermal and electronic properties of nano silicon is crucial for the continued advancement of its applications in nano electronics.

Previous studies show phonon confinement plays an important role in thermal transport in spatially confined silicon structures. Studies of silicon nanowires have shown a decreased thermal conductivity with smaller sample diameters attributed to the phonon confinement.[2] Alvarez's study on porous silicon claimed the thermal conductivity is lower for higher porosity and smaller pore radius as a consequence of phonon ballistic effects.[3] Chávez-Ángel reported the reduction of the thermal conductivity in ultra-thin suspended silicon membranes, using the Fuchs-Sondheimer model of phonon boundary scattering at the surfaces to explain the effects.[4] The phonons are also sensitive to local strain, as observed by Li in the change of the thermal conductivity of the silicon nanowires and thin films[5].

Phonons can play important roles in the electronic and optical properties of spatially confined silicon systems. Silicon has an indirect band gap, and it is believed that electron-phonon coupling is necessary for the photon absorption and emission processes. This has been illustrated by the observation of photoluminescence of red light from porous silicon.[6,7] Photoluminescence was also observed from silicon nanocrystals and other quantum dots. For example, emission through the full visible spectrum was observed under UV excitation[8] out of silicon nanocrystals synthesized by a nonthermal plasma reaction scheme.[9] Additionally, it was reported that the hot (phonon-free) photoluminescence has the opposite size dependency from the phonon-mediated counterpart.[10] While quantum confinement in silicon nanocrystals has been extensively studied, the role of phonon confinement is less clear.[11–15] Understanding phonon dynamics in silicon nanocrystals is crucial for understanding their optoelectronic properties and for applications such as photovoltaics and light-emitting devices. However, prior experimental measurements are mostly based on optical spectroscopy,[15–18] which only has access to the Raman active phonon modes at the center of the Brillouin zone.

In this chapter, inelastic neutron scattering (INS) experiments were performed on silicon nanocrystals from 4 to 7.4 nm in diameter and polycrystalline bulk silicon. Due to the nature of random orientations in nanocrystal samples, only the phonon density of states (DOS) were measured instead of phonon dispersion curves. Molecular dynamics (MD) simulation is used to interpret the experimental results. This work presents new insights into the size and temperature dependence of the phonon dynamics through the whole

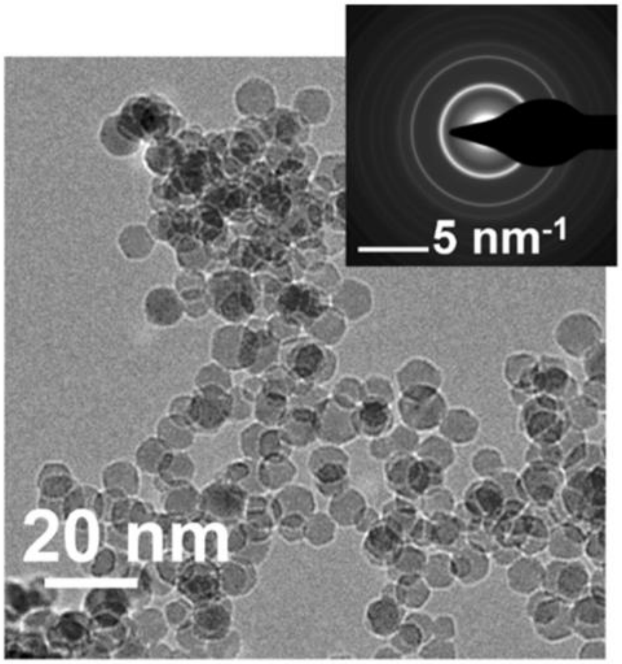

Figure 2.1 Silicon nanocrystals under TEM.

Brillouin zone in silicon nanocrystals, and it will provide valuable information on the phonon dynamics in confined systems.

2.3 Materials and methods

The silicon nanocrystals were synthesized by a non-thermal plasma process.[19,20] The reactor consisted of a quartz tube, through which a mixture of argon, silane, and hydrogen gas flowed and was evacuated by a roughing pump. The plasma discharge was sustained by biasing a copper electrode surrounding the quartz tube with a 13.56 MHz RF power supply. Downstream of the reactor chamber, the silicon nanocrystals were collected on a stainless-steel mesh. The size of silicon nanocrystals was controlled by adjusting the reactor pressure and precursor flow rates. A representative transmission electron microscopy (TEM) image of the silicon nanocrystals is shown in Figure 2.1 The selected area electron diffraction inset shows diffraction rings confirming that the particles are crystalline silicon. Particle size distributions were measured from TEM images and fit to Gaussian profiles, shown in Figure 2.2. As the average particle size increases, the distribution broadens moderately.

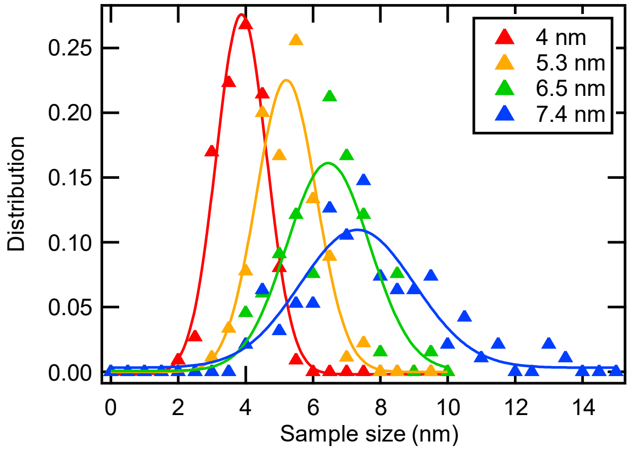

Figure 2.2 Nanocrystal size distribution. The lines are Gaussian fittings.

INS measurements were performed on the Wide Angular-Range Chopper Spectrometer (ARCS), a direct geometry chopper neutron spectrometer, and the Vibrational Spectrometer (VISION), an indirect geometry chopper neutron spectrometer, both of which are at Oak Ridge National Laboratory. All the samples were loaded and carefully sealed in a 3/8-inch diameter aluminum can under a helium atmosphere in order to avoid oxidation. ARCS has an energy resolution of 4% or better of the neutron incident energy (E_i).[21] Neutron beams with E_i of 30, 90, and 150 meV were chosen to optimize the energy resolution and range, as shown in Figure 2.3.

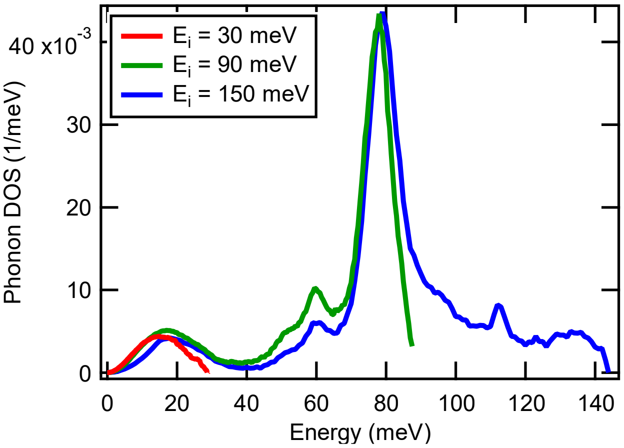

Figure 2.3 Phonon DOS of 4 nm silicon nanocrystals at 300 K measured at ARCS by neutrons with E_i of 30, 90, and 150 meV.

Silicon nanocrystals with diameters of 4, 6.5, and 7.4 nm, and bulk silicon were measured at ARCS at 5, 150, 300, 450, and 600 K, while the 5.3 nm sample was measured at 5 and 300 K. VISION has an energy resolution less than 1.5% of the energy transfer.[22] The phonon spectra of 4 and 7.4 nm silicon nanocrystals as well as bulk silicon were also collected at VISION at 5, 150, and 300 K.

2.4 Data processing

Mantid software[23] was used for data processing. The event mode data of ARCS measurement contains information about the detector number and the time-of-arrival of each scattered neutron. The momentum (q) and energy (E) transfer of each neutron was calculated from its time-of-flight and scattering geometry, with the knowledge of the distance between detectors and the sample to generate the scattering intensity S(q, E). Backgrounds from an empty can were subtracted from the signal. The phonon spectra were analyzed within the incoherent approximation, which has been shown to work reliably.[24–26] Elastic intensities were removed below 6, 7, and 10 meV for E_i = 30, 90, and 150 meV respectively. The low energy parts of the phonon DOSs of the silicon nanocrystals were extrapolated by power functions, while the low energy part of the phonon DOS of bulk silicon was extrapolated by the Debye model, as described in the Discussion Section. The energy bin sizes were set at 0.25, 0.5, and 1 meV for E_i = 30, 90, and 150 meV respectively. Due to the small effective sample thickness, no multiple scattering correction was necessary. Multi-phonon scattering correction was performed by an iterative method considering the S(q, E) and the multi-phonon expansion.[24] The phonon spectra were also corrected for the thermal occupation. The event mode data of VISION was used to calculate the energy transfer of each neutron to produce vibrational spectra. The background from empty cans was subtracted after accounting for the shielding effects. Elastic intensities were removed below 5 meV. The thermal occupation correction was performed on these phonon spectra. It should be noted that the phonon spectra from VISION, an indirect geometry spectrometer, are different from phonon DOS because the measurement covers a specific part of the reciprocal space. The inverted geometry arrangement of VISION granted it with improved signal-to-noise ratio, good resolution and high counting rates. On the other hand, the limited q range of VISION compared with that of ARCS makes it incapable of depicting the phonon DOS. No multiphonon scattering correction was applied on the VISION data.

The strong peak near 75 meV in Figure 2.3 is from the hydrogen phonon modes related to the surface hydrogen terminations.[27,28] The hydrogen atomic concentrations in our samples were estimated to be less than 2% using Equation (2.1),

$$\frac{C_H}{C_{Si}} = \frac{\sigma_{Si} A_H \sqrt{M_H}}{\sigma_H A_{Si} \sqrt{M_{Si}}} \tag{2.1}$$

where C, σ, A, and M are the atomic concentrations, neutron scattering cross-sections, areas in neutron-weighted phonon DOS and atomic mass of hydrogen and silicon respectively. The areas of the Gaussian fittings to the hydrogen phonon features near 75 meV (E_i = 90 meV) were considered as the hydrogen-only mode (longitudinal and shear horizontal wagging modes), while the residual areas were considered as the silicon modes. The number of free surface bonds was estimated by constructing spherical clusters and subtracting the number of formed Si-Si bonds from the number of the bonds that could possibly form in a bulk structure with the same number of atoms. For example, this estimation shows there are 314 free bonds on the surface of a spherical 4 nm silicon nanocrystal. The hydrogen atomic concentration in the 4 nm sample was estimated to have a value of 0.8%, which corresponds to a 5% surface occupation if all hydrogen atoms were on the nanocrystal surface. These values are underestimated because the Si-H stretching vibration mode (near 260 meV) was not taken into consideration, however, considering the small values from the estimations, the hydrogen concentrations are believed to be small. Even though only a small amount of hydrogen exists at the surface of the silicon nanocrystals, the neutron scattering signal of the mode is strong because hydrogen has a neutron scattering cross section 37.8 times greater than that of silicon and lighter atomic mass. To obtain the silicon-only phonon DOS, these hydrogen phonon features were subtracted after fitting them with Gaussian functions. The phonon feature near 110 meV was believed to be the signal of surface oxygen whose atomic concentrations were estimated to be less than 2% using the same method.

2.5 Calculation

The phonon DOS was calculated by MD simulation using the LAMMPS package.[29–33] The position and velocity of each atom at each time step were obtained by solving the equations of motion with the Tersoff potential for silicon.[34] Then the calculated trajectories were used to construct the phonon dynamical matrix, making use of fluctuation-dissipation theory taking the form of Equation (2.2) – (2.4), before computing the phonon DOS by evaluating the eigenvalues. In the set of equations below, $\mathbf{D}$, $\mathbf{\Phi}$, $\mathbf{G}$, $\mathbf{R}$, and m are the element in the dynamical matrix, second order force constant, the lattice Green's function coefficient, the actual position of the atom under the influence of a vibration, and the atomic mass respectively, where k denotes the basis atom in each unit cell, α and β enumerate all x, y, and z coordinates

$$\mathbf{D}_{k\alpha,k'\beta}(\mathbf{q}) = (\mathrm{m}_k \mathrm{m}_{k'})^{-\frac{1}{2}} \mathbf{\Phi}_{k\alpha,k'\beta}(\mathbf{q}) \tag{2.2}$$

$$\mathbf{\Phi}_{k\alpha,k'\beta}(\mathbf{q}) = k_B T \mathbf{G}^{-1}_{k\alpha,k'\beta}(\mathbf{q}) \tag{2.3}$$

$$\mathbf{G}_{k\alpha,k'\beta}(\mathbf{q}) = \langle \mathbf{R}_{k\alpha}(\mathbf{q}) \bullet \mathbf{R}^{*}_{k'\beta}(\mathbf{q}) \rangle - \langle \mathbf{R} \rangle_{k\alpha}(\mathbf{q}) \bullet \langle \mathbf{R} \rangle^{*}_{k'\beta}(\mathbf{q}) \tag{2.4}$$

Calculations were performed on a 4 × 4 × 4 silicon supercell with 512 atoms for bulk material and a 4 nm spherical silicon cluster with 1707 silicon atoms. The initial silicon structures used in the simulation had the space group of Fd-3m. The 4 nm spherical silicon cluster was set at the center of a box with a 20 nm edge length and periodic boundary conditions. The cutoff distance of force potential was set to 0.05 nm. Both simulations were performed under isothermal and isobaric conditions at 300 K and 0 bar. For MD simulation, the temperature damping parameter and the pressure damping parameter were 1 ps and the time step was 2 fs. Equilibrium was considered to be achieved when the calculated phonon DOS converged, which takes roughly tens of nanoseconds. The phonon DOS of the spherical silicon cluster was calculated at the Brillouin zone center while a 20 × 20 × 20 Monkhorst-Pack mesh was used for the silicon supercell.

2.6 Result and discussion

Two main phonon features were observed in the DOS of the silicon nanocrystals, as shown in Figure 2.4 (a) and (b). For simplicity, the features from 0 to 30 meV are referred to as the low energy phonon features (LEPF), and the features from 45 to 73 meV are referred to as the high energy phonon features (HEPF). The LEPF and the HEPF correspond to the transverse acoustic (TA) and the optical modes respectively, in bulk silicon based on the previous calculations.[35–37] The centers and the full widths at half maximum (FWHM) of the LEPF and the HEPF were calculated by the first and the second moments (Gaussian model) from the phonon DOS obtained from the ARCS measurement. The VISION phonon spectra were plotted using the data collected by the high-angle detectors which provide stronger phonon signals at larger Q. The spectra from VISION were rebinned to the energy steps similar to the instrument resolutions to reduce statistical noise. As shown in Figure 2.4 and Figure 2.5, ARCS and VISION results agree well considering the significant difference in the coverage of reciprocal space.

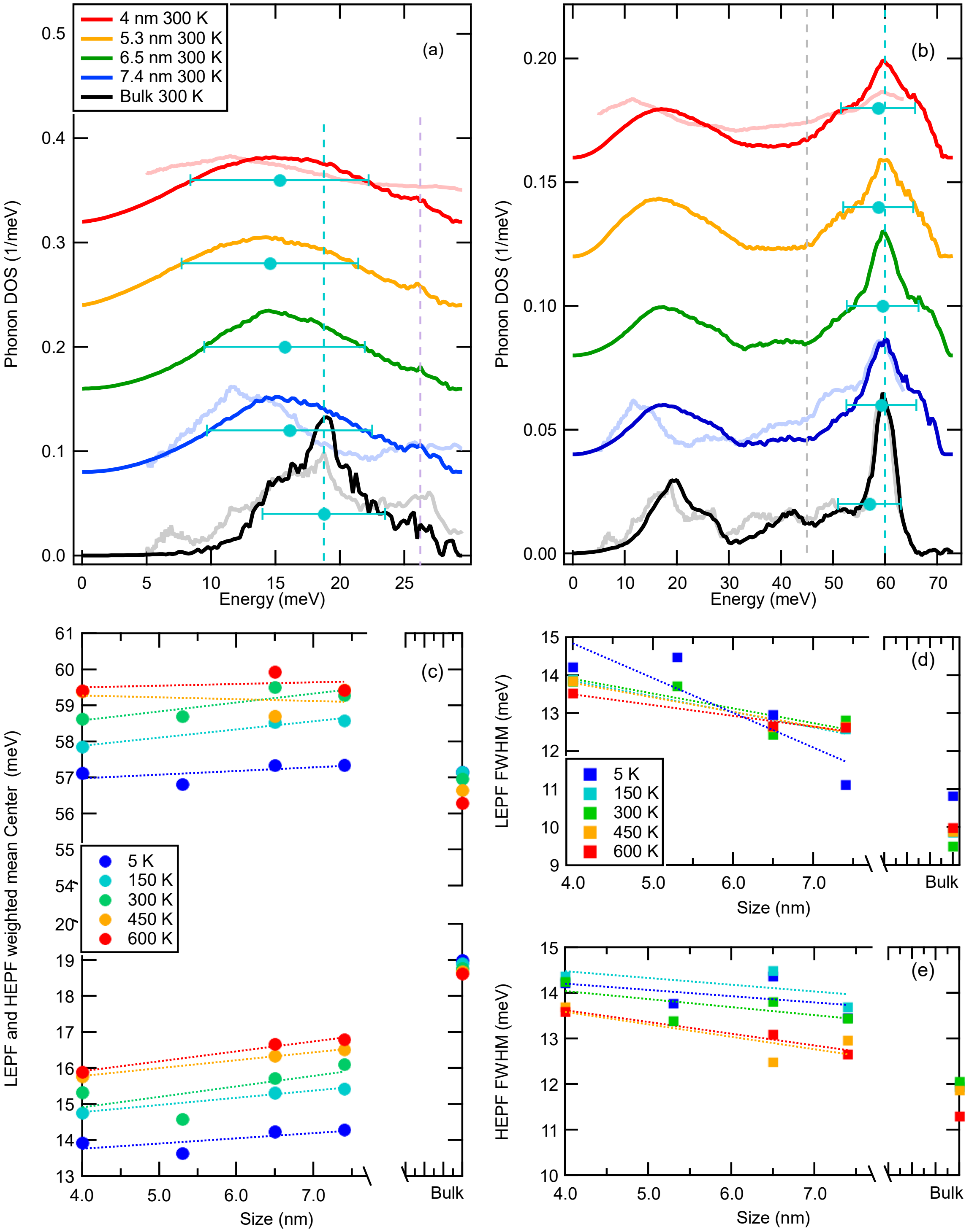
(a)
4 nm 300 K
5.3 nm 300 K
6.5 nm 300 K
7.4 nm 300 K
Bulk 300 K
Phonon DOS (1/meV)
Energy (meV)
0.0
0.1
0.2
0.3
0.4
0.5
0
5
10
15
20
25
(b)
0.00
0.05
0.10
0.15
0.20
0
10
20
30
40
50
60
70
(c)
LEPF and HEPF weighted mean Center (meV)
5 K
150 K
300 K
450 K
600 K
61
60
59
58
57
56
55
54
20
19
18
17
16
15
14
13
4.0
5.0
6.0
7.0
Bulk
Size (nm)
(d)
LEPF FWHM (meV)
15
14
13
12
11
10
9
(e)
HEPF FWHM (meV)
10
11
12
13
14
15

Figure 2.4 A reduction in nanocrystal size reduced the phonon energies and broadens the phonon features. (a) (b) Phonon DOSs/spectra measured at 300 K with E_i = 30 and 90 meV by ARCS (darker lines), and VISION (lighter lines). (c) The center energies of the LEPF (lower part) and the HEPF (upper part) in the samples with different sizes. (d) The FWHM of the LEPF and (e) the HEPF in the samples with different sizes. The dots with error bar in (a) (b) show the calculated center energies and the FWHM of the corresponding phonon features. The dash lines in (a) (b), and (c)-(e) are guides to the eye and linear fittings respectively.

Size effects on phonons are shown in Figure 2.4. As nanocrystal size decreases, the LEPF experience significant energy decreases. As an example, the 4 nm sample shows the energy of the LEPF is 18% smaller than that of the bulk sample at 300 K. On the other hand, the HEPF in the nanocrystals do not show strong size dependence. Both features significantly broaden as nanocrystal size decreases. Additionally, the intermediate phonon feature near 41 meV, which is related to the top of the longitudinal acoustic (LA) phonon branch in bulk silicon, becomes weaker with the decrease in particle size. Temperature effects on the phonons are shown in Figure 2.4. The 13% energy increase of the LEPF with increasing temperature from 5 to 600 K was observed in 4 nm silicon nanocrystals. This is dramatically different from bulk silicon, in which the energies of both the LEPF and the HEPF features slightly decrease with the increase in temperature. The widths of both features do not vary much with temperature. Overall, particle size and temperature have much stronger effects on the LEPF than the HEPF.

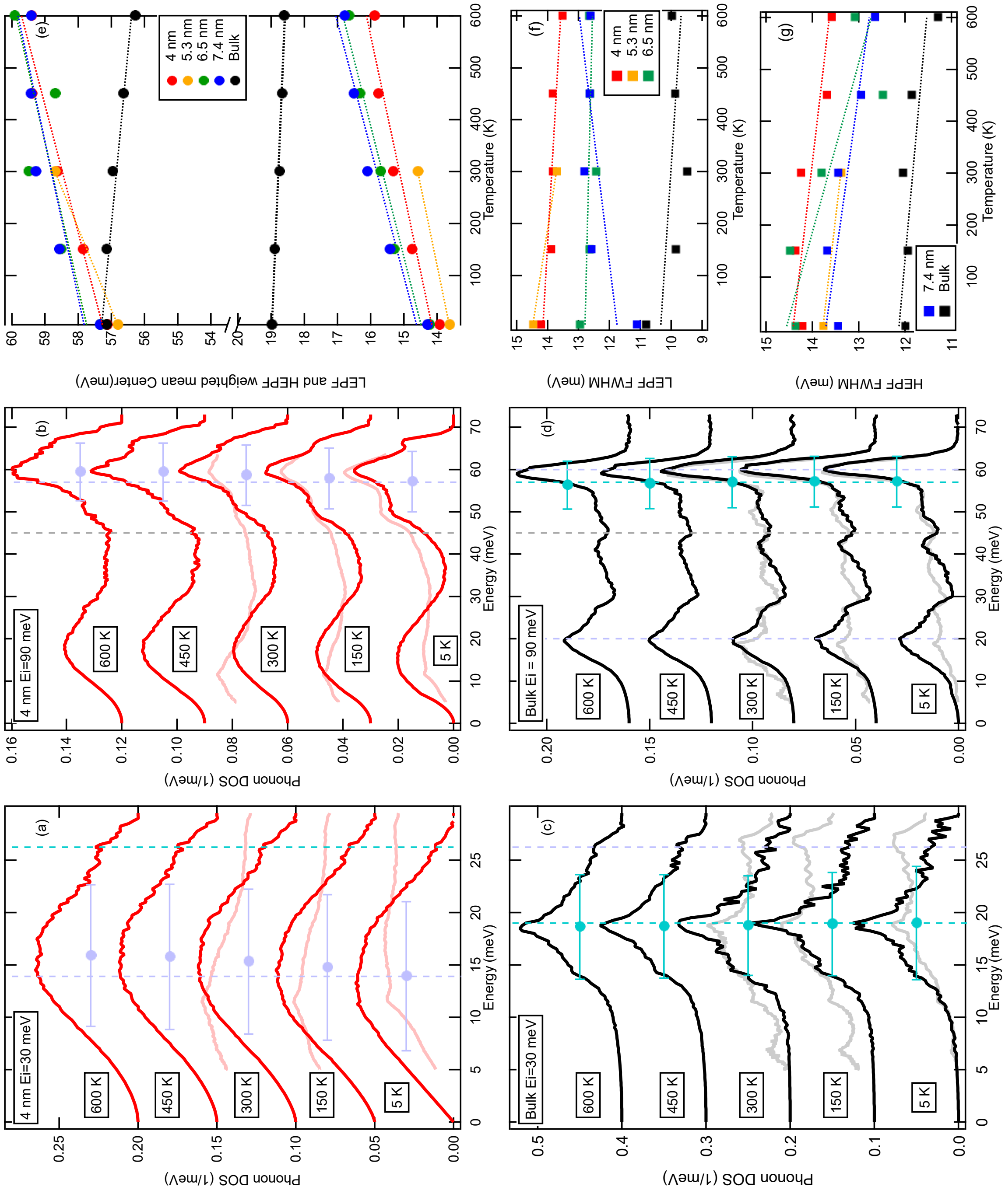
(a)
4 nm Ei=30 meV
600 K
450 K
300 K
150 K
5 K
Phonon DOS (1/meV)
Energy (meV)
(b)
4 nm Ei=90 meV
(c)
Bulk Ei=30 meV
(d)
Bulk Ei = 90 meV
(e)
4 nm
5.3 nm
6.5 nm
7.4 nm
Bulk
LEPF and HEPF weighted mean Center(meV)
Temperature (K)
(f)
LEPF FWHM (meV)
(g)
HEPF FWHM (meV)

Figure 2.5 An elevation of temperature decreases the phonon energies and narrows the phonon features in bulk silicon while it increases the phonon energies in silicon nanocrystals. (a) (b) Phonon DOSs of 4 nm silicon nanocrystals measured with E_i = 30 and 90 meV by ARCS (darker lines), and VISION (lighter lines). (c) (d) Phonon DOSs of bulk silicon measured with E_i = 30 and 90 meV by ARCS (darker lines), and VISION (lighter lines). (e) The center energies of the LEPF (lower part) and the HEPF (upper part) in the samples at different temperatures. (f) The FWHM of the LEPF and (g) the HEPF in the samples at different temperatures. The dots with error bar in (a)-(d) show the calculated center energies and the FWHM of the corresponding phonon features. The dash lines in (a)-(d), and (e)-(g) are guides to the eye and linear fittings respectively.

2.6.1 Comparison between ARCS measurement and MD simulation

The comparisons between the phonon DOSs of 4 nm silicon nanocrystals and bulk silicon obtained from ARCS measurement and MD simulation are shown in Figure 2.6. The discrepancy between the widths of the LEPF for 4 nm silicon nanocrystals is expected because the sample has a finite size distribution which further broadens the phonon DOSs. The energy difference in the bulk silicon comes from the empirical nature of the potentials.[37]

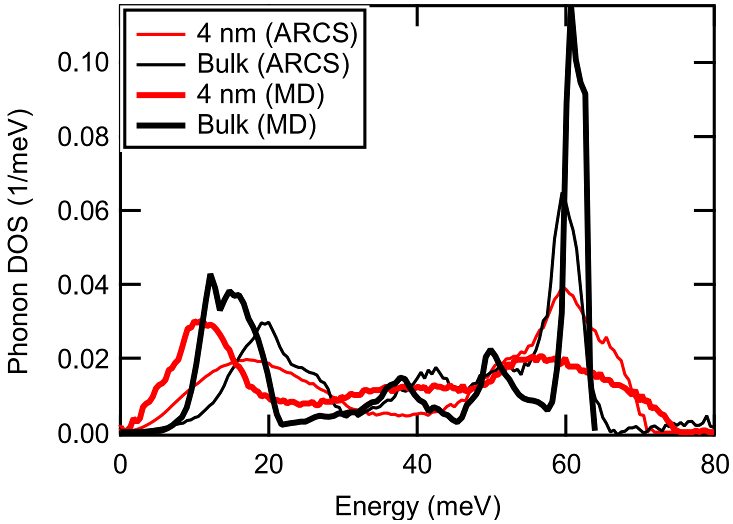

Figure 2.6 The comparisons between the phonon DOSs obtained from ARCS measurements and MD simulations at 300 K.

2.6.2 Size-induced phonon energy shift

According to MD simulation, the size-induced phonon behavior originates from the structure variations within silicon nanocrystals. This is illustrated by plotting the distribution of average Si-Si bond length along the radius of 4 nm silicon nanocrystals (red dots) and the relaxed average bulk bond length (blue dash line) at 300 K, as shown in Figure 2.7.

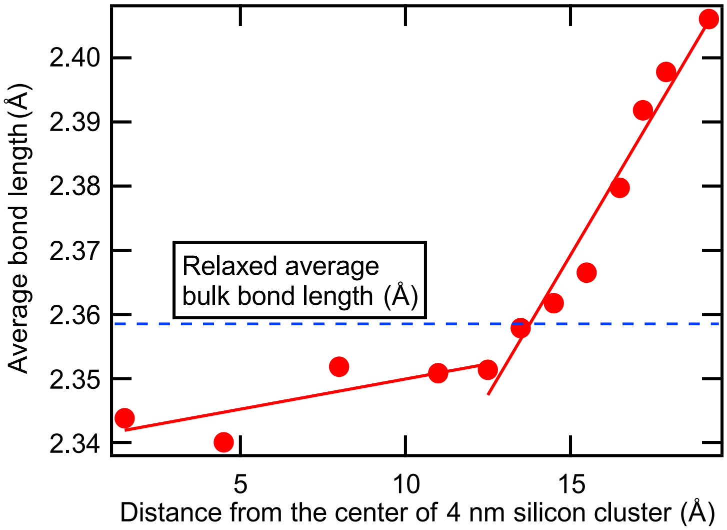

Figure 2.7 Si-Si bond length distribution along the radius in 4 nm silicon nanocrystals from MD simulation shows longer bonds near the surface. The solid lines are linear fittings (1.5~12.5 Å and 12.5~19.2 Å). The dash line is the relaxed average bond length in silicon supercell.

The Si-Si bond length was calculated as the distance between two adjacent silicon atoms within the range between 0 and 3 Å, knowing the Si-Si bond length in bulk silicon is close to 2.35 Å. The average bond lengths of the near-surface atoms are found to be larger than the relaxed bulk silicon, while the inner core atoms are packed tighter than the bulk silicon. For 4 nm silicon nanocrystals, the shell is defined as the region of radius from 16 to 20 Å, where the average bond distance experiences a rapid increase, and the core is defined as the region of radius from 0 to 8 Å where the average bond length is roughly independent of the location.

The longer bond length in the shell region potentially induces a capillary pressure on the core region of the silicon nanocrystals.[38] The magnitude of the capillary pressure was estimated by applying:

$$P = B\frac{\Delta V}{V} \tag{2.5}$$

where B, ΔV, and V are bulk modulus, the change of volume due to the change of the average Si-Si bond length along the radius of nanocrystals, and the volume calculated from the relaxed Si-Si bond length in bulk silicon respectively. Assuming a value of bulk modulus at 50 GPa for 4 nm silicon nanocrystals (the bulk modulus of bulk silicon is roughly 100 GPa), the capillary pressure on the core region due to volume change can reach 2~3 GPa. This capillary pressure likely induces the Si-Si bond length distribution. The core atoms are considered to have higher coordination numbers than shell atoms because they are more closely packed. A previous simulation also states the core atoms have higher coordination numbers, however, with larger bond lengths.[39] Our calculation suggests otherwise.

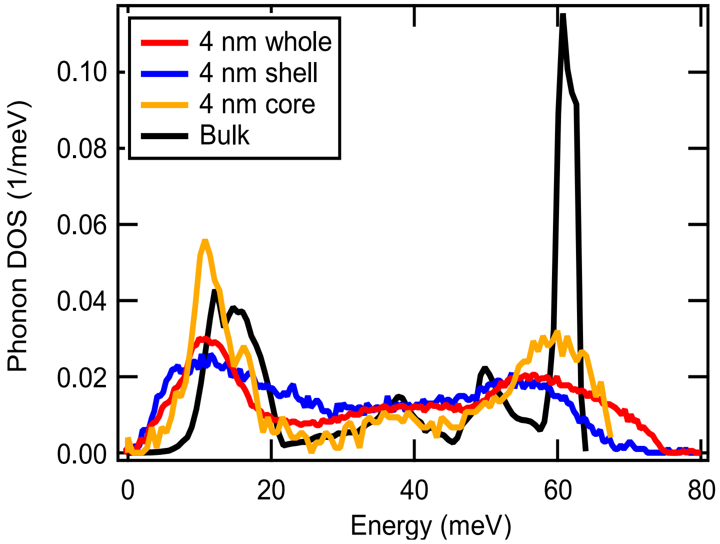

Figure 2.8 Partial phonon DOSs of different spatial regions calculated by MD simulation. The phonon DOS of the shell in 4 nm silicon nanocrystals deviates from that of the bulk the most.

The particle size-induced energy shifting of the LEPF is mainly attributed to the shell phonon modes in the silicon nanocrystals. Partial phonon DOS was calculated for the core and shell region, shown in Figure 2.8. The shell region shows a softer LEPF than that of the bulk silicon, while the core region behaves more like bulk silicon. Although MD simulation only qualitatively reproduces the phonon DOS, as shown in Figure 2.6, it is still a valuable tool to interpret the nanocrystal results. The result is consistent with previous work based on a different interatomic potential.[40] Considering the large volume of the shell region, the softening of the LEPF in silicon nanocrystals can be mostly attributed to shell phonon modes. Compared with bulk silicon, the nanocrystals have a larger fraction of atoms located at or near the surfaces with distortion of the local structure.

In addition to the near-surface shell modes, surface waves may also contribute to the softening of the LEPF in silicon nanocrystals, but the effect is expected to be small. Rayleigh waves, typical surface phonons, have lower frequencies than typical acoustic phonons based on theoretical calculations and Helium scattering measurements.[27,41] Even though silicon nanocrystals have a large surface area to volume ratio, the number of the surface phonon modes is still small and only accounts for an insignificant portion of the overall phonon population.

The energy of the HEPF in silicon nanocrystals appears unchanged with particle size, although their spectra were significantly different from those in bulk silicon. For example, the phonon mode at 60 meV has energy shifts less than 0.5 meV for all the samples, as shown in Figure 2.4. This is different from but not conflicting with the previous Raman work, where the red shift of optical phonon was observed as particle size decreases.[15] Raman spectroscopy only has access to the Raman active modes at the Brillouin zone center. On the other hand, INS measures the overall phonon DOS integrated over the entire Brillouin zone.

2.6.3 Size-induced phonon broadening

The broadening of the HEPF in smaller silicon nanocrystals might have several origins but is considered to be mainly from the wide Si-Si bond length distribution in silicon nanocrystals. The increasing average Si-Si bond length from the center to the surface results in changes in optical phonon energy. It is estimated that the broadening is consistent with the reported Grüneisen parameters in bulk silicon using:

$$\Delta E_i = -\gamma_i \frac{\Delta V}{V} E_i \tag{2.6}$$

where ΔE_i, γ_i, ΔV, V, and E_i are the energy shift of the ith phonon mode, the mode-Grüneisen parameter, the change of volume, the volume calculated with bulk value, and phonon energy respectively. The estimated phonon broadening of the HEPF from the change of the average bond length in 4 nm silicon nanocrystals has a value close to half of its calculated FWHM, using 1.2 as the mode-Grüneisen parameter as reported in previous work.[42] The breaking of structural symmetry near the surface might result in further broadening of the HEPF. This can also be used to explain the similar broadening of the LEPF.[37]

The contributions to the broadening of phonon features from other origins are small, for example, the broadening attribute to the reduced phonon lifetime in nanocrystals corresponding to the boundary scattering was estimated to be small using the following method. The phonon linewidth can be calculated by:

$$\Delta E_w = \frac{h}{2\pi\tau} \tag{2.7}$$

where h is Planck's constant, τ is the phonon lifetime which can be estimated by $\tau = \frac{\lambda}{v}$, where λ and v are the phonon mean-free-path and phonon group velocity.[43,44] The phonon group velocity was approximated to be 65% of that in bulk silicon, as previous work shows the Young's modulus of 5 nm silicon nanowires equals roughly 40% of that of bulk silicon, and Young's modulus is propositional to the square of the speed of sound.[45] If the nanocrystal diameter was used as the upper limit of phonon mean-free-path, for 4 nm silicon nanocrystals, this broadening was estimated to be about 0.7 meV. This is much smaller than the broadening observed in INS, where the LEPF in 4 nm silicon nanocrystals is about 1.5 times wider than that of bulk silicon. As a result, boundary scattering is unlikely the primary origin of the broadening of the LEPF in silicon nanocrystals with a particle diameter of 4 nm or larger. Similarly, the LEPF broadening induced by the nanocrystal size distribution is estimated to be less than 10% for 4 nm silicon nanocrystals, using the particle size distribution (Figure 2.2) and the size dependence of the LEPF (Figure 2.4(c)). In addition, structural defects can affect the phonon dynamics in silicon nanocrystals, for example by phonon trapping.[46] Additionally, the surface roughness can enhance the phonon scattering.[47] Due to the large surface area to volume ratios in nanocrystals, this might introduce an extra reduction in phonon lifetime and broadening of phonon linewidth. The strain gradient across the nanocrystals, shown by the different bond lengths, can also scatter phonons and reduce their lifetime. Overall, these effects are expected to be small.

The anomalous size dependence of the phonon feature near 41 meV (Figure 2.4(b)) is very interesting and observed in both the INS result and the MD simulation (Figure 2.6). According to the bulk phonon dispersion relation, the feature is related to the dip of LA phonons near the zone boundary.[35–37] The disappearing of this phonon feature in smaller silicon nanocrystals might have two explanations related to the loss of long-range translational symmetry in silicon nanocrystals. Firstly, the smaller particle size could have a confinement effect that pushes acoustic and optical phonon apart, reducing the population of intermediate phonons. It is also possible that this phonon feature is dramatically broadened by the Si-Si bond length distribution and phonon anharmonicity.

2.6.4 Phonon anharmonicity in small silicon nanocrystals

An enormous phonon anharmonicity was shown by the abnormal temperature dependence of the mean-square-displacements (MSD) in the small silicon nanocrystals. The MSD, $\langle u^2 \rangle$, was calculated from the phonon DOS with:

$$\langle u^2 \rangle = \frac{3\hbar^2}{2M} \int_0^{E_m} \frac{1}{E} coth\left(\frac{1}{2} E\beta\right) D(E) dE \qquad (2.8)$$

where $\hbar$ is reduced Planck's constant, E_m is the maximum phonon energy of silicon modes, and $\beta = \frac{1}{k_B T}$ (k_B is Boltzmann constant). The calculation was performed assuming that the DOS below 73 meV was dominated by silicon modes after the subtraction of the hydrogen peak. As shown in Figure 2.9, all the MSD increase linearly with temperature, except for that of 4 nm silicon nanocrystals, which was fitted by a power function with the exponential term of 0.7. As the linear relation between MSD and temperature is expected

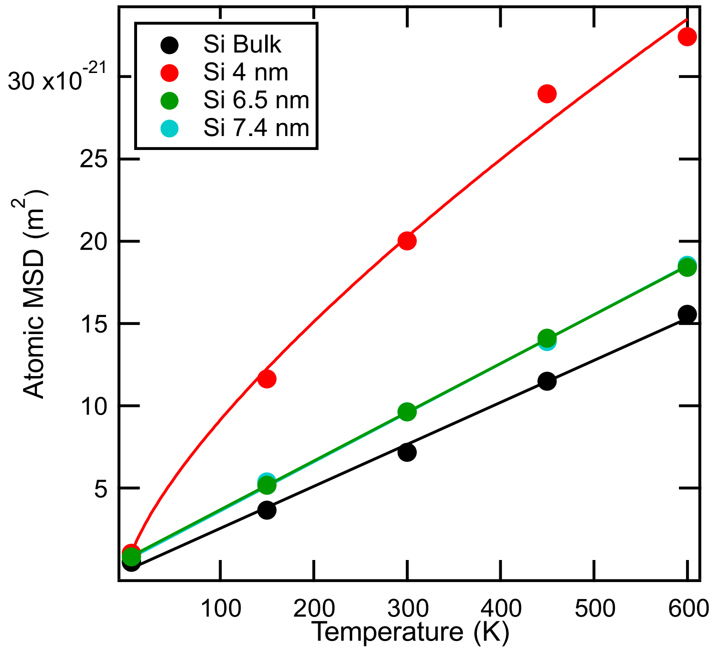

Figure 2.9 The atomic MSDs as a function of temperature calculated form phonon DOSs show the anomalous behaviors in 4 nm silicon nanocrystals. The red line is power fitting, while the other lines are linear fittings.

for harmonic oscillators, anharmonic phonons likely induce the anomalous behaviors in 4 nm silicon nanocrystals. Additionally, at temperatures above 50 K, the silicon atoms in smaller nanocrystals have MSDs about 3 times larger than the bulk value. This suggests that the atoms in smaller nanocrystals are much less confined, which is consistent with the softening of the LEPF in silicon nanocrystals.

The temperature dependence of phonon dynamics in silicon nanocrystals is radically different from that found in bulk silicon. The softening of phonon modes in bulk silicon is consistent with previous measurement[37] and the expected quasi-harmonic behavior as a result of the thermal expansion. On the other hand, the LEPF become stiffer in silicon nanocrystals at elevated temperature, as shown in Figure 2.5(e). The temperature dependence is especially large for acoustic phonons and less so for optical ones, however, the spectra weight redistributes universally, which in consistent with the phonon behaviors observed by Chetan Dhital, et.al.[48] Pronounced redistributions of the spectra weight near 50 and 66 meV are shown in Figure 2.5 (b). At higher temperatures, the phonons in silicon nanocrystals behave more and more like those in bulk silicon. This is expected because the thermal vibration may allow better relaxation of the strain of the near-surface atoms, making them more bulk-like and less anharmonic. There is also a possibility that silicon nanocrystals experience negative thermal expansion (NTE) at a wider temperature range than bulk silicon,[49–55] similar to the case of Au nanocrystals.[56] Pair distribution functions from further neutron diffraction experiments could help validate this hypothesis, for example, the Powder Diffractometer (POWGEN) at Oak Ridge National Laboratory is capable to detect small variances in d-spacings with resolution in a range of 0.0008 < Dd/d < 0.025. In order to control the particle size distribution, the diffraction measurement will be performed on the 3 nm silicon nanocrystals which will be synthesized for later experiments. The calculated widths of the LEPF don't have clear temperature dependence, as shown in Figure 2.5 (f). On the other hand, the HEPF slightly narrows at the elevated temperature, although the contribution from phonon features near 50 meV is hard to separate, as shown in Figure 2.5 (g).

The energy increase of acoustic phonons in silicon nanocrystals suggests that the group velocity of the low-energy acoustic phonon branches increases with increasing temperature. The results for the 4 nm sample are shown in Figure 2.10:

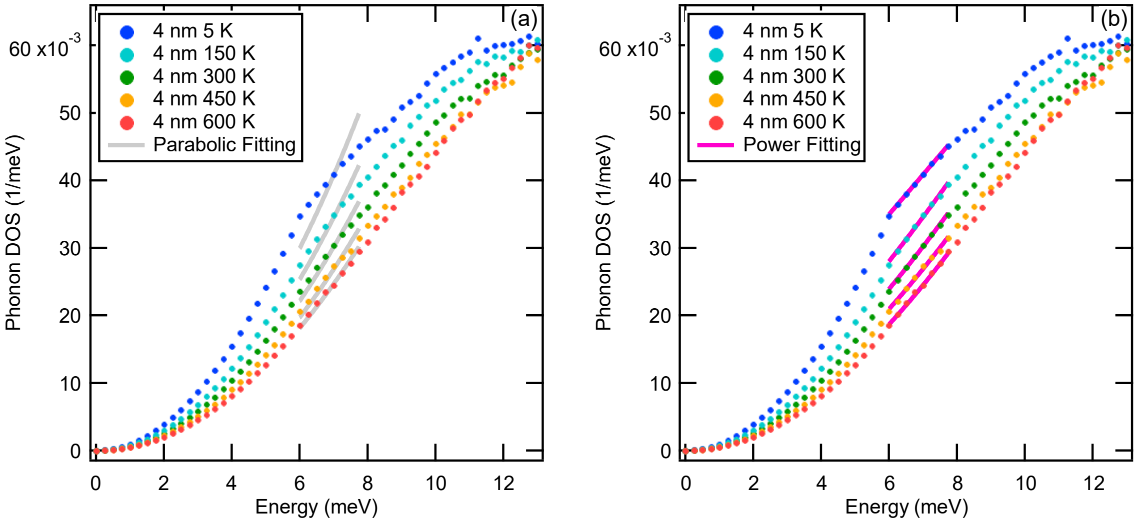

Figure 2.10 (a) Phonon DOSs of 4nm silicon nanocrystals fitted with (a) the Debye model, and (b) power functions which were used to extrapolate the low energy part of the phonon DOS (below 6 meV) of silicon nanocrystals.

where the fitting was applied on the data points between 6 and 7.75 meV. The energy range was carefully chosen to avoid the intensity tail from elastic scattering while the acoustic phonon dispersion remains mostly linear. This is in support of the likely NTE of silicon nanocrystals between 5 to 600K. Furthermore, for the 4 nm sample, only the DOS at 600 K fits well with the Debye model, which assumes linear acoustic phonon dispersion at low energies. In the Debye model, the phonon DOS may be written as:

$$D(E) = \frac{3E^2}{2v^3\pi^2} \tag{2.9}$$

where E and v are phonon energy and phonon group velocity, respectively. At lower temperatures, the fittings worsen significantly, and the phonon DOS becomes subquadratic, suggesting nonlinear dispersion relations near the zone center, as shown in Figure. 9(a). The power fittings ($D(E) = AE^B$) were adopted instead of parabolic fittings on the phonon DOS from 6 to 7.75 meV, as shown in Figure 2.10(b) for silicon nanocrystals in a temperature range of 5~600 K. The energy range used in fittings is compromised in order to avoid the signals introduced by the tails of elastic peaks. Although the elastic signal does not show glaring effect on the phonon DOS for most of the cases, it affects the phonon DOS of bulk silicon at 5 and 150 K up to 5.5 meV in terms of energy. The power fittings along with the exponential terms, *C*, of the corresponding dispersion relations near the zone center are listed in Table 2.1, which are also schematically shown in Figure 2.11. The acoustic phonon dispersion near Γ point is estimated to have an exponent ranging from 1.5 (at 5 K) to 1.09 (600 K), whereas the value is unity in the Debye model.

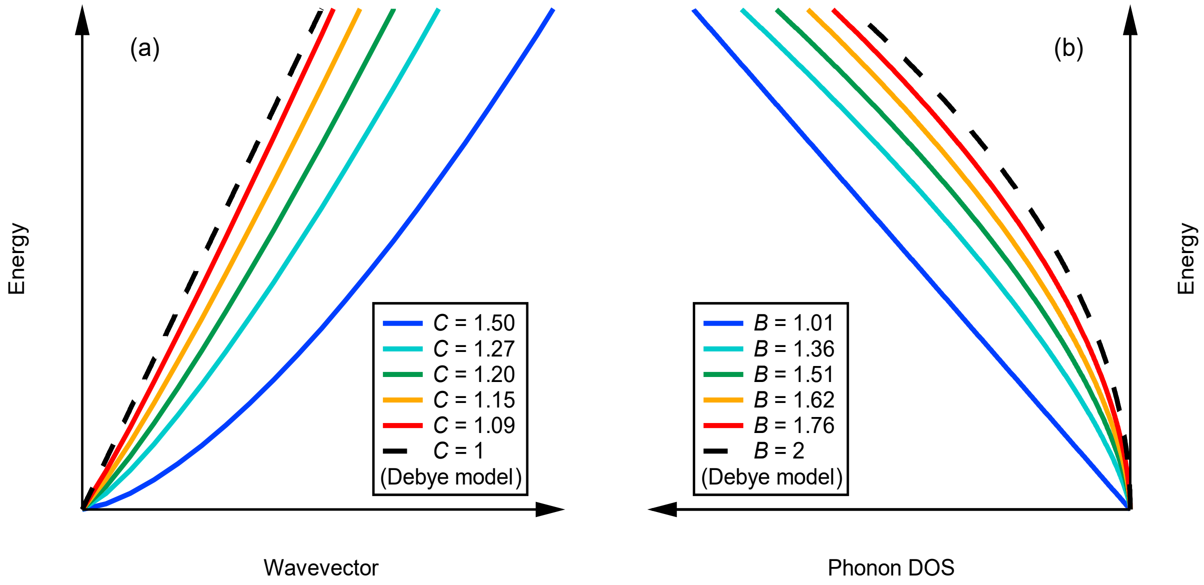

Figure 2.11 Schematic of (a) exponential phonon dispersions with different exponential terms *C*, and (b) their corresponding phonon DOSs with exponential terms *B*.

The intensity from elastic tails does not have significant effects on the fitting result, as shown by the fitting result of the elastic peak of 4 nm silicon nanocrystals at 5 K after thermal occupation correction in Figure 2.12. The fitting result indicates that the tail from the elastic scattering does not contribute to the phonon intensity in the range of interest, 6~7.75 meV, which was used to fit the power law. In addition, the phonon DOSs of bulk silicon are in good agreement with the Debye model at various temperatures, as shown in Figure 2.13, where parabolic functions were fit to the phonon DOSs of bulk silicon from 6 to 8.5 meV (bin size: 0.5 meV) at 5 and 600 K. The 5 K data was moderately smoothed using binormal smoothing to reduce fluctuation. The intensities were removed below 6 meV for E_i = 30 meV. The low energy part of the phonon DOSs of bulk silicon were extrapolated by the Debye model.

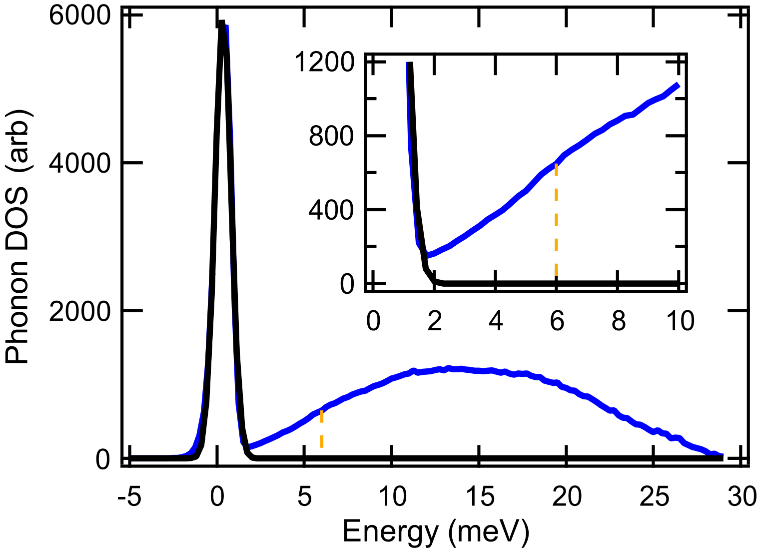

Figure 2.12 The Gaussian fit to the elastic peak shows its small contribution to the scattering intensity beyond 6 meV at 5 K for 4 nm silicon nanocrystals. The inset shows more details near the elastic peak and has the same axis labels as the main figure. The blue, and the black curves are phonon DOS of 4 nm silicon nanocrystals at 5 K, and the Gaussian fitting respectively. The dash line is guide to the eye.

TABLE 2.1. The power fittings of the phonon DOS of the low energy region in 4 nm silicon nanocrystals show the Debye model doesn't work well hereby.

Temperature (K)	DOS: Exponential term (*B*)	Calculated Dispersion: Exponential term (*C*)
5	1.01 ± 0.02	1.50
150	1.36 ± 0.04	1.27
300	1.51 ± 0.03	1.20
450	1.62 ± 0.06	1.15
600	1.76 ± 0.06	1.09

The fact that the low-energy acoustic phonon DOSs in bulk silicon are parabolic and can be well described by the Debye model indicates that the acoustic phonon branches at the low-energy limit in silicon nanocrystals are nonlinear in particular at low temperatures. Such behaviors are rarely seen in bulk lattices and allow large populations of low-energy modes. Even though the Debye model works well for the 4 nm sample at

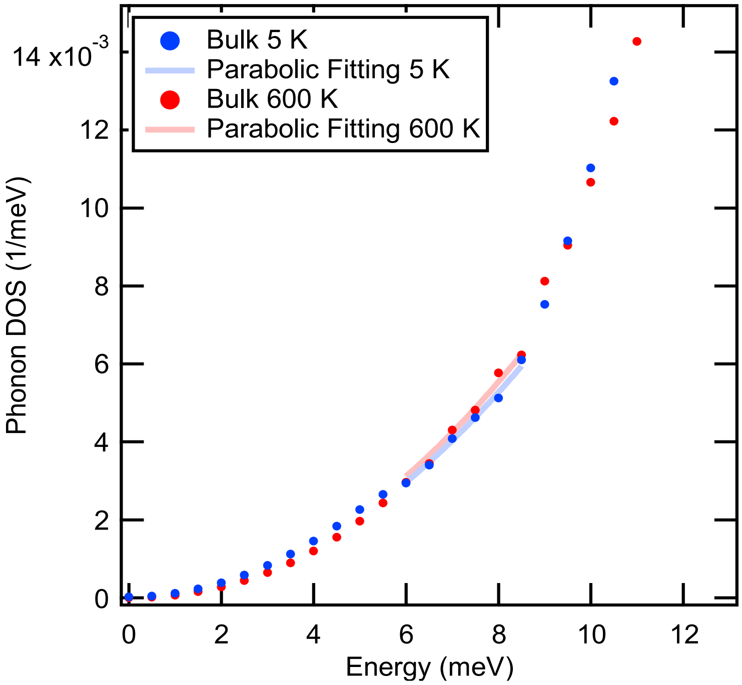

Figure 2.13 The parabolic fitting of the phonon DOSs of bulk silicon shows the elastic peaks have trivial effects on the data beyond the elastic cutoff.

600 K, the implied phonon group velocity is still lower than the bulk silicon. The results indicate that the long wavelength phonon modes are quite soft in nanocrystals at all temperatures.

2.7 Conclusion

The phonon DOSs of silicon nanocrystals at 4, 5.3, 6.5, and 7.4 nm were measured by INS from 5 to 600 K. The results agree qualitatively with molecular dynamics simulations. Phonon anharmonicity is found to be significant in small silicon nanocrystals at low temperatures, resulting from the under-constrained shell phonons. This anharmonicity decreases at elevated temperatures likely because of thermal relaxation. Gigantic size-induced softening of phonon modes below 30 meV and the universal broadening of the phonon features were observed in silicon nanocrystals and attributed to the shell modes. The increase in the Si-Si bond length towards the surface is illustrated in silicon nanocrystals using MD simulation and results in the structural variations between shell and core atoms. Enormous stiffening of phonon modes below 30 meV was observed in silicon nanocrystals with increasing temperature, in contrast with thermal phonon softening in bulk silicon. The overall phonon dynamics in silicon nanoparticles are found to be more bulk-like at elevated temperatures and their acoustic phonons are shown to be quite anharmonic with large thermal vibration amplitude. It is proposed that silicon nanocrystals might show negative thermal expansion in a broader temperature range than bulk silicon. This work provides insights into the phonon dynamics in silicon nanocrystals and other spatially confined nano materials.

2.8 References

(1) Park, J. H.; Gu, L.; Von Maltzahn, G.; Ruoslahti, E.; Bhatia, S. N.; Sailor, M. J. Biodegradable Luminescent Porous Silicon Nanoparticles for in Vivo Applications. *Nat. Mater.* **2009**, *8* (4), 331–336.

(2) Ponomareva, I.; Srivastava, D.; Menon, M. Thermal Conductivity in Thin Silicon Nanowires : Phonon Confinement Effect. *Nano Lett.* **2007**, *7* (5), 1155–1159.

(3) Alvarez, F. X.; Jou, D.; Sellitto, A. Pore-Size Dependence of the Thermal Conductivity of Porous Silicon : A Phonon Hydrodynamic Approach. *Appl. Phys. Lett.* **2010**, *97* (3), 33103.

(4) Chávez-Ángel, E.; Reparaz, J. S.; Gomis-Bresco, J.; Wagner, M. R.; Cuffe, J.; Graczykowski, B.; Shchepetov, A.; Jiang, H.; Prunnila, M.; Ahopelto, J.; Alzina, F.; Sotomayor Torres, C. M. Reduction of the Thermal Conductivity in Free-Standing Silicon Nano-Membranes Investigated by Non-Invasive Raman Thermometry. *APL Mater.* **2014**, *2* (1), 12113.

(5) Li, X.; Maute, K.; Dunn, M. L.; Yang, R. Strain Effects on the Thermal Conductivity of Nanostructures. *Phys. Rev. B* **2010**, *81* (24), 245318.

(6) Richter, A.; Steiner, P.; Kozlowski, F.; Lang, W. Current-Induced Light Emission from a Porous Silicon Device. *IEEE Electron Device Lett.* **1991**, *12* (12), 691–692.

(7) Jiang, D. T.; Coulthard, I.; Sham, T. K.; Lorimer, J. W.; Frigo, S. P.; Feng, X. H.; Rosenberg, R. A. Observations on the Surface and Bulk Luminescence of Porous Silicon. *J. Appl. Phys.* **1993**, *74* (10), 6335–6340.

(8) Pi, X. D.; Liptak, R. W.; Deneen Nowak, J.; Wells, N. P.; Carter, C. B.; Campbell, S. A.; Kortshagen, U. Air-Stable Full-Visible-Spectrum Emission from Silicon Nanocrystals Synthesized by an All-Gas-Phase Plasma Approach. *Nanotechnology* **2008**, *19* (24), 245603.

(9) Mangolini, L.; Thimsen, E.; Kortshagen, U. High-Yield Plasma Synthesis of Luminescent Silicon Nanocrystals. *Nano Lett.* **2005**, *5* (4), 655–659.

(10) de Boer, W. D. A. M.; Timmerman, D.; Dohnalová, K.; Yassievich, I. N.; Zhang, H.; Buma, W. J.; Gregorkiewicz, T. Red Spectral Shift and Enhanced Quantum Efficiency in Phonon-Free Photoluminescence from Silicon Nanocrystals. *Nat. Nanotechnol.* **2010**, *5* (12), 878–884.

(11) Wen, X.; Dao, L. Van; Hannaford, P. Temperature Dependence of Photoluminescence in Silicon Quantum Dots. *J. Phys. D. Appl. Phys.* **2007**, *40* (12), 3573–3578.

(12) Romero, J. J.; Llansola-Portolés, M. J.; Dell'Arciprete, M. L.; Rodríguez, H. B.; Moore, A. L.; Gonzalez, M. C. Photoluminescent 1–2 Nm Sized Silicon Nanoparticles: A Surface-Dependent System. *Chem. Mater.* **2013**, *25* (17), 3488−3498.

(13) Valenta, J.; Juhasz, R.; Linnros, J. Photoluminescence Spectroscopy of Single Silicon Quantum Dots. *Appl. Phys. Lett.* **2002**, *80* (6), 1070–1072.

(14) Brus, L. Luminescence of Silicon Materials: Chains, Sheets, Nanocrystals, Nanowires, Microcrystals, and Porous Silicon. *J. Phys. Chem.* **1994**, *98* (14), 3575–3581.

(15) Meier, C.; Lüttjohann, S.; Kravets, V. G.; Nienhaus, H.; Lorke, A.; Wiggers, H. Raman Properties of Silicon Nanoparticles. *Phys. E Low-dimensional Syst. Nanostructures* **2006**, *32* (1), 155–158.

(16) Kohno, H.; Iwasaki, T.; Mita, Y.; Takeda, S. One-Phonon Raman Scattering Studies of Chains of Crystalline-Si Nanospheres. *J. Appl. Phys.* **2002**, *91* (5), 3232–3235.

(17) Adu, K. W.; Gutiérrez, H. R.; Kim, U. J.; Sumanasekera, G. U.; Eklund, P. C. Confined Phonons in Si Nanowires. *Nano Lett.* **2005**, *5* (3), 409–414.

(18) Sagar, D. M.; Atkin, J. M.; Palomaki, P. K. B.; Neale, N. R.; Blackburn, L.; Johnson, J. C.; Nozik, A. J.; Raschke, M. B.; Beard, M. C. Quantum Confined Electron–Phonon Interaction in Silicon Nanocrystals. *Nano Lett.* **2015**, *15* (3), 1511–1516.

(19) Lopez, T.; Mangolini, L. On the Nucleation and Crystallization of Nanoparticles in Continuous-Flow Nonthermal Plasma Reactors. *J. Vac. Sci. Technol. B* **2014**, *32* (6), 61802.

(20) Mangolini, L.; Thimsen, E.; Kortshagen, U. High-Yield Plasma Synthesis of Luminescent Silicon Nanocrystals. *Nano Lett.* **2005**, *5* (4), 655–659.

(21) Lin, J. Y. Y.; Banerjee, A.; Islam, F.; Le, M. D.; Abernathy, D. L. Energy Dependence of the Flux and Elastic Resolution for the ARCS Neutron Spectrometer. *Phys. B Condens. Matter* **2019**, *562*, 26–30.

(22) Seeger, P. A.; Daemen, L. L.; Larese, J. Z. Resolution of VISION, a Crystal-Analyzer Spectrometer. *Nucl. Instruments Methods Phys. Res. Sect. A Accel. Spectrometers, Detect. Assoc. Equip.* **2009**, *604* (3), 719–728.

(23) Taylor, J.; Arnold, O.; Bilheaux, J.; Buts, A.; Campbell, S.; Doucet, M.; Draper, N.; Fowler, R.; Gigg, M.; Lynch, V.; Markvardsen, A.; Palmen, K.; Parker, P.; Peterson, P.; Ren, S.; Reuter, M.; Savici, A.; Taylor, R.; Tolchenov, R.; Whitley, R.; Zhou, W, J. *Mantid, A High Performance Framework for Reduction and Analysis of Neutron Scattering Data*; 2012.

(24) Kresch, M.; Delaire, O.; Stevens, R.; Lin, J. Y. Y.; Fultz, B. Neutron Scattering Measurements of Phonons in Nickel at Elevated Temperatures. *Phys. Rev. B* **2007**, *75* (10), 104301.

(25) Lucas, M. S.; Kresch, M.; Stevens, R.; Fultz, B. Phonon Partial Densities of States and Entropies of Fe and Cr in Bcc Fe-Cr from Inelastic Neutron Scattering. *Phys. Rev. B* **2008**, *77* (18), 184303.

(26) Delaire, O.; Kresch, M.; Muñoz, J. A.; Lucas, M. S.; Lin, J. Y. Y.; Fultz, B. Electron-Phonon Interactions and High-Temperature Thermodynamics of Vanadium and Its Alloys. *Phys. Rev. B* **2008**, *77* (21), 214112.

(27) Harten, U.; Toennies, J. P.; Wöll, C.; Miglio, L.; Ruggerone, P.; Colombo, L.; Benedek, G. Surface Phonons in Si(111)+ H(1 X 1). *Phys. Rev. B* **1988**, *38* (5), 3305–3310.

(28) Chabal, Y. J. Infrared Spectroscopy of Hydrogen on Silicon Surfaces. *Phys. B Condens. Matter* **1991**, *170* (1), 447–456.

(29) Kong, L. T. Phonon Dispersion Measured Directly from Molecular Dynamics Simulations. *Comput. Phys. Commun.* **2011**, *182* (10), 2201–2207.

(30) Kong, L. T.; Denniston, C.; Müser, M. H. An Improved Version of the Green' s Function Molecular Dynamics Method. *Comput. Phys. Commun.* **2011**, *182* (2), 540–541.

(31) Martyna, G. J.; Tobias, D. J.; Klein, M. L. Constant Pressure Molecular Dynamics Algorithms. *J. Chem. Phys.* **1994**, *101* (5), 4177–4189.

(32) Kong, L. T.; Bartels, G.; Campañá, C.; Denniston, C.; Müser, M. H. Implementation of Green' s Function Molecular Dynamics : An Extension to LAMMPS. *Comput. Phys. Commun.* **2009**, *180* (6), 1004–1010.

(33) Campañá, C.; Müser, M. H. Practical Green's Function Approach to the Simulation of Elastic Semi-Infinite Solids. *Phys. Rev. B* **2006**, *74* (7), 75420.

(34) Tersoff, J. New Empirical Approach for the Structure and Energy of Covalent Systems. *Phys. Rev. B* **1988**, *37* (12), 6991–7000.

(35) Valentin, A.; Sée, J.; Galdin-Retailleau, S.; Dollfus, P. Study of Phonon Modes in Silicon Nanocrystals Using the Adiabatic Bond Charge Model. *J. Phys. Condens. Matter* **2008**, *20* (14), 145213.

(36) Hu, X.; Zi, J. Reconstruction of Phonon Dispersion in Si Nanocrystals. *J. Phys. Condens. Matter* **2002**, *14* (41), L671–L677.

(37) Kim, D. S.; Smith, H. L.; Niedziela, J. L.; Li, C. W.; Abernathy, D. L.; Fultz, B. Phonon Anharmonicity in Silicon from 100 to 1500 K. *Phys. Rev. B* **2015**, *91* (1), 14307.

(38) Meyer, R.; Prakash, S.; Entel, P. Capillary Pressure and Phonons in Ag, Au, Cu and Ni Nanoparticles. *Phase Transitions* **2002**, *75* (1–2), 51–58.

(39) Zachariah, M. R.; Carrier, M. J.; Blaisten-Barojas, E. Properties of Silicon Nanoparticles : A Molecular Dynamics Study. *J. Phys. Chem.* **1996**, *100* (36),

(40) Meyer, R.; Comtesse, D. Vibrational Density of States of Silicon Nanoparticles. *Phys. Rev. B* **2011**, *83* (1), 14301.

(41) Benedek, G.; Toennies, J. P.; Nature., S. *Atomic Scale Dynamics at Surfaces : Theory and Experimental Studies with Helium Atom Scattering*; Springer-Verlag GmbH Germany, part of Springer Nature: Berlin, 2018.

(42) Weinstein, B. A.; Piermarini, G. J. Raman Scattering and Phonon Dispersion in Si and GaP at Very High Pressure. *Phys. Rev. B* **1975**, *12* (4), 1172–1186.

(43) Ferry, D. K.; Oda, S. *Silicon Nanoelectronics*; 2017.

(44) Saleh, B. E. A. *Fundamentals of Photonics*; 2019.

(45) Yang, L. Phonon Transport in Nanowires – Beyond Classical Size Effects, 2019.

(46) Estreicher, S. K.; Gibbons, T. M.; Kang, B.; Bebek, M. B. Phonons and Defects in Semiconductors and Nanostructures : Phonon Trapping , Phonon Scattering , and Heat Flow at Heterojunctions. *J. Appl. Phys.* **2014**, *115* (1), 12012.

(47) Lim, J.; Hippalgaonkar, K.; Andrews, S. C.; Majumdar, A.; Yang, P. Quantifying Surface Roughness Effects on Phonon Transport in Silicon Nanowires. *Nano Lett.* **2012**, *12* (5), 2475–2482.

(48) Dhital, C.; Abernathy, D. L.; Zhu, G.; Ren, Z.; Broido, D.; Wilson, S. D. Inelastic Neutron Scattering Study of Phonon Density of States in Nanostructured $Si_{1-x}Ge_x$ Thermoelectrics. *Phys. Rev. B* **2012**, *86* (21), 214303.

(49) Ibach, H. Thermal Expansion of Silicon and Zinc Oxide (I). *Phys. status solidi* **1969**, *31* (2), 625–634.

(50) Gibbons, D. F. Thermal Expansion of Some Crystals with the Diamond Structure. *Phys. Rev.* **1958**, *112* (1), 136–140.

(51) Shah, J. S.; Straumanis, M. E. Thermal Expansion Behavior of Silicon at Low Temperatures. *Solid State Commun.* **1972**, *10* (1), 159–162.

(52) Middelmann, T.; Walkov, A.; Bartl, G.; Schödel, R. Thermal Expansion Coefficient of Single-Crystal Silicon from 7 K to 293 K. *Phys. Rev. B* **2015**, *92* (17), 174113.

(53) Okada, Y.; Tokumaru, Y. Precise Determination of Lattice Parameter and Thermal Expansion Coefficient of Silicon between 300 and 1500 K. *J. Appl. Phys.* **1984**, *56* (2), 314–320.

(54) Slack, G. A.; Bartram, S. F. Thermal Expansion of Some Diamondlike Crystals. *J. Appl. Phys.* **1975**, *46* (1), 89–98.

(55) Batchelder, D. N.; Simmons, R. O. Lattice Constants and Thermal Expansivities of Silicon and of Calcium Fluoride between 6° and 322°K. *J. Chem. Phys.* **1964**, *41* (8), 2324–2329.

(56) Li, W.-H.; Wu, S. Y.; Yang, C. C.; Lai, S. K.; Lee, K. C.; Huang, H. L.; Yang, H. D. Thermal Contraction of Au Nanoparticles. *Phys. Rev. Lett.* **2002**, *89* (13), 135504.

Chapter 3

Distinct Acoustic and Optical Phonon Responses to Particle Size, Oxidation, and Temperature in Silicon Nanocrystals

3.1 Abstract

Phonon, as an important momentum carrier, may play an important role in the photoluminescence of silicon nanocrystals. However, systematic experimental study on phonon dynamics in spatially confined silicon systems remains limited. We used inelastic neutron scattering to investigate particle size, oxidation, and temperature effects on phonon dynamics of silicon nanocrystals by measuring the phonon density of states of 12 and 50-nm silicon nanocrystals with several oxidation levels at different temperatures. We found transverse acoustic phonon modes have much stronger responses to particle size, oxidation, and temperature than optical phonon modes. In specific, the strong acoustic phonon response to temperature suggests modulations of phonon group velocity. At intermediate temperature, we observed a large difference between vibrational entropies of silicon nanocrystals and bulk silicon. Our results shed light on the phonon dynamics of silicon-based functional nanomaterials and facilitate further theoretical investigation on the electron-phonon interaction of spatially confined silicon systems.

3.2 Introduction

Spatially confined silicon systems have drawn an increasing amount of attention since the last century owing to their significantly higher emission efficiencies of photoluminescence (PL) than their bulk counterparts.[1–5] Nowadays luminescent silicon nanocrystals are widely used in bio and cellular imaging industries as bio-compatible, non-toxic, and bio-degradable theranostic agents.[6–13] PL of silicon nanocrystals also grants them tremendous potential in optoelectronic applications.[14–19] Although many theories of PL of silicon nanocrystals were presented in previous studies, the mechanism of PL has remained a subject of discussion.[20–26] A better physical understanding of silicon nanocrystals may prompt a revolutionary development of quantized silicon-based applications.

PL spectrum of silicon nanocrystals was related to both intrinsic and extrinsic effects. Intrinsically, it was commonly related to quantum confinement.[12,27–31] Previous works showed that strong quantum confinement in silicon increases the probability of radiative recombination through the direct bandgap transitions and reduces phonon-assisted indirect bandgap transitions.[29,32] Extrinsically, surface effects including but not limited to the surface-mediated direct-like emission, the surface chemistry, defects, and impurities were related to PL of spatially confined silicon systems.[33–38]

Evidence shows phonon can play an important role in the PL of silicon nanocrystals. Studies show the PL lifetime in spatially confined silicon is typically very long - approximately 3 orders of magnitude longer than those of direct bandgap semiconductors.[3,31,39–43] PL observed under resonant excitation was also related to transverse optical and transverse acoustic (TA) phonon modes of bulk crystalline silicon by many studies to account for momentum-conservation.[43–45] Additionally, the temperature dependence of PL of silicon nanocrystals, such as the emission wavelength, also supports the phonon-assisted indirect transition.[41,46] Furthermore, the importance of electron-phonon coupling in the PL of silicon nanocrystals was also shown by experiments and calculations.[47,48] Yet, systematic experimental study on phonon dynamics in spatially confined silicon systems remains limited.

In this chapter, the phonon density of states (DOS) of 12 and 50-nm silicon nanocrystals with several oxidation levels are measured by inelastic neutron scattering (INS). Particle size, oxidation, and temperature effect on phonon dynamics in silicon nanocrystals are studied with the help of molecular dynamic (MD) simulations based on empirical potentials and first-principles calculations based on density functional theories. Shell-core models are proposed to interpret experimental results. Large particle sizes of nanocrystal samples were targeted for two primary reasons. Firstly, we find large nanocrystal size grants us better control over their oxidation levels by adjusting the exposure time during experiments. In contrast, it is harder to control the oxidation level of small nanocrystals because they tend to get oxidized more rapidly and the hydrogen terminations on their surface likely expedite the oxidation process thanks to their relatively large surface-area-to-volume ratios. Secondly, we would like to qualitatively investigate the nature of lattice vibrations of large silicon nanocrystals by comparing them with those of smaller silicon nanocrystals and bulk silicon. This work provides valuable phonon information in spatially confined silicon systems and contributes to further investigation of the role of phonon in the PL of silicon-based functional nanomaterials.

3.3 Materials and methods

The 12 and 50-nm silicon nanocrystals were synthesized by a non-thermal plasma process.[49,50] The fabrication details are described in our previous paper and Chapter 2.[51] The surfaces of the as-produced silicon nanocrystals were terminated by hydrogen atoms. The as-produced 12-nm samples were divided into three batches and treated to achieve different oxidation levels. One batch of the 12-nm silicon nanocrystals was kept sealed after the fabrication to minimize oxidation and was named Sample A (12-nm, 585 mg). The other two batches of the 12-nm silicon nanocrystals were baked in a furnace in the presence of air to get their surface oxidized. The oxidation levels were controlled by adjusting the operation time. The two oxidized samples were named Sample B (12-nm, 630 mg) and C (12-nm, 605 mg), respectively. The 50-nm silicon nanocrystals were slightly oxidized and were named Sample D (50-nm, 640 mg). The oxidation levels of Sample B, C, and D were estimated to be 5%, 15%, and 3%, respectively, using the energy dispersive spectroscopy (EDS). Sample A, which was carefully sealed and expected to have a low oxidation level, was not measured by EDS to avoid exposure to air.

INS measurements were performed on the Wide Angular-Range Chopper Spectrometer (ARCS), a direct geometry chopper neutron spectrometer at Oak Ridge

National Laboratory. All the samples were loaded in a 3/8-inch diameter aluminum can. ARCS has an energy resolution of 4% or better of the neutron incident energy (E_i).[52] Neutron beams with E_i of 30, 90, and 150 meV were chosen to optimize the energy resolution and range. Sample A was measured at 10, 150, and 300 K. Sample B, C, and D were measured at 300 K.

3.4 Data processing

Mantid software was used for data processing.[53] The event data of ARCS measurement contains information about the detector number and the time of arrival of each scattered neutron. The momentum (q) and energy (E) transfer of each neutron were calculated from its time-of-flight and scattering geometry, with the knowledge of the distance between detectors and the sample to generate the scattering intensity S(q, E). Backgrounds from an empty can were subtracted from the signals. The phonon spectra were analyzed within the incoherent approximation, which has been shown to work reliably.[54–56] Neutron signal was normalized by currents. Elastic intensities were removed below 5, 7, and 10 meV for E_i = 30, 90, and 150 meV, respectively. The low-energy phonon DOSs below the corresponding elastic cutoff (used to remove elastic background) were extrapolated by parabolic functions using the Debye model. The energy step sizes of 0.3, 1, and 1.5 meV were used for E_i = 30, 90, and 150 meV, respectively. Due to the small effective sample thickness, no multiple scattering correction is necessary. Multi-phonon scattering correction was performed by an iterative method considering the S(q, E) and the multi-phonon expansion.[54] The phonon spectra were also corrected for the thermal occupation.

3.5 Calculation

3.5.1 Molecular dynamic simulations

3.5.1.1 Unoxidized Nanocrystal model

MD simulations were used to study the stricture and the dynamic of unoxidized silicon nanocrystals. The 3-nm diameter spherical silicon nanocrystal consisting of 705 silicon atoms in a 20×20×20 nm^3 cube was used as a model system (UN model). The small size of the nanocrystal in this model was chosen for reasonable computation cost. The initial structure of the silicon nanocrystal in the model is identical to crystalline silicon ($Fd\bar{3}m$) with a lattice parameter of 5.431 Å. The atomic structure and phonon DOS of this model were calculated using the LAMMPS and Phana packages[57] based on 3-body Tersoff potential with an interaction cutoff distance of 3.7 Å.[58] The initial velocities of the atoms in this model were generated in a Gaussian distribution at 300 K. The linear and angular momentum of the initially created ensemble of atomic velocities were zeroed. The atomic positions and velocities in this model were updated every 1 fs by performing time integration on Nose-Hoover style non-Hamiltonian equations of motion under an isothermal and isochoric condition. The temperature relaxation parameter was set as 0.1 ps. The calculated trajectories were then used to analyze atomic structures, as well as compute phonon dynamical matrix based on the fluctuation-dissipation theory.[51] Normalized phonon DOSs were obtained by evaluating the eigenvalues of the dynamical matrix at the Brillouin zone center after equilibrium, which takes about fifty nanoseconds, was reached.

3.5.1.2 Oxidized Nanocrystal model

MD simulations were also used to study the oxidization effect on silicon nanocrystals. A similar model, in which the silicon nanocrystal was partially oxidized, was used in the simulation (ON model). To make the thickness of the oxidized shell of the nanocrystal in this model close to that in Sample C (12-nm, nominally 15% oxidized), a partially oxidized 3-nm nanocrystal ($Si_{583}O_{609}$) model was constructed by substituting the structure within 1-nm from the center of a relaxed 3-nm α-quartz ($P3_121$) nanocrystal $Si_{499}O_{756}$ with crystalline silicon. The regions within and beyond 1 nm from the center of this nanocrystal are defined as its core and shell region, respectively. The atomic structure and phonon DOS of this model were calculated based on 3-body Tersoff interatomic potential for Si–O with similar methods.[59]

3.5.1.3 Crystalline model

The atomic structure and the phonon DOS of crystalline silicon were also calculated by MD simulation for comparison. The simulation was performed on a 4 × 4 × 4 silicon supercell of 512 silicon atoms with periodic boundary conditions (Crystalline model). The phonon DOS was computed by evaluating the eigenvalues on points sampled by a Monkhorst-Pack mesh.

3.5.2 First-principles calculations

Phonon dynamics and mode isothermal Grüneisen parameters of crystalline silicon were calculated using VASP and Phonopy based on DFT with GGA projector augmented wave potential and quasi-harmonic approximation (QHA).[60,61] In DFT calculation, a 2 × 2 × 2 relaxed silicon ($Fd\bar{3}m$) supercell with the lattice parameter of 5.434 Å was used as a model to calculate force sets, from which a dynamical matrix was computed. Phonon DOS and dispersion of crystalline silicon were calculated from the dynamical matrix with a q-mesh of 31 × 31 × 31 and along high symmetry directions, respectively. The mode isothermal Grüneisen parameters were obtained from DFT calculations with QHA on smaller and larger unit cells with 1% differences in lattice parameters. The phonon DOS of α-quartz ($P3_121$) was also calculated using DFT in similar methods for comparison.

3.6 Result and discussion

The phonon DOSs of silicon nanocrystals as well as the phonon DOS of bulk silicon from our previous work[51] were shown in Figure 3.1(a-c), where outstanding phonon peaks at 78 meV are longitudinal and shear modes of the Si-H bond.[62] They were fitted with Gaussian functions and subtracted, as shown in Figure 3.1 (b). The atomic concentration of hydrogen in Sample A was estimated by comparing the population of hydrogen-related and silicon-related phonon states with

$$\frac{C_H}{C_{Si}} = \frac{\sigma_{Si} A_H \sqrt{M_H}}{\sigma_H A_{Si} \sqrt{M_{Si}}} \tag{3.1}$$

where C, σ, A, and M are the atomic concentrations, neutron scattering cross-sections, areas in neutron-weighted phonon DOS, and atomic masses of hydrogen and silicon, respectively. Using the area of the Gaussian fit to the hydrogen-related peak in Sample A at 78 meV as A_H and the residual after subtraction as A_{Si}, the atomic concentration of hydrogen in Sample A was estimated to be 2%. The hydrogen concentrations in Samples A, B, C, and D are in descending order. The result underestimates the hydrogen concentration by considering only one hydrogen-related peak. Other hydrogen-related modes including Si-H_2 scissor at 111 meV and Si–H_x stretching mode at 270 meV contribute much less due to the low hydrogen concentration.[26,62] The light atomic mass and the large neutron scattering cross-section of hydrogen are responsible for the outstanding hydrogen-related phonon peaks though the hydrogen concentrations of our samples are low.

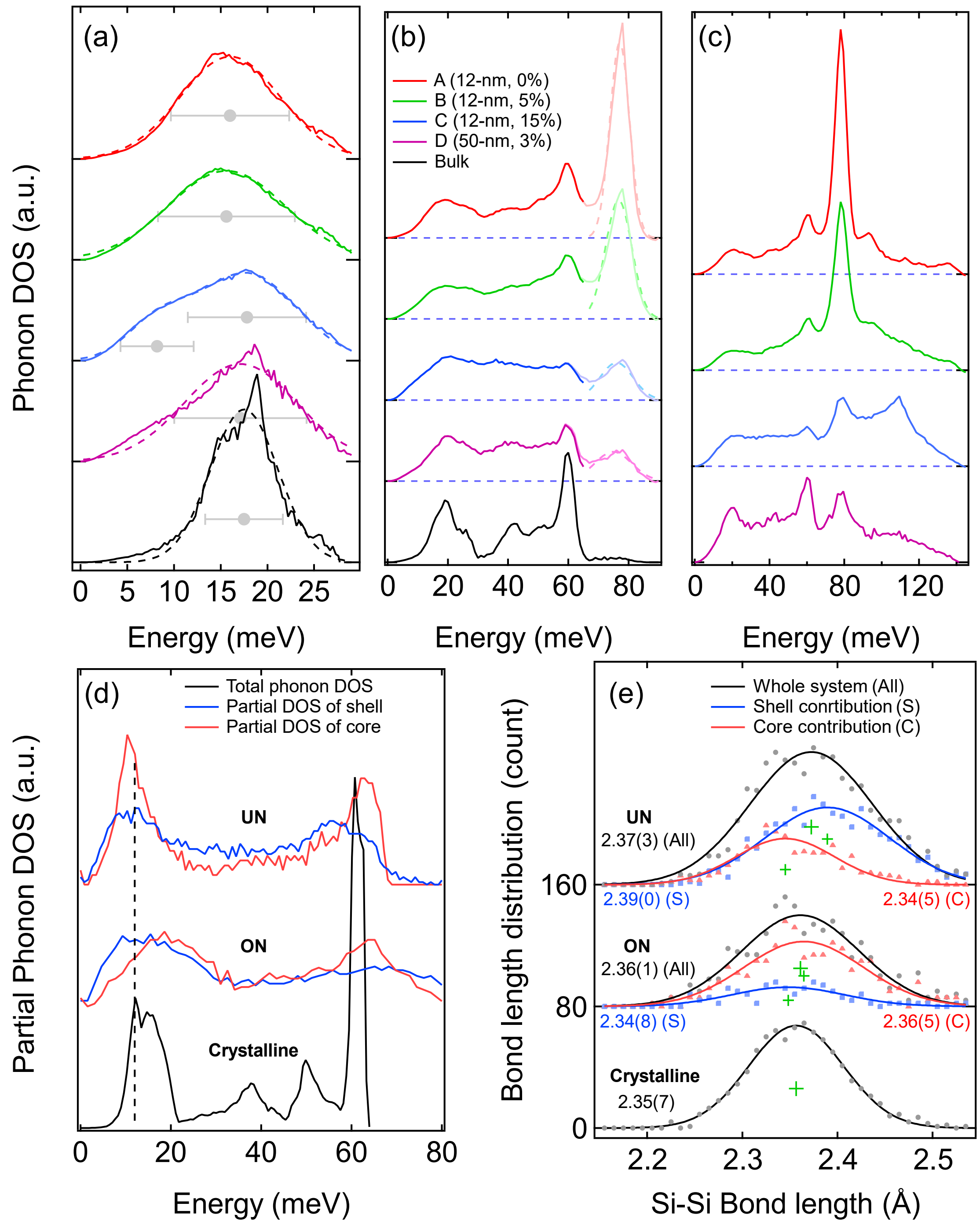
(a)
Phonon DOS (a.u.)
0
5
10
15
20
25
Energy (meV)
(b)
A (12-nm, 0%)
B (12-nm, 5%)
C (12-nm, 15%)
D (50-nm, 3%)
Bulk
0
20
40
60
80
Energy (meV)
(c)
0
40
80
120
Energy (meV)
(d)
Total phonon DOS
Partial DOS of shell
Partial DOS of core
UN
ON
Crystalline
Partial Phonon DOS (a.u.)
0
20
40
60
80
Energy (meV)
(e)
Whole system (All)
Shell conrtibution (S)
Core contribution (C)
UN
2.37(3) (All)
2.39(0) (S)
2.34(5) (C)
ON
2.36(1) (All)
2.34(8) (S)
2.36(5) (C)
Crystalline
2.35(7)
160
80
0
Bond length distribution (count)
2.2
2.3
2.4
2.5
Si-Si Bond length (Å)

Figure 3.1 (a) Normalized phonon DOSs measured with E_i = 30 meV (solid lines) at 300 K. Grey dots with error bar show the center and the FWHM of the Gaussian fits (dash lines) to TA modes. (b) Phonon DOSs measured with E_i = 90 meV (solid lines) at 300 K. Percentages in the legend are nominal oxidization levels determined by energy dispersive spectroscopy. The hydrogen-related phonon peaks at 78 meV were fitted with Gaussian functions (dim-colored dash lines) and subtracted. Hydrogen atomic concentrations of our samples were estimated to be lower than 2%. Residual phonon DOSs were normalized to unity between 0 and 65 meV. (c) Normalized phonon DOSs measured with E_i = 150 meV at 300 K. (d) Normalized MD simulated partial phonon DOSs. The core region of the ON model is 23% oxidized during simulation, as discussed in the text. (e) Gaussian fits to the MD simulated Si-Si bond length distributions show heterostructures of shell-core models. The fitting uncertainties are shown in the parentheses. (S) and (C) stand for shell and core regions, respectively. Average bond lengths in different regions are marked by green crosses. The populations of Si-Si bond in the oxidized cluster are scaled for comparison.

We found particle size has stronger effects on the TA phonon (below 30 meV) profile than the optical phonon (at 60 meV) profile of silicon nanocrystals, as shown in Figure 3.1(a-c).[63–65] The size effect is illustrated by comparing the phonon DOSs of 12-nm (Sample A) and 50-nm silicon nanocrystals (Sample D), as well as the phonon DOS of bulk silicon from our previous work.[51] Surprisingly, phonon DOSs of both 12 and 50-nm silicon nanocrystals are greatly different from that of bulk silicon. This implies that the lattice vibrations of large silicon nanocrystals are still substantially different from those of bulk silicon. As particle size decreases, the silicon phonon profile becomes broader, the TA phonon peak shifts to lower energies while the optical phonon peak center remains mostly unchanged. The size-dependent evolutions of the phonon DOSs of our samples agree with our prior observations.[51]

We calculated phonon DOSs of nano-sized silicon models using MD simulations to better understand the particle size effect on the phonon dynamics of silicon nanocrystals. Unoxidized silicon nanocrystals were studied with a 3-nm diameter silicon sphere (UN model for Unoxidized Nanocrystal model). The small size of the model was chosen to reduce computation costs. To account for the heterostructure and study phonon dynamics of the near-center and the near-surface regions of silicon nanocrystals separately, the UN model is divided into two spatial regions. The regions within and beyond 1 nm from the center of the UN model are defined as its core region and shell region, respectively.[51] The phonon DOS of crystalline silicon (Crystalline model) was also calculated using MD simulation for comparison. The details of our models and calculation setups are described in section 3.5.

MD simulations reveal great vibrational differences between the core region and the shell region of the UN model, as shown in Figure 3.1(d). The simulated partial phonon DOS of the core region of the UN model resembles that of the Crystalline model while the simulated phonon DOS of the shell region of the UN model has a significantly broader profile than that of the Crystalline model. Additionally, the simulated TA phonon energies of both core and shell regions of the UN model are smaller than those of the Crystalline model. By applying the relative TA phonon energy shift from the crystalline value (∂E/E) and the relative volume change extracted from MD simulations to Equation (3.2):

$$\gamma_i = -\frac{a^3 \cdot \partial E_i}{E_i \cdot \partial a^3} \tag{3.2}$$

where a is MD simulated average Si-Si bond lengths in Figure 3.1 (e), we calculated the Grüneisen parameter of the UN model. The calculated TA Grüneisen parameter of the shell region of the UN model is 6.8, which is greatly different from and has the opposite sign to the first-principles calculated crystalline results, as shown in Figure 3.1 (a).[66–68] Such dramatically different Grüneisen parameters indicate that the shell region of the UN model and the Crystalline model have significantly different phonon responses to the volume change. Assuming the thickness of the shell region does not vary strongly with nanocrystal size, we expect the partial phonon DOS of the shell region to become dominant for small silicon nanocrystals whose surface-area-to-volume ratios are large. This agrees with the experimentally observed phonon broadening and energy decrease of TA phonon with decreasing nanocrystal size. In contrast, the phonon broadening from the reduced phonon lifetime by boundary scattering in 12-nm nanocrystals (Sample A,) is small and estimated to be 0.2 meV using 12-nm as the upper limit of phonon mean-free-path and the same method in our previous work.[51] Contributions from particle size distribution and surface roughness to the broadening of the phonon DOS of our samples are expected to be small.

We compared Si-Si bond length distributions, which directly relate to interatomic interactions and local phonon modes, extracted from MD simulations to better understand optical phonons, as shown in Figure 3.1 (e). The peak center of the Gaussian fit to the MD simulated Si-Si bond length distributions of the Crystalline model is 2.357 ± 0.005 Å, which agrees with the reported value.[69] The simulated average Si-Si bond lengths of both the UN model's core (0.4% smaller) and shell (1.3% larger) regions are similar to that of the Crystalline model, which likely accounts for similar optical phonon behaviors in these two systems. This agrees with the size-independent optical phonon energy from our INS observations. Additionally, the simulated FWHM (Full Width at Half Maximum) of Si-Si bond length distributions in the UN model's shell region is 31% larger than that of the Crystalline model. Such big structural differences account for the great differences in the simulated phonon profiles between the shell region of the UN model and the Crystalline model.

Similar to the particle size effect, we found oxidation also has stronger effects on the TA phonon profile than the optical phonon profile of silicon nanocrystals. The oxidation effect is illustrated by comparing the measured phonon DOSs of 12-nm Sample A, B, and C with ascending oxidation levels, as shown in Figure 3.1 (a-c). At a higher oxidation level, the phonon profile becomes broader, the TA phonon peak splits while the optical peak center remains unchanged. Additionally, oxygen-related phonon modes begin to show up at higher oxidation levels. For example, the gigantic peak at 110 meV in the phonon DOS of Sample C is the bond bending mode of the Si-H group in the HSi-O_3 configuration, as shown in Figure 3.1 (c).[70]

We built a partially oxidized 3-nm diameter silicon sphere (ON model for Oxidized Nanocrystal model) by substituting the silicon structure in the shell region of the UN model with α-quartz to study the oxidation effect on silicon nanocrystals. Definitions of the core and the shell region of the ON model are identical to those of the UN model. The MD simulated partial phonon DOS of the oxidized shell region of the ON model has a broader profile than that of the unoxidized shell region of the UN model due to oxygen-related modes, as shown in Figure 3.1 (d). This shows the oxygen-related phonon modes in the near-surface region of silicon nanocrystals will lead to phonon broadening, which agrees with our experimental observation. Additionally, the simulated average Si-Si bond length of the ON model is also similar (the difference is smaller than the uncertainty) to that of the Crystalline model, which likely leads to similar optical peaks (silicon-silicon modes) centered at 60 meV. This agrees with the oxidation-independent optical phonon energy from our INS observations.

The simulated partial phonon DOS of the core region of the ON model is different from the crystalline pattern due to the invasion of relaxed oxygen atoms from the oxidized shell region of the ON model during MD simulation. MD results show the atomic concentration of oxygen in the core region of the ON model is 23%. This partial oxidization also accounts for the larger simulated average Si-Si bond length (0.8%) and FWHM (20%) of the Si-Si bond distribution of the core region of the ON model than those of the unoxidized core region of the UN model, as shown in Figure 3.1 (e). We expect interatomic interactions, which account for optical phonon modes, in the unoxidized core region of a partially oxidized silicon nanocrystal to behave like those of crystallin silicon and to have small responses to near-surface oxidization.

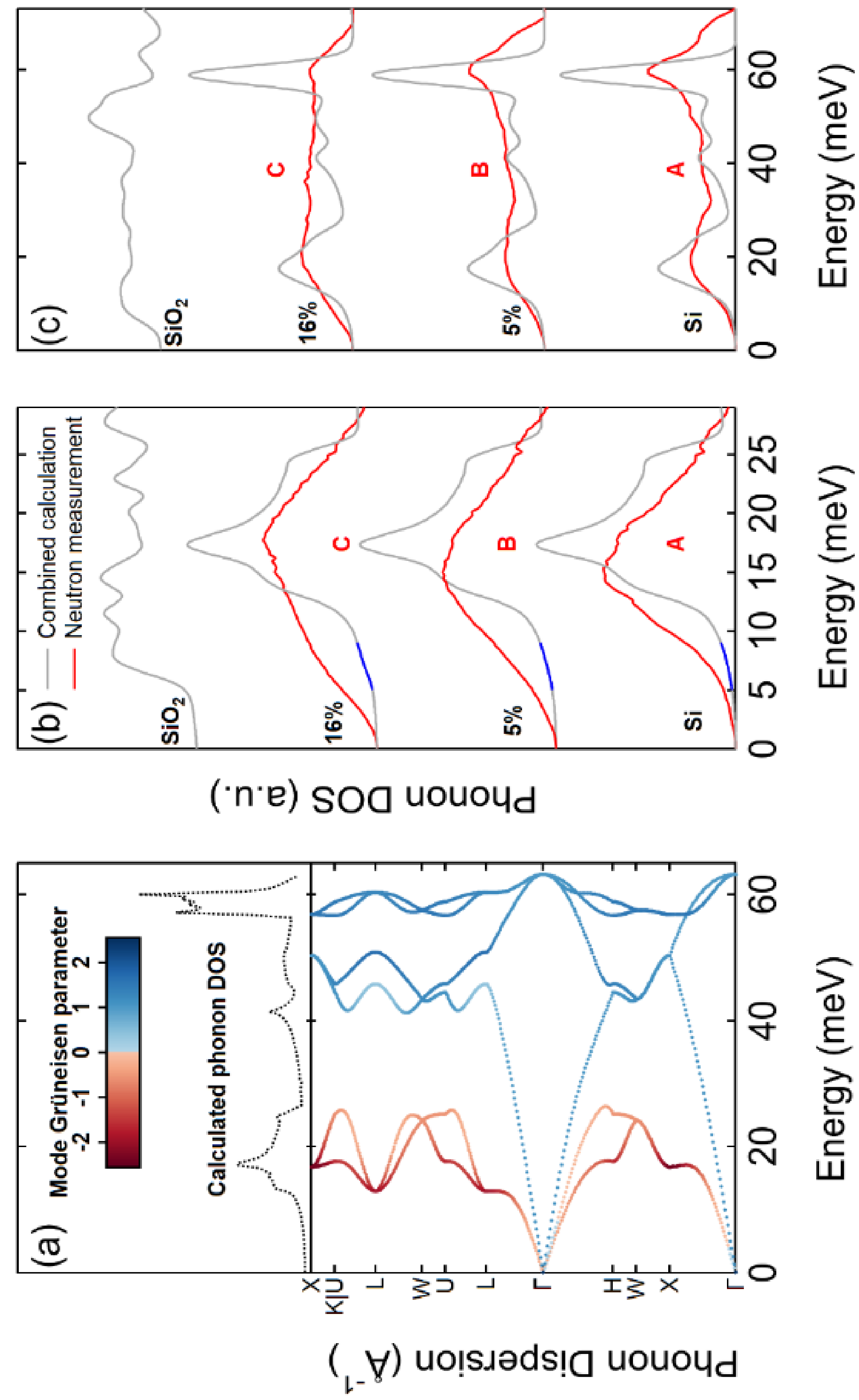
(a)
Mode Grüneisen parameter
-2 -1 0 1 2
Calculated phonon DOS
Phonon Dispersion (Å⁻¹)
X K|U L W U L Γ H W X Γ
0 20 40 60
Energy (meV)
(b)
Combined calculation
Neutron measurement
SiO₂
16%
5%
Si
C
B
A
0 5 10 15 20 25
Energy (meV)
Phonon DOS (a.u.)
(c)
SiO₂
16%
5%
Si
C
B
A
0 20 40 60
Energy (meV)

Figure 3.2 (a) First-principles calculated phonon DOS and isothermal mode Grüneisen parameters of crystalline silicon. (b, c) Combined first-principle calculated phonon DOSs (black lines) and measured phonon DOSs (red lines) with E_i = 30 and 90 meV. DFT results are convoluted with instrument resolution functions of ARCS. Percentages show atomic ratios of oxygen. Blue curves in (b) highlight the calculated changes of phonon DOS induced by oxygen-related modes.

We attribute the split of the TA phonon peak at a high oxidation level to energy differences between phonon modes of the unoxidized near-center region and the partially oxidized near-surface region of our samples. This is illustrated by comparing our measurements to a set of phonon DOSs obtained by combining first-principles calculated phonon DOSs of crystalline silicon and α-quartz with different ratios. Calculation details are described in section 3.5. The results are shown in Figure 3.2(b, c). Sample A, B, and C's phonon peaks centered at 17 meV are in agreement with the phonon profiles of the combined phonon DOSs and do not show strong oxidation dependence. We attribute these peaks to the TA phonon modes of the unoxidized core regions of our samples. On the other hand, Sample C's phonon peak centered at 7 meV is identified as an oxygen-related mode and is attributed to shell oxidation. Although phonon DOSs of Sample A, B, and C from our measurement show great oxidation-induced changes, the oxidation effects predicted by first-principles calculation are subtle. This is likely because the oxidized structures in our samples are less ordered than the oxidized structure (α-quartz) we used in the calculation. Phonon peak energies, such as the optical phonon peak at 60 meV, of the combined (calculated) phonon DOSs, are slightly different from those from our measurements likely because the relaxed lattice parameter used in calculations is slightly larger than those of our samples.

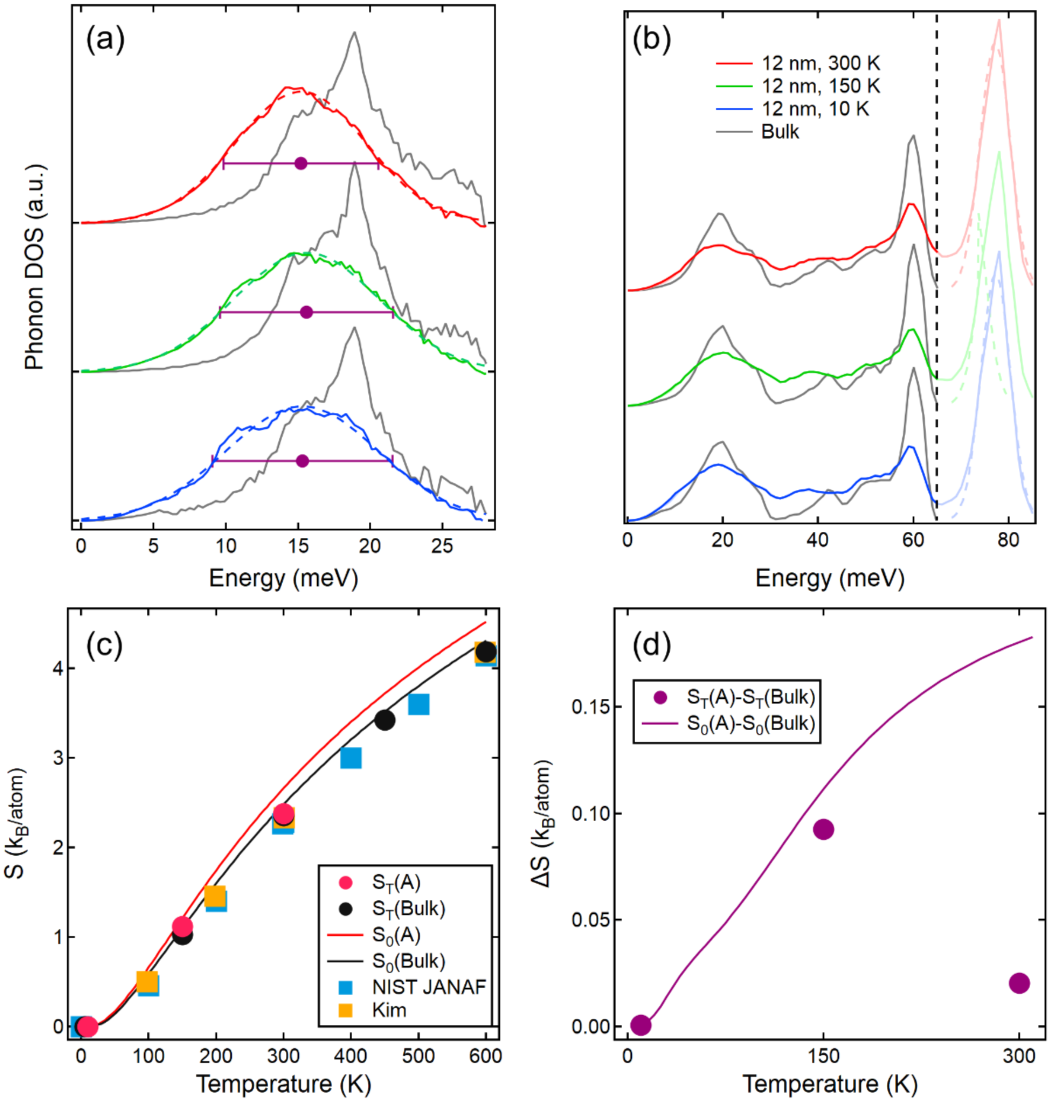

Figure 3.3 (a) Phonon DOS of Sample A measured with E_i = 30 meV evolves toward that of crystalline silicon as temperature increases. The orange dots with error bar show the center and the FWHM of the Gaussian fits to the DOS of Sample A. (b) Phonon DOS of Sample A measured with E_i = 90 meV (solid lines). The hydrogen-related phonon peaks at 78 meV were fitted with Gaussian functions (dim-colored dash lines) and subtracted. Phonon DOSs were normalized to unity between 0 and 65 meV indicated by the black dash line. (c) Vibrational entropy-per-atom extracted from as-measured phonon DOSs of Sample A and bulk silicon (round markers). Without considering the temperature effect on phonon DOS, vibrational entropy-per-atom calculated from the phonon DOSs of Sample A and bulk silicon measured at the low temperature with different thermal occupations (solid lines). Square markers show reference data. (d) The difference in vibrational entropy-per-atom between Sample A and the bulk sample is largest at intermediate temperature. The round markers/solid line show differences between the red and black markers/solid lines in (c)

We found TA phonon profiles of silicon nanocrystals evolve toward that of bulk silicon with increasing temperature, while optical phonon profiles do not show strong temperature dependence, as shown in Figure 3.3(a, b). In specific, the energy of the low-energy TA phonon of 12-nm silicon nanocrystals (Sample A) increases while the FWHM of the Gaussian fit to the TA phonon DOS decreases by 15% as temperature increases from 10 to 300 K.

The group velocity of the low-energy TA phonon in silicon nanocrystals was compared to that of bulk silicon assuming Sample A's TA phonon modes can be described by the Debye Model, which has been widely used in previous studies.[71–73] The Debye Model describes a linear phonon dispersion which corresponds to a quadratic relation between phonon DOS and phonon energy. We fit the measured phonon DOSs with

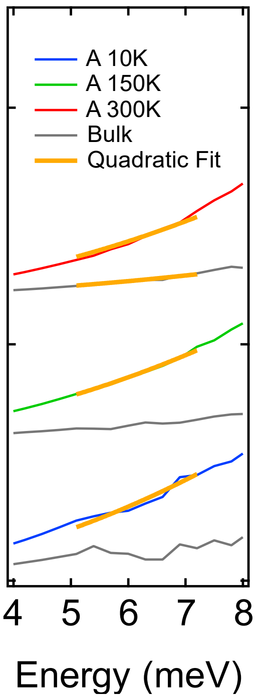

Figure 3.4 Quadric fits to the INS measured phonon DOS with $E_i = 30$ meV.

quadratic equations, as shown in Figure 3.4, and extracted phonon group velocities from the quadratic terms using:

$$D(E) = \frac{3VE^2}{2\pi^2\hbar^3 v_g^3} \tag{3.3}$$

where E, $D(E)$, V, $\hbar$, and v_g are phonon energy, phonon DOS, system volume, reduced Planck's constant, and phonon group velocity, respectively. The fitting range was set from 5.1 meV to 7.2 meV, because the data points below 5 meV, where the elastic cutoff is, are not from the experiment, while the experimental data beyond 7.2 meV cannot be well described by the Debye Model, see the first-principles calculated acoustic phonon dispersion in Γ-L direction of crystalline silicon in Figure 3.2(a). The extracted group velocity of the low-energy acoustic phonon of Sample A is 34 ± 1% smaller than that of the bulk silicon at 300 K. Additionally, the extracted group velocity of the low-energy acoustic phonon of Sample A increases 10 ± 1% as temperature increases from 10 to 300 K. We attribute temperature-induced TA phonon evolutions of silicon nanocrystals to the strong temperature effect on the TA phonon of the shell regions of silicon nanocrystals, while the temperature effect on the TA phonon of the core regions of silicon nanocrystals resembles that of crystalline silicon which is reported to be small.[74] The uncertainties come from fitting errors.

To quantitively describe the temperature effect on phonon dynamics, we calculated vibrational entropies of 12-nm unoxidized samples (Sample A) and bulk silicon using as-measured phonon DOSs (below 65 meV, Figure 3.3(b)) at different temperatures. The vibrational entropy-per-atom was calculated using Equation 3.4 with harmonic approximation:

$$S_{vib}(T) = 3k_B \int_0^{Em} [(n+1)\ln(n+1) - n\ln(n)]\, D(E)\, dE \qquad (3.4)$$

where k_B, E_m, n, and $D(E)$ are Boltzmann constant, the maximum phonon energy, the Bose-Einstein distribution function, and phonon DOS, respectively.[74,75] To illustrate the temperature effect on phonon DOSs, we compared vibrational entropies extracted from as-measured phonon DOSs to those obtained without considering the temperature effect on phonon DOSs. The later ones were calculated from phonon DOSs measured at low temperatures with different thermal occupations and plotted in Figure 3.3(c). The calculated $S_{vib,Bulk(as-mesured)}$ agrees with reported values.[74] The small differences between $S_{vib,Bulk(as-mesured)}$ and $S_{vib,Bulk(low-T)}$ shows weak temperature effect on phonon dynamics of bulk silicon. In contrast, the big difference between $S_{vib,A(as-mesured)}$ and $S_{vib,A(low-T)}$ at elevated temperature shows strong temperature effect on phonon dynamics of silicon nanocrystals.

Surprisingly, unlike the entropy difference between 12-nm unoxidized samples (Sample A) and bulk silicon calculated from the phonon DOSs measured at low temperature, the entropy difference calculated using as-measured phonon DOSs is not monotonous to temperature, as shown in Figure 3. (d). The $\Delta S_{vib(as-mesured)}$ is small at low temperatures due to low thermal occupation. The $\Delta S_{vib(as-mesured)}$ is also small at elevated temperatures (300 K) because the difference between TA phonon profiles of Sample A and bulk silicon diminishes, as shown in Figure 3. (a). The $\Delta S_{vib(as-mesured)}$ is the largest at intermediate temperature (150 K) because both thermal occupation and the difference between the phonon profiles of Sample A and bulk silicon are relatively large.

3.7 Conclusion

We conducted systematic experiments to study particle size, oxidation, and temperature effects on phonon dynamics in spatially confined silicon systems. We showed particle size, oxidation level, and temperature have comparable effects on the lattice vibrations of silicon nanocrystals. We observed strong acoustic phonon responses to temperature suggesting modulations of phonon group velocity. Such modulations lead to large differences between vibrational entropies of silicon nanocrystals and bulk silicon at intermediate temperatures. The great differences between phonon responses to temperature changes also illustrate that the lattice vibrations of large silicon nanocrystals (12 nm) and bulk silicon are substantially different.

We showed TA phonon modes and optical phonon modes of silicon nanocrystals have distinct responses to changes in particle size, oxidation level, and temperature. Specifically, these changes have much stronger effects on TA than optical phonon modes.

We showed that one can practically use these effects to manipulate the TA phonon dynamics of silicon nanocrystals. In contrast, we showed changes in particle size, oxidation level, and temperature have much weaker effects on optical phonon modes, which may have stronger interaction with electrons and attribute to the PL of silicon nanocrystals.[76] However, the newly formed high-energy phonon modes due to oxidation or surface functionalization, such as that at 110 meV in Sample C, may play important roles in the PL process.[77] This work provides valuable information on phonon dynamics which may greatly impact the PL of silicon nanocrystals by facilitating the possible Γ-X recombination. A deeper understanding of the mechanism of PL of silicon nanocrystals requires further theoretical investigations on the electron-phonon interaction of spatially confined silicon systems and will benefit from this work.

3.8 Reference

(1) Li, Q.; Luo, T.-Y.; Zhou, M.; Abroshan, H.; Huang, J.; Kim, H. J.; Rosi, N. L.; Shao, Z.; Jin, R. Silicon Nanoparticles with Surface Nitrogen: 90% Quantum Yield with Narrow Luminescence Bandwidth and the Ligand Structure Based Energy Law. *ACS Nano* **2016**, *10* (9), 8385–8393.

(2) Jurbergs, D.; Rogojina, E.; Mangolini, L.; Kortshagen, U. Silicon Nanocrystals with Ensemble Quantum Yields Exceeding 60%. *Appl. Phys. Lett.* **2006**, *88* (23), 233116.

(3) Miller, J. B.; Van Sickle, A. R.; Anthony, R. J.; Kroll, D. M.; Kortshagen, U. R.; Hobbie, E. K. Ensemble Brightening and Enhanced Quantum Yield in Size-Purified Silicon Nanocrystals. *ACS Nano* **2012**, *6* (8), 7389–7396.

(4) Mastronardi, M. L.; Maier-Flaig, F.; Faulkner, D.; Henderson, E. J.; Kübel, C.; Lemmer, U.; Ozin, G. A. Size-Dependent Absolute Quantum Yields for Size-Separated Colloidally-Stable Silicon Nanocrystals. *Nano Lett.* **2012**, *12* (1), 337–342.

(5) Gelloz, B.; Juangsa, F. B.; Nozaki, T.; Asaka, K.; Koshida, N.; Jin, L. Si/SiO2 Core/Shell Luminescent Silicon Nanocrystals and Porous Silicon Powders With High Quantum Yield, Long Lifetime, and Good Stability. *Frontiers in Physics*. 2019, p 47.

(6) Ranjbar-Navazi, Z.; Omidi, Y.; Eskandani, M.; Davaran, S. Cadmium-Free Quantum Dot-Based Theranostics. *TrAC Trends Anal. Chem.* **2019**, *118*, 386–400.

(7) Alsharif, N. H.; Berger, C. E. M.; Varanasi, S. S.; Chao, Y.; Horrocks, B. R.; Datta, H. K. Alkyl-Capped Silicon Nanocrystals Lack Cytotoxicity and Have Enhanced Intracellular Accumulation in Malignant Cells via Cholesterol-Dependent Endocytosis. *Small* **2009**, *5* (2), 221–228.

(8) Bhattacharjee, S.; Rietjens, I. M. C. M.; Singh, M. P.; Atkins, T. M.; Purkait, T. K.; Xu, Z.; Regli, S.; Shukaliak, A.; Clark, R. J.; Mitchell, B. S.; Alink, G. M.; Marcelis, A. T. M.; Fink, M. J.; Veinot, J. G. C.; Kauzlarich, S. M.; Zuilhof, H. Cytotoxicity of Surface-Functionalized Silicon and Germanium Nanoparticles: The Dominant Role of Surface Charges. *Nanoscale* **2013**, *5* (11), 4870–4883.

(9) Erogbogbo, F.; Yong, K.-T.; Roy, I.; Hu, R.; Law, W.-C.; Zhao, W.; Ding, H.; Wu, F.; Kumar, R.; Swihart, M. T.; Prasad, P. N. In Vivo Targeted Cancer Imaging, Sentinel Lymph Node Mapping and Multi-Channel Imaging with Biocompatible Silicon Nanocrystals. *ACS Nano* **2011**, *5* (1), 413–423.

(10) Liu, J.; Erogbogbo, F.; Yong, K.-T.; Ye, L.; Liu, J.; Hu, R.; Chen, H.; Hu, Y.; Yang, Y.; Yang, J.; Roy, I.; Karker, N. A.; Swihart, M. T.; Prasad, P. N. Assessing Clinical Prospects of Silicon Quantum Dots: Studies in Mice and Monkeys. *ACS Nano* **2013**, *7* (8), 7303–7310.

(11) Park, J. H.; Gu, L.; Von Maltzahn, G.; Ruoslahti, E.; Bhatia, S. N.; Sailor, M. J. Biodegradable Luminescent Porous Silicon Nanoparticles for in Vivo Applications. *Nat. Mater.* **2009**, *8* (4), 331–336.

(12) Warner, J. H.; Hoshino, A.; Yamamoto, K.; Tilley, R. D. Water-Soluble Photoluminescent Silicon Quantum Dots. *Angew. Chemie Int. Ed.* **2005**, *44* (29), 4550–4554.

(13) Shiohara, A.; Prabakar, S.; Faramus, A.; Hsu, C.-Y.; Lai, P.-S.; Northcote, P. T.; Tilley, R. D. Sized Controlled Synthesis, Purification, and Cell Studies with Silicon Quantum Dots. *Nanoscale* **2011**, *3* (8), 3364–3370.

(14) Morozova, S.; Alikina, M.; Vinogradov, A.; Pagliaro, M. Silicon Quantum Dots: Synthesis, Encapsulation, and Application in Light-Emitting Diodes. *Frontiers in Chemistry*. 2020, p 191.

(15) Xu, K. Silicon MOS Optoelectronic Micro-Nano Structure Based on Reverse-Biased PN Junction. *Phys. status solidi* **2019**, *216* (7), 1800868.

(16) Oh, J.; Yuan, H.-C.; Branz, H. M. An 18.2%-Efficient Black-Silicon Solar Cell Achieved through Control of Carrier Recombination in Nanostructures. *Nat. Nanotechnol.* **2012**, *7* (11), 743–748.

(17) Biswas, R.; Xu, C. Nano-Crystalline Silicon Solar Cell Architecture with Absorption at the Classical 4n2 Limit. *Opt. Express* **2011**, *19* (S4), A664–A672.

(18) Dimitrov, D. Z.; Du, C.-H. Crystalline Silicon Solar Cells with Micro/Nano Texture. *Appl. Surf. Sci.* **2013**, *266*, 1–4.

(19) Nayak, B. K.; Iyengar, V. V; Gupta, M. C. Efficient Light Trapping in Silicon Solar Cells by Ultrafast-Laser-Induced Self-Assembled Micro/Nano Structures. *Prog. Photovoltaics Res. Appl.* **2011**, *19* (6), 631–639.

(20) Talapin, D. V; Lee, J.-S.; Kovalenko, M. V; Shevchenko, E. V. Prospects of Colloidal Nanocrystals for Electronic and Optoelectronic Applications. *Chem. Rev.* **2010**, *110* (1), 389–458.

(21) Kovalenko, M. V; Manna, L.; Cabot, A.; Hens, Z.; Talapin, D. V; Kagan, C. R.; Klimov, V. I.; Rogach, A. L.; Reiss, P.; Milliron, D. J.; Guyot-Sionnnest, P.;

Konstantatos, G.; Parak, W. J.; Hyeon, T.; Korgel, B. A.; Murray, C. B.; Heiss, W. Prospects of Nanoscience with Nanocrystals. *ACS Nano* **2015**, *9* (2), 1012–1057.

(22) Priolo, F.; Gregorkiewicz, T.; Galli, M.; Krauss, T. F. Silicon Nanostructures for Photonics and Photovoltaics. *Nat. Nanotechnol.* **2014**, *9* (1), 19–32.

(23) Nayfeh, M. H.; Rao, S.; Barry, N.; Therrien, J.; Belomoin, G.; Smith, A.; Chaieb, S. Observation of Laser Oscillation in Aggregates of Ultrasmall Silicon Nanoparticles. *Appl. Phys. Lett.* **2002**, *80* (1), 121–123.

(24) Rosso-Vasic, M.; Spruijt, E.; Popović, Z.; Overgaag, K.; van Lagen, B.; Grandidier, B.; Vanmaekelbergh, D.; Domínguez-Gutiérrez, D.; De Cola, L.; Zuilhof, H. Amine-Terminated Silicon Nanoparticles: Synthesis, Optical Properties and Their Use in Bioimaging. *J. Mater. Chem.* **2009**, *19* (33), 5926–5933.

(25) Wu, S.; Zhong, Y.; Zhou, Y.; Song, B.; Chu, B.; Ji, X.; Wu, Y.; Su, Y.; He, Y. Biomimetic Preparation and Dual-Color Bioimaging of Fluorescent Silicon Nanoparticles. *J. Am. Chem. Soc.* **2015**, *137* (46), 14726–14732.

(26) Hessel, C. M.; Rasch, M. R.; Hueso, J. L.; Goodfellow, B. W.; Akhavan, V. A.; Puvanakrishnan, P.; Tunnel, J. W.; Korgel, B. A. Alkyl Passivation and Amphiphilic Polymer Coating of Silicon Nanocrystals for Diagnostic Imaging. *Small* **2010**, *6* (18), 2026–2034.

(27) Wilcoxon, J. P.; Samara, G. A.; Provencio, P. N. Optical and Electronic Properties of Si Nanoclusters Synthesized in Inverse Micelles. *Phys. Rev. B* **1999**, *60* (4), 2704–2714.

(28) Valenta, J.; Fucikova, A.; Pelant, I.; Kůsová, K.; Dohnalová, K.; Aleknavičius, A.; Cibulka, O.; Fojtík, A.; Kada, G. On the Origin of the Fast Photoluminescence Band in Small Silicon Nanoparticles. *New J. Phys.* **2008**, *10* (7), 73022.

(29) Zhou, Z.; Brus, L.; Friesner, R. Electronic Structure and Luminescence of 1.1- and 1.4-Nm Silicon Nanocrystals: Oxide Shell versus Hydrogen Passivation. *Nano Lett.* **2003**, *3* (2), 163–167.

(30) Rosso-Vasic, M.; Spruijt, E.; van Lagen, B.; De Cola, L.; Zuilhof, H. Alkyl-Functionalized Oxide-Free Silicon Nanoparticles: Synthesis and Optical Properties. *Small* **2008**, *4* (10), 1835–1841.

(31) Wen, X.; Zhang, P.; Smith, T. A.; Anthony, R. J.; Kortshagen, U. R.; Yu, P.; Feng, Y.; Shrestha, S.; Coniber, G.; Huang, S. Tunability Limit of Photoluminescence in Colloidal Silicon Nanocrystals. *Sci. Rep.* **2015**, *5* (1), 12469.

(32) Kovalev, D.; Heckler, H.; Ben-Chorin, M.; Polisski, G.; Schwartzkopff, M.; Koch, F. Breakdown of the K-Conservation Rule in Si Nanocrystals. *Phys. Rev. Lett.* **1998**, *81* (13), 2803–2806.

(33) Kůsová, K.; Cibulka, O.; Dohnalová, K.; Pelant, I.; Valenta, J.; Fučíková, A.; Žídek, K.; Lang, J.; Englich, J.; Matějka, P.; Štěpánek, P.; Bakardjieva, S. Brightly Luminescent Organically Capped Silicon Nanocrystals Fabricated at Room Temperature and Atmospheric Pressure. *ACS Nano* **2010**, *4* (8), 4495–4504.

(34) English, D. S.; Pell, L. E.; Yu, Z.; Barbara, P. F.; Korgel, B. A. Size Tunable Visible Luminescence from Individual Organic Monolayer Stabilized Silicon Nanocrystal Quantum Dots. *Nano Lett.* **2002**, *2* (7), 681–685.

(35) Zou, J.; Baldwin, R. K.; Pettigrew, K. A.; Kauzlarich, S. M. Solution Synthesis of Ultrastable Luminescent Siloxane-Coated Silicon Nanoparticles. *Nano Lett.* **2004**, *4* (7), 1181–1186.

(36) Yang, Z.; De los Reyes, G. B.; Titova, L. V; Sychugov, I.; Dasog, M.; Linnros, J.; Hegmann, F. A.; Veinot, J. G. C. Evolution of the Ultrafast Photoluminescence of Colloidal Silicon Nanocrystals with Changing Surface Chemistry. *ACS Photonics* **2015**, *2* (5), 595–605.

(37) Li, Z.; Kortshagen, U. R. Aerosol-Phase Synthesis and Processing of Luminescent Silicon Nanocrystals. *Chem. Mater.* **2019**, *31* (20), 8451–8458.

(38) Dasog, M.; Yang, Z.; Regli, S.; Atkins, T. M.; Faramus, A.; Singh, M. P.; Muthuswamy, E.; Kauzlarich, S. M.; Tilley, R. D.; Veinot, J. G. C. Chemical Insight into the Origin of Red and Blue Photoluminescence Arising from Freestanding Silicon Nanocrystals. *ACS Nano* **2013**, *7* (3), 2676–2685.

(39) Garcia, C.; Garrido, B.; Pellegrino, P.; Ferre, R.; Moreno, J. A.; Morante, J. R.; Pavesi, L.; Cazzanelli, M. Size Dependence of Lifetime and Absorption Cross Section of Si Nanocrystals Embedded in SiO2. *Appl. Phys. Lett.* **2003**, *82* (10), 1595–1597.

(40) Sangghaleh, F.; Bruhn, B.; Schmidt, T.; Linnros, J. Exciton Lifetime Measurements on Single Silicon Quantum Dots. *Nanotechnology* **2013**, *24* (22), 225204.

(41) Brown, S. L.; Vogel, D. J.; Miller, J. B.; Inerbaev, T. M.; Anthony, R. J.; Kortshagen, U. R.; Kilin, D. S.; Hobbie, E. K. Enhancing Silicon Nanocrystal Photoluminescence through Temperature and Microstructure. *J. Phys. Chem. C* **2016**, *120* (33), 18909–18916.

(42) Wolkin, M. V; Jorne, J.; Fauchet, P. M.; Allan, G.; Delerue, C. Electronic States and Luminescence in Porous Silicon Quantum Dots: The Role of Oxygen. *Phys. Rev. Lett.* **1999**, *82* (1), 197–200.

(43) Brus, L. E.; Szajowski, P. F.; Wilson, W. L.; Harris, T. D.; Schuppler, S.; Citrin, P. H. Electronic Spectroscopy and Photophysics of Si Nanocrystals: Relationship to Bulk c-Si and Porous Si. *J. Am. Chem. Soc.* **1995**, *117* (10), 2915–2922.

(44) Calcott, P. D. J.; Nash, K. J.; Canham, L. T.; Kane, M. J.; Brumhead, D. Identification of Radiative Transitions in Highly Porous Silicon. *J. Phys. Condens. Matter* **1993**, *5* (7), L91–L98.

(45) Suemoto, T.; Tanaka, K.; Nakajima, A.; Itakura, T. Observation of Phonon Structures in Porous Si Luminescence. *Phys. Rev. Lett.* **1993**, *70* (23), 3659–3662.

(46) Ghosh, B.; Shirahata, N. Influence of Oxidation on Temperature-Dependent Photoluminescence Properties of Hydrogen-Terminated Silicon Nanocrystals. *Crystals*. 2020.

(47) Sagar, D. M.; Atkin, J. M.; Palomaki, P. K. B.; Neale, N. R.; Blackburn, J. L.; Johnson, J. C.; Nozik, A. J.; Raschke, M. B.; Beard, M. C. Quantum Confined Electron–Phonon Interaction in Silicon Nanocrystals. *Nano Lett.* **2015**, *15* (3), 1511–1516.

(48) Delerue, C.; Allan, G.; Lannoo, M. Electron-Phonon Coupling and Optical Transitions for Indirect-Gap Semiconductor Nanocrystals. *Phys. Rev. B* **2001**, *64* (19), 193402.

(49) Lopez, T.; Mangolini, L. On the Nucleation and Crystallization of Nanoparticles in Continuous-Flow Nonthermal Plasma Reactors. *J. Vac. Sci. Technol. B* **2014**, *32* (6), 61802.

(50) Mangolini, L.; Thimsen, E.; Kortshagen, U. High-Yield Plasma Synthesis of Luminescent Silicon Nanocrystals. *Nano Lett.* **2005**, *5* (4), 655–659.

(51) Chen, S.; Coleman, D.; Abernathy, D. L.; Banerjee, A.; Daemen, L. L.; Mangolini, L.; Li, C. W. Giant Low-Temperature Anharmonicity in Silicon Nanocrystals. *Phys. Rev. Mater.* **2020**, *4* (5), 56001.

(52) Lin, J. Y. Y.; Banerjee, A.; Islam, F.; Le, M. D.; Abernathy, D. L. Energy Dependence of the Flux and Elastic Resolution for the ARCS Neutron Spectrometer. *Phys. B Condens. Matter* **2019**, *562*, 26–30.

(53) Taylor, J.; Arnold, O.; Bilheaux, J.; Buts, A.; Campbell, S.; Doucet, M.; Draper, N.;

Fowler, R.; Gigg, M.; Lynch, V.; Markvardsen, A.; Palmen, K.; Parker, P.; Peterson, P.; Ren, S.; Reuter, M.; Savici, A.; Taylor, R.; Tolchenov, R.; Whitley, R.; Zhou, W, J. *Mantid, A High Performance Framework for Reduction and Analysis of Neutron Scattering Data*; 2012.

(54) Kresch, M.; Delaire, O.; Stevens, R.; Lin, J. Y. Y.; Fultz, B. Neutron Scattering Measurements of Phonons in Nickel at Elevated Temperatures. *Phys. Rev. B* **2007**, *75* (10), 104301.

(55) Lucas, M. S.; Kresch, M.; Stevens, R.; Fultz, B. Phonon Partial Densities of States and Entropies of Fe and Cr in Bcc Fe-Cr from Inelastic Neutron Scattering. *Phys. Rev. B* **2008**, *77* (18), 184303.

(56) Delaire, O.; Kresch, M.; Muñoz, J. A.; Lucas, M. S.; Lin, J. Y. Y.; Fultz, B. Electron-Phonon Interactions and High-Temperature Thermodynamics of Vanadium and Its Alloys. *Phys. Rev. B* **2008**, *77* (21), 214112.

(57) Plimpton, S. Fast Parallel Algorithms for Short-Range Molecular Dynamics. *J. Comput. Phys.* **1995**, *117* (1), 1–19.

(58) Tersoff, J. Empirical Interatomic Potential for Silicon with Improved Elastic Properties. *Phys. Rev. B* **1988**, *38* (14), 9902–9905.

(59) Munetoh, S.; Motooka, T.; Moriguchi, K.; Shintani, A. Interatomic Potential for Si–O Systems Using Tersoff Parameterization. *Comput. Mater. Sci.* **2007**, *39* (2), 334–339.

(60) Kresse, G.; Furthmüller, J. Efficiency of Ab-Initio Total Energy Calculations for Metals and Semiconductors Using a Plane-Wave Basis Set. *Comput. Mater. Sci.* **1996**, *6* (1), 15–50.

(61) Togo, A.; Tanaka, I. First Principles Phonon Calculations in Materials Science. *Scr. Mater.* **2015**, *108*, 1–5.

(62) Harten, U.; Toennies, J. P.; Wöll, C.; Miglio, L.; Ruggerone, P.; Colombo, L.; Benedek, G. Surface Phonons in Si(111)+ H(1 X 1). *Phys. Rev. B* **1988**, *38* (5), 3305–3310.

(63) Nilsson, G.; Nelin, G. Study of the Homology between Silicon and Germanium by Thermal-Neutron Spectrometry. *Phys. Rev. B* **1972**, *6* (10), 3777–3786.

(64) Wei, S.; Chou, M. Y. Phonon Dispersions of Silicon and Germanium from First-Principles Calculations. *Phys. Rev. B* **1994**, *50* (4), 2221–2226.

(65) Holt, M.; Wu, Z.; Hong, H.; Zschack, P.; Jemian, P.; Tischler, J.; Chen, H.; Chiang, T.-C. Determination of Phonon Dispersions from X-Ray Transmission Scattering: The Example of Silicon. *Phys. Rev. Lett.* **1999**, *83* (16), 3317–3319.

(66) Prechtel, J.; Kalus, J.; Lüscher, E.; Pintschovius, L.; Ghosh, R. Measurement of Mode Grüneisen Parameters in Si. *Phys. status solidi* **1979**, *93* (2), 653–659.

(67) Weinstein, B. A.; Piermarini, G. J. Raman Scattering and Phonon Dispersion in Si and GaP at Very High Pressure. *Phys. Rev. B* **1975**, *12* (4), 1172–1186.

(68) Rignanese, G.-M.; Michenaud, J.-P.; Gonze, X. Ab Initio Study of the Volume Dependence of Dynamical and Thermodynamical Properties of Silicon. *Phys. Rev. B* **1996**, *53* (8), 4488–4497.

(69) Többens, D. M.; Stüßer, N.; Knorr, K.; Mayer, H. M.; Lampert, G. E9: The New High-Resolution Neutron Powder Diffractometer at the Berlin Neutron Scattering Center. In *European Powder Diffraction EPDIC 7*; Materials Science Forum; Trans Tech Publications Ltd, 2001; Vol. 378, pp 288–293.

(70) Tsu, D. V; Lucovsky, G.; Davidson, B. N. Effects of the Nearest Neighbors and the Alloy Matrix on SiH Stretching Vibrations in the Amorphous SiO_r :H (0<r<2) Alloy System. *Phys. Rev. B* **1989**, *40* (3), 1795–1805.

(71) Ho-Kwang, M.; Junshan, X.; Viktor, S.; Jinfu, S.; Russell, H.; Wolfgang, S.; Michael, H.; Esen, A.; Lidunka, V.; Dario, A.; Geoffrey, P.; Michael, G.; Mathis, S.-B.; D., H.; P., E.; G., S.; Heiner, G.; R., L.; G., W. Phonon Density of States of Iron up to 153 Gigapascals. Science. 2001, 292 (5518), 914–916.

(72) Ramazani, A.; Reihani, A.; Soleimani, A.; Larson, R.; Sundararaghavan, V. Molecular Dynamics Study of Phonon Transport in Graphyne Nanotubes. *Carbon N. Y.* **2017**, *123*, 635–644.

(73) Jeong, C.; Datta, S.; Lundstrom, M. Full Dispersion versus Debye Model Evaluation of Lattice Thermal Conductivity with a Landauer Approach. *J. Appl. Phys.* **2011**, *109* (7), 73718.

(74) Kim, D. S.; Smith, H. L.; Niedziela, J. L.; Li, C. W.; Abernathy, D. L.; Fultz, B. Phonon Anharmonicity in Silicon from 100 to 1500 K. *Phys. Rev. B* **2015**, *91* (1), 14307.

(75) Fultz, B. Vibrational Thermodynamics of Materials. *Prog. Mater. Sci.* **2010**, *55* (4), 247–352.

(76) Monserrat, B.; Needs, R. J. Comparing Electron-Phonon Coupling Strength in Diamond, Silicon, and Silicon Carbide: First-Principles Study. *Phys. Rev. B* **2014**, *89* (21), 214304.

(77) Borczyskowski, J. M. C. H. von. Electron − Phonon Coupling and Localization of Excitons in Single Silicon Nanocrystals. *Nano Lett.* **2008**, *8* (2), 656–660.

Chapter 4

Hydrogen-Dominated Phonon Dynamics in Surface Functionalized Silicon Nanocrystals

4.1 Abstract

Photoluminescent silicon nanocrystals have been attractive thanks to their great potential in optoelectronic and biomedical applications. Previous studies observed a significant increase in fluorescence quantum yield induced by surface functionalization of silicon nanocrystals, however, the mechanism of which is still under debate. Because phonon dynamics in spatially confined silicon systems are believed to play an important role in the photoluminescent process, we measured the phonon density of states of the hydrogen-terminated and the 1-dodecene terminated 3-nm spherical silicon nanocrystals to investigate the effect of organic surface ligands on the phonon dynamics in silicon nanocrystals. We found that the phonon density of states of the 1-dodecene terminated 3-nm spherical silicon nanocrystals are largely different from those of their hydrogen-terminated counterparts. Additionally, we observed small temperature effects on the phonon dynamics of 1-dodecene terminated silicon nanocrystals due to the dominant neutron scattering cross section of hydrogen atoms. A small effect from the heat treatment on the phonon dynamics of 1-dodecene terminated silicon nanocrystals was also observed. This work sheds light on the phonon dynamics in surface functionalized silicon nano systems and will contribute to the further investigation of the origin of the photoluminescence in spatially confined silicon systems.

4.2 Introduction

Silicon nanocrystals have immense industrial, biotechnological, agriculture, and pharmaceutical applications as non-toxic, bio-compatible, and bio-degradable agents thanks to their high surface area to volume ratio, versatile functionalization, and many other mesmerizing properties.[1–10] Recently, spatially confined silicon systems have drawn an increasing amount of attention with the observation of their photoluminescent properties and their great potential in optoelectronic applications.[11–16] Previous studies show both electrons and phonons contribute to the photoluminescence of quantum-sized silicon systems and many models have been proposed, however, the mechanism of the photoluminescence remains unclear.[17–22]

The extensive studies on surface-functionalized silicon nanocrystals show surface functionalization can play an important role and modify the photoluminescence behaviors of silicon nanocrystals in many aspects.[23–26] Samuel reported changes in microstructure associated with the thermotropic crystallization of a matrix comprised of unbound ligands can increase the effective excitation fluence through scattering, yielding dramatic improvements in photoluminescence intensity.[27] Sinelnikov suggested alkanes functionalizations do not interfere with the intrinsic core emission of silicon nanocrystals while oxide moieties do affect the recombination pathways in silicon nanocrystals.

In this chapter, phonon density of state (DOS) of the 1-dodecene terminated and the hydrogen-terminated 3-nm spherical silicon nanocrystals were measured by inelastic neutron scattering (INS) under different temperatures to investigate the effect of surface functionalization on the phonon dynamics in silicon nanocrystals. The effect of heat treatment on phonon dynamics was also studied. This work will provide valuable information on the investigation of the origin of photoluminescence in spatially confined silicon systems.

4.3 Materials and methods

The 1-dodecene terminated and the hydrogen-terminated 3-nm spherical silicon nanocrystals were synthesized by a non-thermal plasma process[28–30] using a 60 W radio frequency capacitive plasma at 1 Torr reactor pressure with 130 sccm of a 1.37% SiH_4:Ar mixture. Upon leaving the powered plasma region 87.5 sccm of pure H_2, and 12.5 sccm of H_2 saturated with 1-dodecene was added which cooled the plasma while simultaneously using the plasma energy to functionalize the silicon nanocrystals with dodecene. The nanomaterials were collected on stainless steel 400-grade mesh, then transferred into a glovebox via an air-free transfer chamber. In the glovebox, the nanocrystals were removed from the mesh and placed in the center of a 1” quartz tube with quarter turn vacuum seals on each end. A sealed tube of 1-dodecene terminated silicon nanocrystals was then brought out of the glovebox, brought to vacuum conditions, and heated to 200 ºC for 1 hour before being refilled with argon, closing the valves on both ends and being transferred back into the glovebox where it was packed up to go to Oak Ridge National Laboratory (ORNL).

INS measurements were performed on the Wide Angular-Range Chopper Spectrometer (ARCS), a direct geometry chopper neutron spectrometer at ORNL. All the samples were loaded in a 3/8-inch diameter aluminum can. ARCS has an energy resolution of 4% or better of the neutron incident energy (E_i).[31] Neutron beams with E_i of 30, 75, 150, and 500 meV were chosen to optimize the energy resolution and range. The samples were measured at 15, 150, 300, 450, 600 K, and then again at 300 K to check the hysteresis behaviors.

4.4 Data processing

Mantid software[32] was used for data processing. The event mode data of ARCS measurement contains information about the detector number and the time-of-arrival of each scattered neutron. The momentum (q) and energy (E) transfer of each neutron was calculated from its time-of-flight and scattering geometry, with the knowledge of the distance between detectors and the sample to generate the scattering intensity S(q, E). Backgrounds from an empty can were subtracted from the signal. The phonon spectra were analyzed within the incoherent approximation, which has been shown to work reliably.[33–35] Elastic intensities were removed below 4, 4, 7, and 7 meV for E_i = 30, 75, 150, and 500 meV, respectively. The low energy part of the phonon DOS of the silicon nanocrystals was extrapolated by power functions, while the low energy part of the phonon DOS of bulk silicon was extrapolated by the Debye model, as described in the Discussion Section. The energy bin sizes were set at 0.5, 1, 1.5, and 5 meV for 30, 75, 150, and 500 meV, respectively. Due to the small effective sample thickness, no multiple scattering correction was necessary. Multi-phonon scattering correction was performed by an iterative method considering the S(q, E) and the multi-phonon expansion.[33] The phonon spectra were also corrected for the thermal occupation.

4.5 Result and discussion

Phonon DOSs in the untreated 1-dodecene terminated and the heat treated 1-dodecene terminated 3-nm spherical silicon nanocrystals are similar to each other and significantly different from those of their hydrogen terminated counterparts from low energy end up to 500 meV, as shown in Figure 4.1. In specific, the phonon profiles below 30 meV of the 1-dodecane-terminated silicon nanocrystals are about 20% broader than those of the hydrogen-terminated nanocrystals, as shown in Figure 4.1(a). Such discrepancies majorly come from the phonon modes in the 1-dodecene ligand and the near-surface interface region. Another example is that the pronounced phonon peak at 350 meV in Figure 4.1(d) was reported to be related to CH_3 stretching and CH_2 stretching modes.[36]

The temperature effect on phonon DOSs in the untreated 1-dodecene terminated and the heat treated 1-dodecene terminated 3-nm spherical silicon nanocrystals are small, as shown in Figure 4.2. The temperature-induced phonon evolutions at 90 (SiH2 scissoring mode), 110 (S-C stretching mode), and 350 meV are expected. This is because atoms tend to have larger vibrational amplitudes which will induce more phonon anharmonicity and result in shorter phonon lifetimes at elevated temperatures. Phonon lifetime is inversely proportional to the linewidth of a phonon DOS profile so the phonon peaks at 90, 110, and 350 meV become broader with increasing temperature. The transverse acoustic (TA)[37–39] phonon profile in the hydrogen-terminated 3-nm spherical silicon nanocrystals becomes narrower and shifted to higher energy at elevated temperature due to thermal relaxations, as shown in Figure 4.2(a). This agrees with our observations from the larger-particle-sized hydrogen-terminated silicon nanocrystals.[40,41] In addition, the phonon energy at 260 meV, which is related to SiH_x stretching modes, in all our samples decreases as temperature increases. Such phonon behaviors suggest that heating removes the weakly bonded hypervalent SiH_3 species which have slightly higher phonon energy than $SiH_{x=1,2}$ and act as nonradiative recombination centers. This explains the enhanced photoluminescence quantum yield at elevated temperatures which are reported in the previous study.[42]

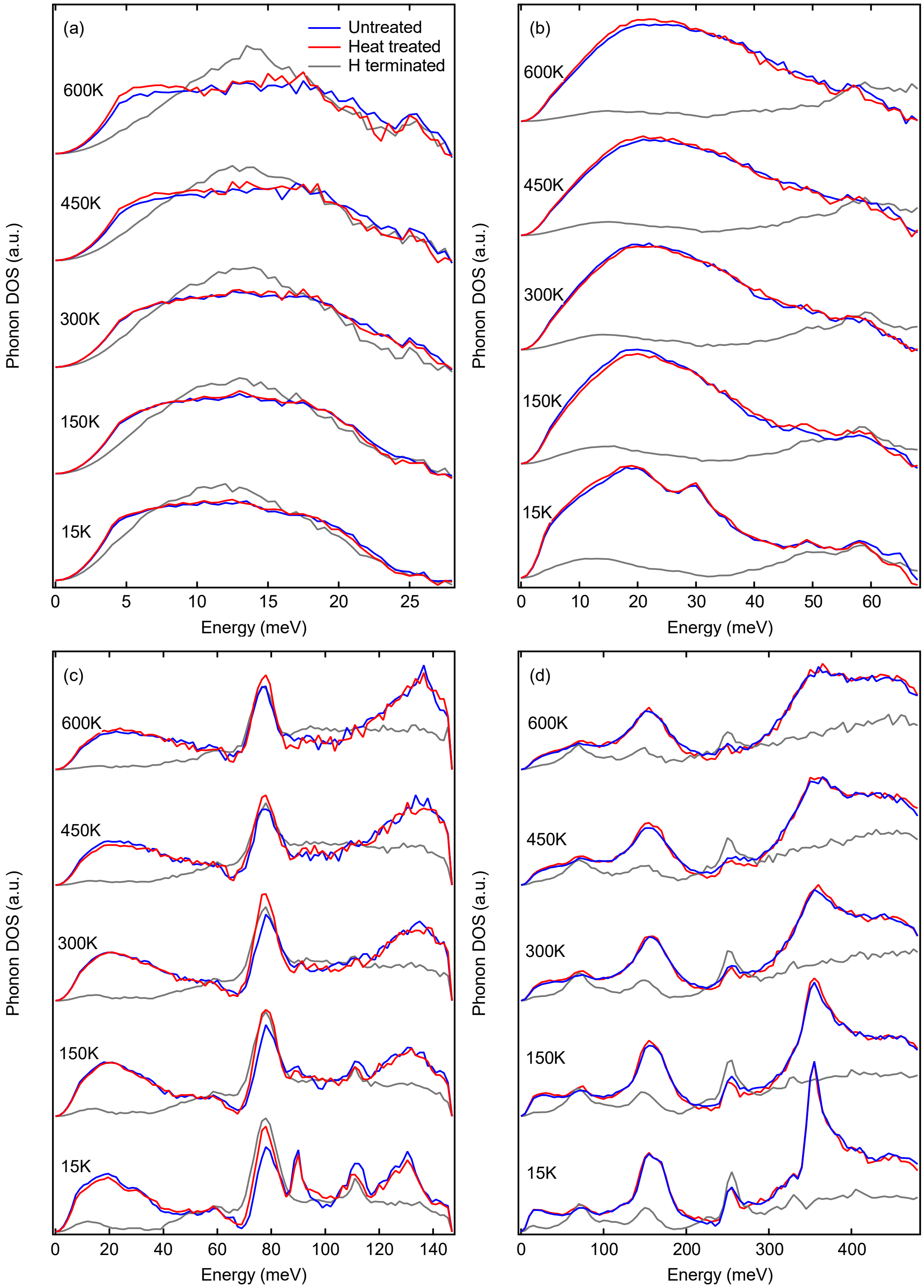
(a)
Untreated
Heat treated
H terminated
600K
450K
300K
150K
15K
Phonon DOS (a.u.)
0
5
10
15
20
25
Energy (meV)
(b)
600K
450K
300K
150K
15K
Phonon DOS (a.u.)
0
10
20
30
40
50
60
Energy (meV)
(c)
600K
450K
300K
150K
15K
Phonon DOS (a.u.)
0
20
40
60
80
100
120
140
Energy (meV)
(d)
600K
450K
300K
150K
15K
Phonon DOS (a.u.)
0
100
200
300
400
Energy (meV)

Figure 4.1 ARCS measured phonon DOSs in the untreated 1-dodecene terminated (blue lines), the heat-treated 1-dodecene terminated (red lines), and the hydrogen-terminated (grey lines) 3-nm spherical silicon nanocrystals at 15, 150, 300, 450, and 600 K with E_i = 30 (a), 75 (b), 150 (c), and 500 meV (d). The phonon DOSs are scaled for clarity.

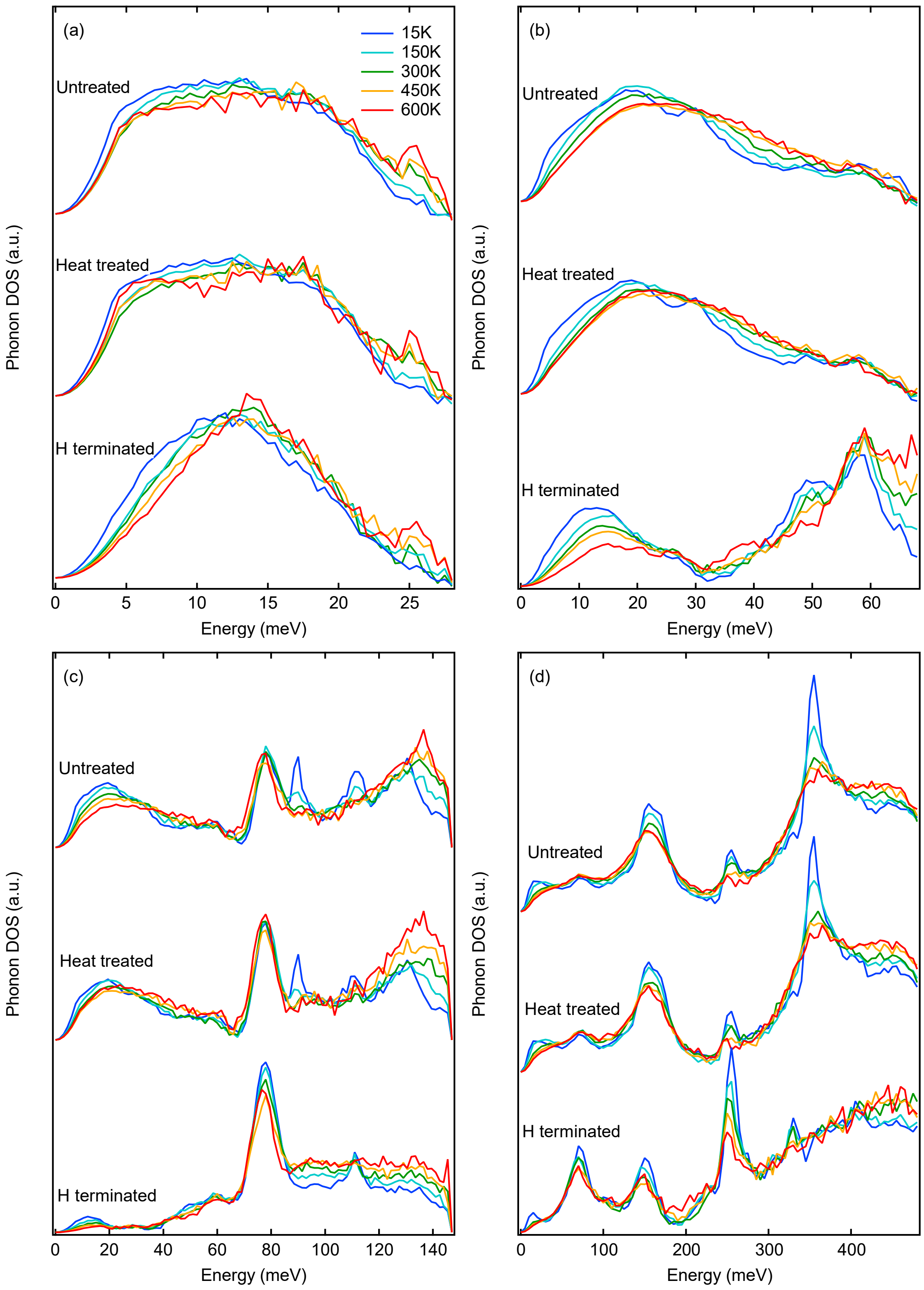
(a)
15K
150K
300K
450K
600K
Untreated
Heat treated
H terminated
Phonon DOS (a.u.)
0
5
10
15
20
25
Energy (meV)
(b)
Untreated
Heat treated
H terminated
Phonon DOS (a.u.)
0
10
20
30
40
50
60
Energy (meV)
(c)
Untreated
Heat treated
H terminated
Phonon DOS (a.u.)
0
20
40
60
80
100
120
140
Energy (meV)
(d)
Untreated
Heat treated
H terminated
Phonon DOS (a.u.)
0
100
200
300
400
Energy (meV)

Figure 4.2 Temperature effect on phonon DOSs in the untreated 1-dodecene terminated, the heat-treated 1-dodecene terminated, and the hydrogen-terminated 3-nm spherical silicon nanocrystals at 15, 150, 300, 450, and 600 K with E_i = 30 (a), 75 (b), 150 (c), and 500 meV (d). The phonon DOSs are scaled for clarity.

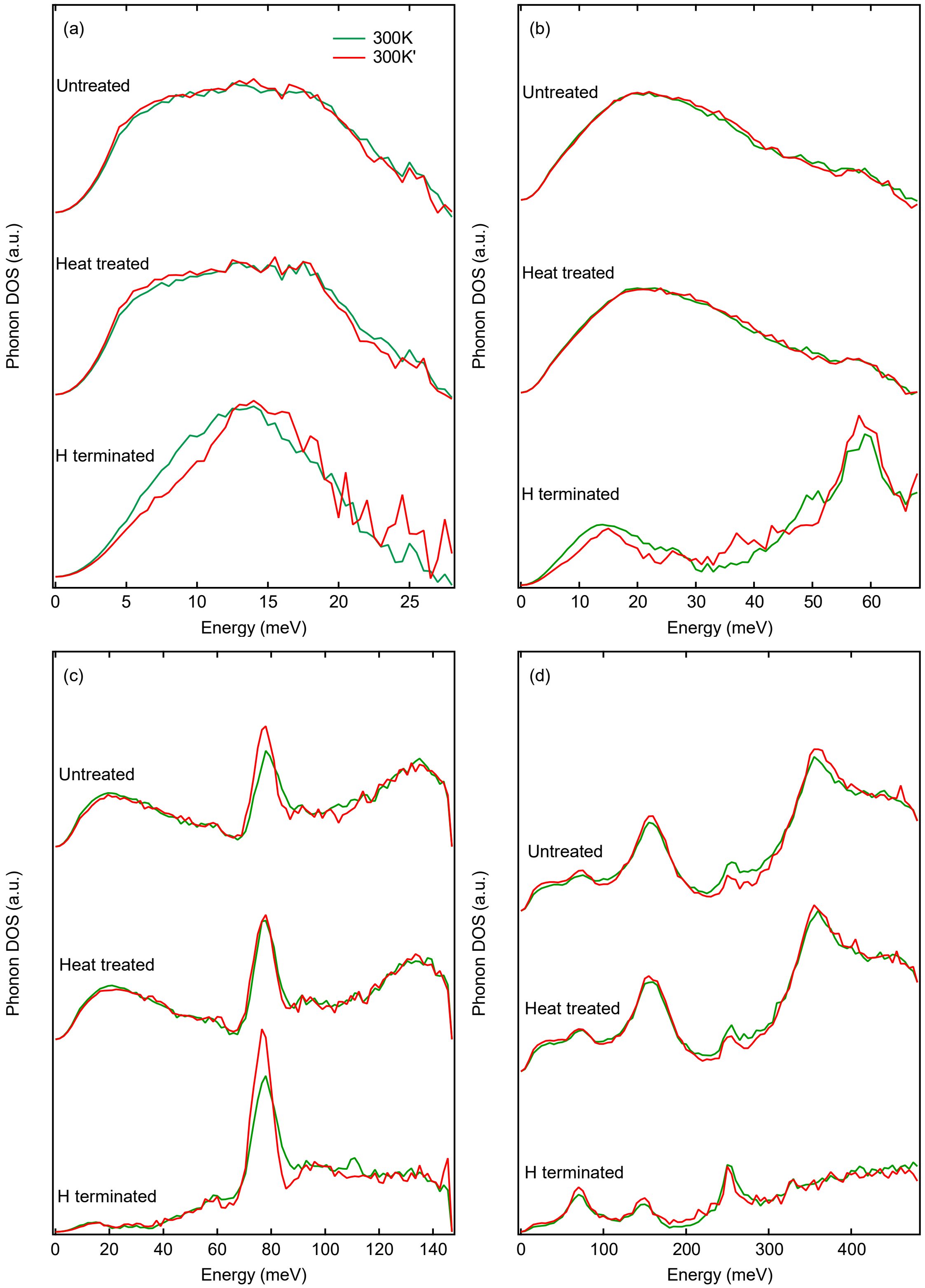
(a)
300K
300K'
Untreated
Heat treated
H terminated
Phonon DOS (a.u.)
0
5
10
15
20
25
Energy (meV)
(b)
Untreated
Heat treated
H terminated
Phonon DOS (a.u.)
0
10
20
30
40
50
60
Energy (meV)
(c)
Untreated
Heat treated
H terminated
Phonon DOS (a.u.)
0
20
40
60
80
100
120
140
Energy (meV)
(d)
Untreated
Heat treated
H terminated
Phonon DOS (a.u.)
0
100
200
300
400
Energy (meV)

Figure 4.3 Phonon DOSs in the untreated 1-dodecene terminated, the heat treated 1-dodecene terminated, and the hydrogen-terminated 3-nm spherical silicon nanocrystals measure when heated up from lower temperature to 300 K (green lines) and when cooled down from higher temperature to 300 K' (red lines) with E_i = 30 (a), 75 (b), 150 (c), and 500 meV (d). The phonon DOSs are scaled for clarity.

The thermal history effect is found to be small on phonon DOSs in the untreated 1-dodecene terminated and the heat-treated 1-dodecene terminated silicon nanocrystals, as shown in Figure 4.3. In contrast, it has a bigger effect on the TA phonon profiles of the hydrogen-terminated nanocrystals, as shown in Figure 4.3(a). The phonon DOS in the hydrogen-terminated nanocrystals measured at 300 K, which was cooled down from 600 K, is compared to phonon DOSs measured at other temperatures to further investigate the temperature effect. Surprisingly, such phonon DOS of silicon TA modes has a similar profile to that measured at 600 K, as shown in Figure 4.4. This indicates that the structural thermal relaxation inside the silicon nanocrystals is irreversible. Thermal history likely has a similar effect on the TA phonon modes in the 1-dodecene terminated silicon nanocrystals. However, such effect was not observed from our data because almost the entire phonon DOSs of the 1-dodecene terminated silicon nanocrystals are largely dominated by the ligand-related hydrogen signals due to the lighter atomic mass and the huge neutron scattering cross section, which is 37.8 times greater than that of silicon, of hydrogen atoms.

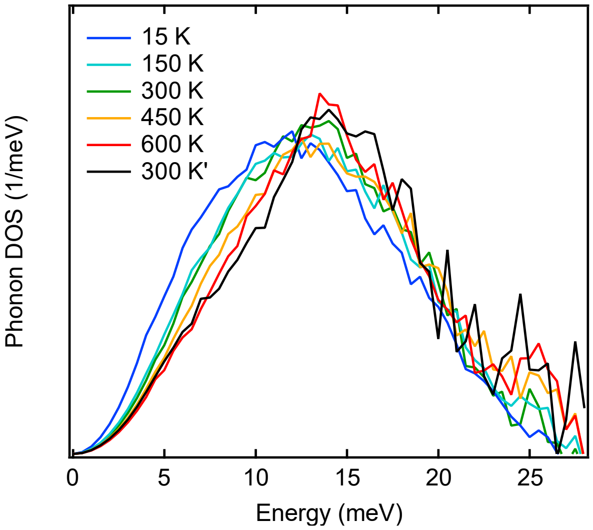

Figure 4.4 Temperature induced hysteresis effect on the normalized TA phonon DOSs of the hydrogen terminated silicon nanocrystals.

On the other hand, the thermal history effect on the higher energy phonon modes, which may have stronger interaction with electrons and contribute to the PL of silicon nanocrystals,[43] can be small. Our observations suggest that the reported effect of heat treatment on the abrupt change in photoluminescence intensity of surface functionalized silicon nanocrystals likely does not directly relate to the modification of phonon dynamics.

4.6 Conclusion

Phonon DOSs of the untreated 1-dodecene terminated, the heat-treated 1-dodecene terminated, and the hydrogen-terminated 3-nm spherical silicon nanocrystals were measured using INS at different temperatures to investigate the effect of organic surface ligands on the phonon dynamics in silicon nanocrystals. We found that the phonon DOSs of the 1-dodecene terminated silicon nanocrystals are dominated by hydrogen-related phonon modes and are largely different from those of their hydrogen-terminated counterparts. Small effects from the heat treatment on the phonon dynamics of 1-dodecene terminated silicon nanocrystals were also observed because of the dominant hydrogen signals. In addition, the thermal relaxation of silicon nanocrystals was found to be irreversible. This work sheds light on the phonon dynamics in surface functionalized silicon nano systems and will benefit the further investigation of the origin of the photoluminescence in spatially confined silicon systems.

4.7 Reference

(1) Rastogi, A.; Tripathi, D. K.; Yadav, S.; Chauhan, D. K.; Živčák, M.; Ghorbanpour, M.; El-Sheery, N. I.; Brestic, M. Application of Silicon Nanoparticles in Agriculture. *3 Biotech* **2019**, *9* (3), 90.

(2) Jeelani, P. G.; Mulay, P.; Venkat, R.; Ramalingam, C. Multifaceted Application of Silica Nanoparticles. A Review. *Silicon* **2020**, *12* (6), 1337–1354.

(3) Ranjbar-Navazi, Z.; Omidi, Y.; Eskandani, M.; Davaran, S. Cadmium-Free Quantum Dot-Based Theranostics. *TrAC Trends Anal. Chem.* **2019**, *118*, 386–400.

(4) Alsharif, N. H.; Berger, C. E. M.; Varanasi, S. S.; Chao, Y.; Horrocks, B. R.; Datta, H. K. Alkyl-Capped Silicon Nanocrystals Lack Cytotoxicity and Have Enhanced Intracellular Accumulation in Malignant Cells via Cholesterol-Dependent Endocytosis. *Small* **2009**, *5* (2), 221–228.

(5) Bhattacharjee, S.; Rietjens, I. M. C. M.; Singh, M. P.; Atkins, T. M.; Purkait, T. K.; Xu, Z.; Regli, S.; Shukaliak, A.; Clark, R. J.; Mitchell, B. S.; Alink, G. M.; Marcelis, A. T. M.; Fink, M. J.; Veinot, J. G. C.; Kauzlarich, S. M.; Zuilhof, H. Cytotoxicity of Surface-Functionalized Silicon and Germanium Nanoparticles: The Dominant Role of Surface Charges. *Nanoscale* **2013**, *5* (11), 4870–4883.

(6) Erogbogbo, F.; Yong, K.-T.; Roy, I.; Hu, R.; Law, W.-C.; Zhao, W.; Ding, H.; Wu, F.; Kumar, R.; Swihart, M. T.; Prasad, P. N. In Vivo Targeted Cancer Imaging, Sentinel Lymph Node Mapping and Multi-Channel Imaging with Biocompatible Silicon Nanocrystals. *ACS Nano* **2011**, *5* (1), 413–423.

(7) Liu, J.; Erogbogbo, F.; Yong, K.-T.; Ye, L.; Liu, J.; Hu, R.; Chen, H.; Hu, Y.; Yang, Y.; Yang, J.; Roy, I.; Karker, N. A.; Swihart, M. T.; Prasad, P. N. Assessing Clinical Prospects of Silicon Quantum Dots: Studies in Mice and Monkeys. *ACS Nano* **2013**, *7* (8), 7303–7310.

(8) Park, J. H.; Gu, L.; Von Maltzahn, G.; Ruoslahti, E.; Bhatia, S. N.; Sailor, M. J. Biodegradable Luminescent Porous Silicon Nanoparticles for in Vivo Applications. *Nat. Mater.* **2009**, *8* (4), 331–336.

(9) Warner, J. H.; Hoshino, A.; Yamamoto, K.; Tilley, R. D. Water-Soluble Photoluminescent Silicon Quantum Dots. *Angew. Chemie Int. Ed.* **2005**, *44* (29), 4550–4554.

(10) Shiohara, A.; Prabakar, S.; Faramus, A.; Hsu, C.-Y.; Lai, P.-S.; Northcote, P. T.; Tilley, R. D. Sized Controlled Synthesis, Purification, and Cell Studies with Silicon Quantum Dots. *Nanoscale* **2011**, *3* (8), 3364–3370.

(11) Morozova, S.; Alikina, M.; Vinogradov, A.; Pagliaro, M. Silicon Quantum Dots: Synthesis, Encapsulation, and Application in Light-Emitting Diodes. *Frontiers in Chemistry*. 2020, p 191.

(12) Xu, K. Silicon MOS Optoelectronic Micro-Nano Structure Based on Reverse-Biased PN Junction. *Phys. status solidi* **2019**, *216* (7), 1800868.

(13) Oh, J.; Yuan, H.-C.; Branz, H. M. An 18.2%-Efficient Black-Silicon Solar Cell Achieved through Control of Carrier Recombination in Nanostructures. *Nat. Nanotechnol.* **2012**, *7* (11), 743–748.

(14) Biswas, R.; Xu, C. Nano-Crystalline Silicon Solar Cell Architecture with Absorption at the Classical 4n2 Limit. *Opt. Express* **2011**, *19* (S4), A664–A672.

(15) Dimitrov, D. Z.; Du, C.-H. Crystalline Silicon Solar Cells with Micro/Nano Texture. *Appl. Surf. Sci.* **2013**, *266*, 1–4.

(16) Nayak, B. K.; Iyengar, V. V; Gupta, M. C. Efficient Light Trapping in Silicon Solar Cells by Ultrafast-Laser-Induced Self-Assembled Micro/Nano Structures. *Prog. Photovoltaics Res. Appl.* **2011**, *19* (6), 631–639.

(17) Ponomareva, I.; Srivastava, D.; Menon, M. Thermal Conductivity in Thin Silicon Nanowires : Phonon Confinement Effect. *Nano Lett.* **2007**, *7* (5), 1155–1159.

(18) Alvarez, F. X.; Jou, D.; Sellitto, A. Pore-Size Dependence of the Thermal Conductivity of Porous Silicon : A Phonon Hydrodynamic Approach. *Appl. Phys. Lett.* **2010**, *97* (3), 33103.

(19) Li, X.; Maute, K.; Dunn, M. L.; Yang, R. Strain Effects on the Thermal Conductivity of Nanostructures. *Phys. Rev. B* **2010**, *81* (24), 245318.

(20) Chávez-Ángel, E.; Reparaz, J. S.; Gomis-Bresco, J.; Wagner, M. R.; Cuffe, J.; Graczykowski, B.; Shchepetov, A.; Jiang, H.; Prunnila, M.; Ahopelto, J.; Alzina, F.; Sotomayor Torres, C. M. Reduction of the Thermal Conductivity in Free-Standing Silicon Nano-Membranes Investigated by Non-Invasive Raman Thermometry. *APL Mater.* **2014**, *2* (1), 12113.

(21) Richter, A.; Steiner, P.; Kozlowski, F.; Lang, W. Current-Induced Light Emission from a Porous Silicon Device. *IEEE Electron Device Lett.* **1991**, *12* (12), 691–692.

(22) Jiang, D. T.; Coulthard, I.; Sham, T. K.; Lorimer, J. W.; Frigo, S. P.; Feng, X. H.; Rosenberg, R. A. Observations on the Surface and Bulk Luminescence of Porous Silicon. *J. Appl. Phys.* **1993**, *74* (10), 6335–6340.

(23) Bergren, M. R.; Palomaki, P. K. B.; Neale, N. R.; Furtak, T. E.; Beard, M. C. Size-Dependent Exciton Formation Dynamics in Colloidal Silicon Quantum Dots. *ACS Nano* **2016**, *10* (2), 2316–2323.

(24) Joo, B. S.; Gu, M.; Han, J.; Jung, N.; Kim, S.; Park, D.-W.; Han, M. Decay Time Dynamics of Red and Blue Luminescence of Surface-Functionalized Silicon Quantum Dots. *J. Lumin.* **2021**, *236*, 118121.

(25) Hua, F.; Erogbogbo, F.; Swihart, M. T.; Ruckenstein, E. Organically Capped Silicon Nanoparticles with Blue Photoluminescence Prepared by Hydrosilylation Followed by Oxidation. *Langmuir* **2006**, *22* (9), 4363–4370.

(26) Hill, S. K. E.; Connell, R.; Peterson, C.; Hollinger, J.; Hillmyer, M. A.; Kortshagen, U.; Ferry, V. E. Silicon Quantum Dot–Poly(Methyl Methacrylate) Nanocomposites with Reduced Light Scattering for Luminescent Solar Concentrators. *ACS Photonics* **2019**, *6* (1), 170–180.

(27) Brown, S. L.; Vogel, D. J.; Miller, J. B.; Inerbaev, T. M.; Anthony, R. J.; Kortshagen, U. R.; Kilin, D. S.; Hobbie, E. K. Enhancing Silicon Nanocrystal Photoluminescence through Temperature and Microstructure. *J. Phys. Chem. C* **2016**, *120* (33), 18909–18916.

(28) Lopez, T.; Mangolini, L. On the Nucleation and Crystallization of Nanoparticles in Continuous-Flow Nonthermal Plasma Reactors. *J. Vac. Sci. Technol. B* **2014**, *32* (6), 61802.

(29) Mangolini, L.; Thimsen, E.; Kortshagen, U. High-Yield Plasma Synthesis of Luminescent Silicon Nanocrystals. *Nano Lett.* **2005**, *5* (4), 655–659.

(30) Mangolini, L.; Jurbergs, D.; Rogojina, E.; Kortshagen, U. High Efficiency Photoluminescence from Silicon Nanocrystals Prepared by Plasma Synthesis and Organic Surface Passivation. *Phys. status solidi c* **2006**, *3* (11), 3975–3978.

(31) Lin, J. Y. Y.; Banerjee, A.; Islam, F.; Le, M. D.; Abernathy, D. L. Energy Dependence of the Flux and Elastic Resolution for the ARCS Neutron Spectrometer. *Phys. B Condens. Matter* **2019**, *562*, 26–30.

(32) Taylor, J.; Arnold, O.; Bilheaux, J.; Buts, A.; Campbell, S.; Doucet, M.; Draper, N.; Fowler, R.; Gigg, M.; Lynch, V.; Markvardsen, A.; Palmen, K.; Parker, P.; Peterson, P.; Ren, S.; Reuter, M.; Savici, A.; Taylor, R.; Tolchenov, R.; Whitley, R.; Zhou, W, J. *Mantid, A High Performance Framework for Reduction and Analysis of Neutron Scattering Data*; 2012.

(33) Kresch, M.; Delaire, O.; Stevens, R.; Lin, J. Y. Y.; Fultz, B. Neutron Scattering Measurements of Phonons in Nickel at Elevated Temperatures. *Phys. Rev. B* **2007**, *75* (10), 104301.

(34) Lucas, M. S.; Kresch, M.; Stevens, R.; Fultz, B. Phonon Partial Densities of States and Entropies of Fe and Cr in Bcc Fe-Cr from Inelastic Neutron Scattering. *Phys. Rev. B* **2008**, *77* (18), 184303.

(35) Delaire, O.; Kresch, M.; Muñoz, J. A.; Lucas, M. S.; Lin, J. Y. Y.; Fultz, B. Electron-Phonon Interactions and High-Temperature Thermodynamics of Vanadium and Its Alloys. *Phys. Rev. B* **2008**, *77* (21), 214112.

(36) Ono, T.; Xu, Y.; Sakata, T.; Saitow, K. Designing Efficient Si Quantum Dots and LEDs by Quantifying Ligand Effects. *ACS Appl. Mater. Interfaces* **2022**, *14* (1), 1373–1388.

(37) Valentin, A.; Sée, J.; Galdin-Retailleau, S.; Dollfus, P. Study of Phonon Modes in Silicon Nanocrystals Using the Adiabatic Bond Charge Model. *J. Phys. Condens. Matter* **2008**, *20* (14), 145213.

(38) Hu, X.; Zi, J. Reconstruction of Phonon Dispersion in Si Nanocrystals. *J. Phys. Condens. Matter* **2002**, *14* (41), L671–L677.

(39) Kim, D. S.; Smith, H. L.; Niedziela, J. L.; Li, C. W.; Abernathy, D. L.; Fultz, B. Phonon Anharmonicity in Silicon from 100 to 1500 K. *Phys. Rev. B* **2015**, *91* (1), 14307.

(40) Chen, S.; Coleman, D.; Abernathy, D. L.; Banerjee, A.; Daemen, L. L.; Mangolini, L.; Li, C. W. Giant Low-Temperature Anharmonicity in Silicon Nanocrystals. *Phys. Rev. Mater.* **2020**, *4* (5), 56001.

(41) Chen, S.; Coleman, D.; Abernathy, D. L.; Banerjee, A.; Mangolini, L.; Li, C. Distinct Acoustic and Optical Phonon Dependences on Particle Size, Oxidation, and Temperature in Silicon Nanocrystals. *J. Phys. Chem. C* **2022**, *126* (30), 12704–12711.

(42) Li, Z.; Kortshagen, U. R. Aerosol-Phase Synthesis and Processing of Luminescent Silicon Nanocrystals. *Chem. Mater.* **2019**, *31* (20), 8451–8458.

(43) Monserrat, B.; Needs, R. J. Comparing Electron-Phonon Coupling Strength in Diamond, Silicon, and Silicon Carbide: First-Principles Study. *Phys. Rev. B* **2014**, *89* (21), 214304.

Chapter 5

Anisotropic Structure Variations in Silicon Nanocrystals

5.1 Abstract

Spatially confined silicon systems, with many mesmerizing properties such as photoluminescence, carry great application potential in the industries of novel electronic devices, light-emitting devices, photovoltaic cells, and biomedical fields. Many properties of the silicon nano systems have been extensively investigated, however, their atomic structures remain elusive. In order to better understand the morphology of quantum-sized silicon systems, we measured the diffraction spectra of 3-nm silicon nanocrystals using elastic neutron scattering. We observed huge anisotropic structure variations in silicon nanocrystals, where the lattice constant in the [0 2 2] direction is about 1.5% smaller than the corresponding bulk value while the lattice constant in the [1 1 3] direction is about 1.5% bigger than the corresponding bulk value. Our study sheds light on the structure of spatially confined silicon systems from a microscopic perspective and will facilitate the investigations of many physical and mechanical properties of quantum-sized silicon systems.

5.2 Introduction

As the second most earth-abundant element in the crust, silicon has been widely used in numerous industries with electronic, construction, and chemical applications. To make things better, this field has grown enormously after the observations of the photoluminescent property of spatially confined silicon systems, which remain an area of great interest.[1–6] Recent studies show luminescent silicon nanocrystals carry great potential in the optoelectronic[7–12] and biomedical industries as a novel non-toxic, bio-compatible, and bio-degradable material.[13–20] In addition, surface functionalized silicon nanocrystals have also drawn an increasing amount of attention because these systems possess the properties of silicon nanocrystals, the functionalized ligands, and the hybrid characteristics arising from the synergistic interactions between the components, as discussed in Chapter 4.[21–23]

Driven by the great applications of quantum-sized silicon systems, studies have been carried out to investigate their physical properties, however, their atomic structures are still unclear, regardless of many theoretical models proposed for calculations.[24,25] Previous studies show the lattice constants of silicon nanocrystals are particle size dependent. This makes good control of particle size distribution a critical requirement for the success of the measurement. However, many synthesis methods including wet chemistry methods are not ideal to produce silicon nanocrystals with narrow particle size distribution.

In this chapter, we measured the diffraction spectra of 3-nm silicon nanocrystals synthesized by a non-thermal plasma process[26,27], which provides great control of particle size distribution, using elastic neutron scattering. This work sheds light on the atomic structure of spatially confined silicon systems and will benefit further investigation and the development of silicon-based nano-systems.

5.3 Materials and methods

The 3-nm spherical silicon nanocrystals were synthesized by a non-thermal plasma process.[26,27] The fabrication details are described in our previous paper and Chapter 2.[28]

The size of silicon nanocrystals was controlled by adjusting the reactor pressure and precursor flow rates. The surfaces of the as-produced silicon nanocrystals were terminated by hydrogen atoms from the precursor silane and hydrogen gas used for the reaction. The synthesized 3-nm silicon nanocrystals were carefully collected on stainless steel 400-grade mesh, then transferred into a glovebox via an air-free transfer chamber. In the glovebox, the nanocrystals were removed from the mesh and placed in the center of a 1” quartz tube with quarter-turn vacuum seals on each end to avoid surface oxidation.

The elastic neutron scattering measurements were performed on the Powder Diffractometer (POWGEN), a third-generation time-of-flight general-purpose neutron powder diffractometer at Oak Ridge National Laboratory. POWGEN has a d-space resolution of 2.5% or better.[29] Frame 2 was chosen for good resolutions and counting statistics. The choppers rotate at 60 Hz and allow a white neutron beam with a center wavelength of 1.5 Å to reach samples. The d-space coverage with this frame is 0.5-12.5 Å. The diffraction spectra of 3-nm silicon nanocrystals were measured at 15, 75, 100, 125, 150, 175, 200 K, and at room temperature to investigate the thermal expansion behaviors of silicon nanocrystals. The samples are expected to remain unoxidized during the measurement.

5.4 Data processing

Mantid software was used for data processing.[30] The event data of POWGEN contains information about the detector number and the time-of-arrival of each scattered neutron. The interatomic spacing d was calculated from its time-of-flight and scattering geometry, with the knowledge of the distance between detectors and the sample by combining Bragg’s law and de Broglie’s equation:

$$\lambda = \frac{ht}{mL} = 2d\ \sin\theta \tag{5.1}$$

$$d = \frac{ht}{2mL\ \sin\theta}$$

where λ, h, t, m, L, and θ are the neutron wavelength, the Planck’s constant, the time-of-flight of neutrons, the mass of neutron, the total flight path, and the scattering angle, respectively. The instrument responses were calibrated using a vanadium rod of diameter 6.35 mm, measuring for several hours to collect appropriate statistics. Backgrounds from an empty can were subtracted from the signals with the equation scheme:

$$I = \frac{\text{Sample} - \text{Empty can}}{\text{Vanadium rod} - \text{ Empty environment for V rod}} \tag{5.2}$$

where I is the corrected signal intensity of the diffraction spectrum.

5.5 Calculation

Neutron diffraction spectrum of crystalline silicon with a space group of $\mathrm{Fd\bar{3}m}$ and a lattice constant of 5.43 Å according to the reported values,[31,32] as shown in Figure 5.1,

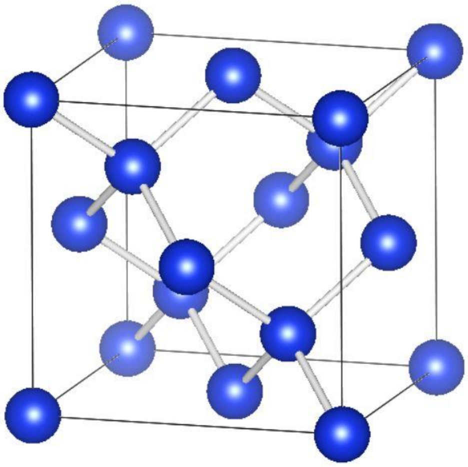

Figure 5.1 The atomic structure of the silicon unit cell used for the calculation.

was calculated using CrystalDiffract®. The particle size was set to 3 nm. The change of particle only changes the widths of the diffraction peaks and does not affect the values of peak centers. The calculated signal intensity was weighted by the cross section of the time-of-flight neutron.

5.6 Result and discussion

The diffraction spectra of our 3-nm silicon nanocrystal samples agree with the calculated diffraction patten of the 3-nm crystalline silicon in general, as shown in Figure 5.2(a). Such general agreement confirms that our 3-nm silicon nanocrystal samples have similar short-range interatomic structures to those of crystalline silicon. However, a few remarkable discrepancies between our experimental data and the calculation suggests that the interatomic structure of our silicon nanocrystal samples can still be different from the crystalline structure in bulk silicon in many aspects.

Firstly, even though the measured diffraction peaks match the calculated result relatively well, a few offsets of the experimental data from the calculation are quite pronounced, especially for the diffraction peaks at 1.36, 1.6, and 1.9 Å, which correspond to the interplanar spacing along [0 0 4], [1 1 3], and [0 2 2] directions, respectively. These diffraction peaks were fitted with Gaussian functions, as shown in Figure 5.2(b) and (c), to determine the average interplanar distances in the 3-nm silicon nanocrystal samples and compare to the calculated values. The Gaussian functions provide good fits to our measurements and the fitting results are summarized in Figure 5.3.

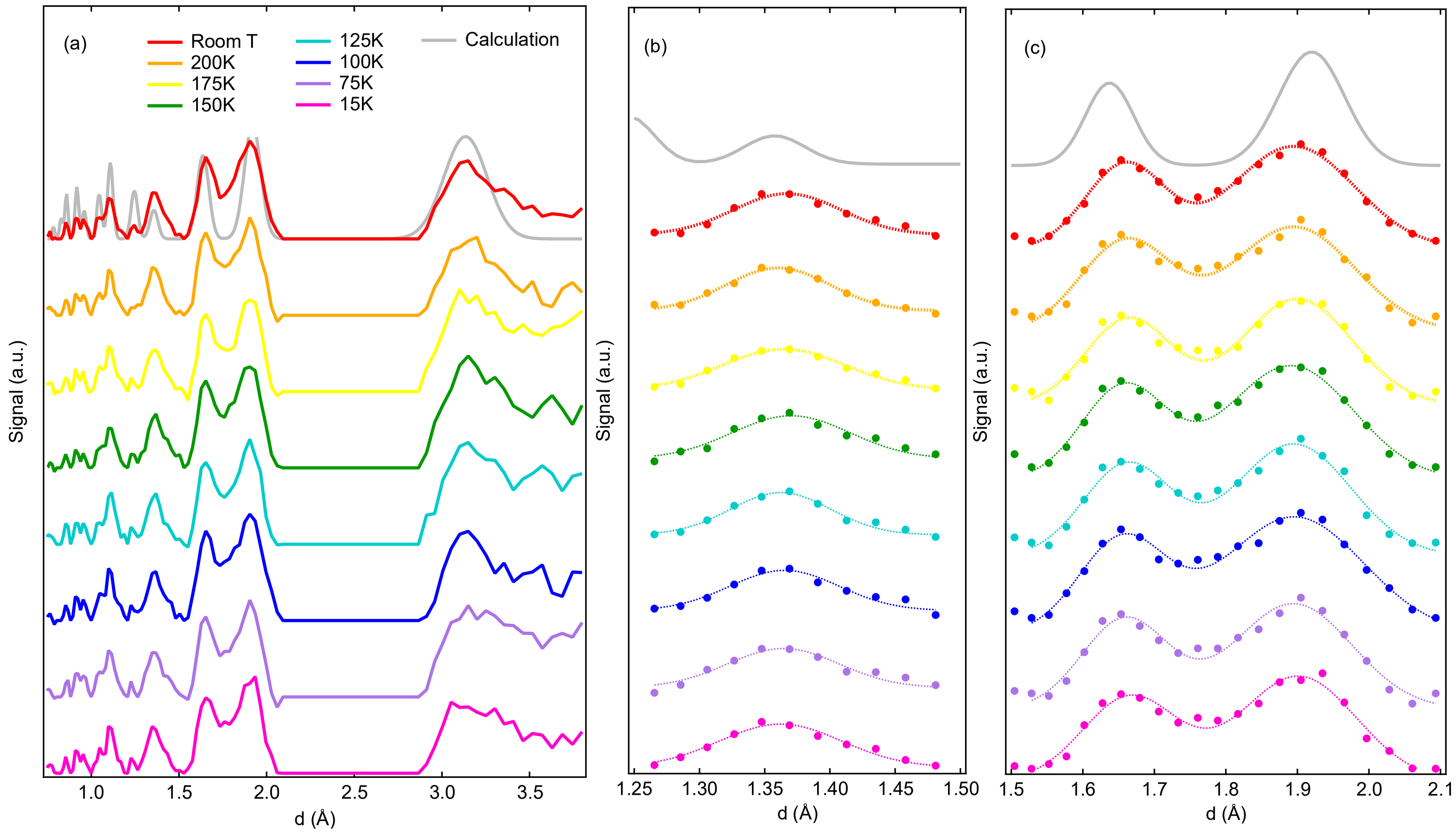
(a)
Room T
200K
175K
150K
125K
100K
75K
15K
Calculation
Signal (a.u.)
1.0
1.5
2.0
2.5
3.0
3.5
d (Å)
(b)
Signal (a.u.)
1.25
1.30
1.35
1.40
1.45
1.50
d (Å)
(c)
Signal (a.u.)
1.5
1.6
1.7
1.8
1.9
2.0
2.1
d (Å)

Figure 5.2 (a) Diffraction spectra (colored lines) of our 3-nm silicon nanocrystal samples measured in the temperature range from 15 K to room temperature. The calculated diffraction spectrum (gray line) of the 3-nm crystalline silicon is plotted as a reference. (b) Gaussian fits (colored dash lines) to the diffraction peaks (colored markers) near 1.36 Å. (c) Double Gaussian fits to the diffraction peaks near 1.6 and 1.9 Å. Notations are the same as (b).

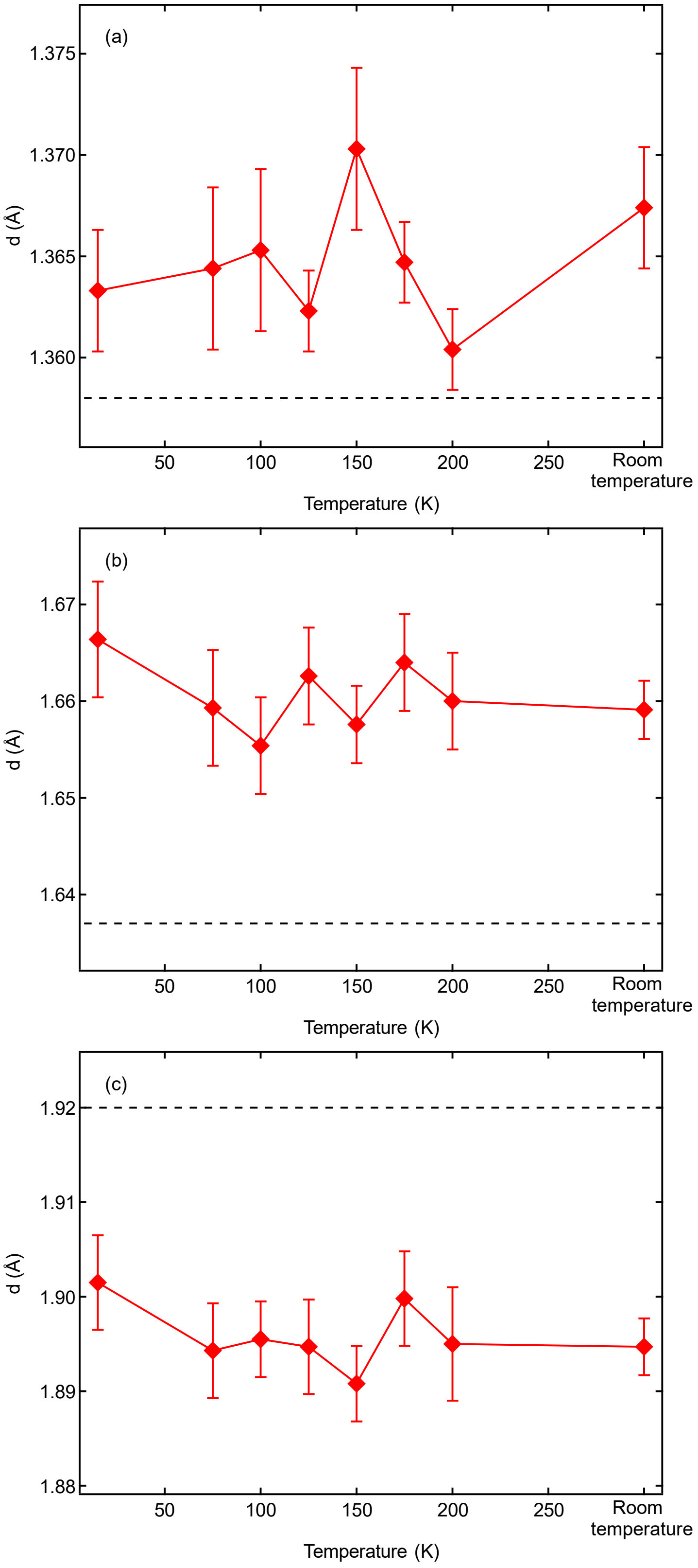
(a)
1.375
1.370
1.365
1.360
d (Å)
50
100
150
200
250
Room temperature
Temperature (K)
(b)
1.67
1.66
1.65
1.64
d (Å)
50
100
150
200
250
Room temperature
Temperature (K)
(c)
1.92
1.91
1.90
1.89
1.88
d (Å)
50
100
150
200
250
Room temperature
Temperature (K)

Figure 5.3 Gaussian fitted interatomic distances of the diffraction peaks near (a) 1.36 Å, (b) 1.6 Å, and (c) 1.96 Å. The error bars show the fitting errors. The red lines are guides to the eye. The black dash lines show the calculated interatomic distances of the corresponding interatomic distances in crystalline silicon with a lattice constant of 5.43 Å.

Surprisingly, gigantic anisotropic structure variations are observed in 3-nm silicon nanocrystals, as shown in Figure 5.3. The measured interplanar distance along [0 0 4] and [1 1 3] directions are about 0.5% and 1.5% larger than the calculated values in the temperature range from 15 K to room temperature, respectively, as shown in Figure 5.3(a) and (b). In contrast, the measured interplanar distance in [0 2 2] direction is 1.5% smaller than the calculated values, as shown in Figure 5.3(c). Such observations indicate that the atomic structures in the silicon nanocrystals are intrinsically different from that of crystalline bulk silicon. The differences between the structures of the spatially confined and the bulk system are systematically anisotropic instead of simple lattice compression or expansion.

In addition, the experimentally measured diffraction spectra are about 2 times broader than the calculated diffraction spectrum, as shown in Figure 5.2. Such broadening likely comes from the particle size distribution of our nanocrystal samples. The broadening greatly overshadows the temperature-induced lattice evolution of silicon nanocrystals, as shown in Figure 5.3, even though fitting errors are about only 0.3%. As a result, we were not able to extract any thermal expansion information from this experiment. Better control over the particle size distribution and more counting statistics will be helpful in order to obtain more accurate structural information about silicon nanocrystals.

5.7 Conclusion

Gigantic anisotropic structure variations are observed in 3-nm spherical silicon nanocrystals using elastic neutron scattering. The lattice constants of silicon nanocrystals are bigger than those of crystalline bulk silicon along [0 0 4] and [1 1 3] directions, while the lattice constant is smaller than the bulk value in [0 2 2] direction. Our research sheds light on the atomic structure of spatially confined silicon systems and will benefit further investigation and the development of silicon-based nano-systems.

5.8 References

(1) Mangolini, L. Synthesis, Properties, and Applications of Silicon Nanocrystals. *J. Vac. Sci. Technol. B* **2013**, *31* (2), 20801.

(2) Li, Q.; Luo, T.-Y.; Zhou, M.; Abroshan, H.; Huang, J.; Kim, H. J.; Rosi, N. L.; Shao, Z.; Jin, R. Silicon Nanoparticles with Surface Nitrogen: 90% Quantum Yield with Narrow Luminescence Bandwidth and the Ligand Structure Based Energy Law. *ACS Nano* **2016**, *10* (9), 8385–8393.

(3) Jurbergs, D.; Rogojina, E.; Mangolini, L.; Kortshagen, U. Silicon Nanocrystals with Ensemble Quantum Yields Exceeding 60%. *Appl. Phys. Lett.* **2006**, *88* (23), 233116.

(4) Miller, J. B.; Van Sickle, A. R.; Anthony, R. J.; Kroll, D. M.; Kortshagen, U. R.; Hobbie, E. K. Ensemble Brightening and Enhanced Quantum Yield in Size-Purified Silicon Nanocrystals. *ACS Nano* **2012**, *6* (8), 7389–7396.

(5) Mastronardi, M. L.; Maier-Flaig, F.; Faulkner, D.; Henderson, E. J.; Kübel, C.; Lemmer, U.; Ozin, G. A. Size-Dependent Absolute Quantum Yields for Size-Separated Colloidally-Stable Silicon Nanocrystals. *Nano Lett.* **2012**, *12* (1), 337–342.

(6) Gelloz, B.; Juangsa, F. B.; Nozaki, T.; Asaka, K.; Koshida, N.; Jin, L. Si/SiO2 Core/Shell Luminescent Silicon Nanocrystals and Porous Silicon Powders With High Quantum Yield, Long Lifetime, and Good Stability. *Frontiers in Physics*. 2019, p 47.

(7) Morozova, S.; Alikina, M.; Vinogradov, A.; Pagliaro, M. Silicon Quantum Dots: Synthesis, Encapsulation, and Application in Light-Emitting Diodes. *Frontiers in Chemistry*. 2020, p 191.

(8) Xu, K. Silicon MOS Optoelectronic Micro-Nano Structure Based on Reverse-Biased PN Junction. *Phys. status solidi* **2019**, *216* (7), 1800868.

(9) Oh, J.; Yuan, H.-C.; Branz, H. M. An 18.2%-Efficient Black-Silicon Solar Cell Achieved through Control of Carrier Recombination in Nanostructures. *Nat. Nanotechnol.* **2012**, *7* (11), 743–748.

(10) Biswas, R.; Xu, C. Nano-Crystalline Silicon Solar Cell Architecture with Absorption at the Classical 4n2 Limit. *Opt. Express* **2011**, *19* (S4), A664–A672.

(11) Dimitrov, D. Z.; Du, C.-H. Crystalline Silicon Solar Cells with Micro/Nano Texture. *Appl. Surf. Sci.* **2013**, *266*, 1–4.

(12) Nayak, B. K.; Iyengar, V. V; Gupta, M. C. Efficient Light Trapping in Silicon Solar

Cells by Ultrafast-Laser-Induced Self-Assembled Micro/Nano Structures. *Prog. Photovoltaics Res. Appl.* **2011**, *19* (6), 631–639.

(13) Ranjbar-Navazi, Z.; Omidi, Y.; Eskandani, M.; Davaran, S. Cadmium-Free Quantum Dot-Based Theranostics. *TrAC Trends Anal. Chem.* **2019**, *118*, 386–400.

(14) Alsharif, N. H.; Berger, C. E. M.; Varanasi, S. S.; Chao, Y.; Horrocks, B. R.; Datta, H. K. Alkyl-Capped Silicon Nanocrystals Lack Cytotoxicity and Have Enhanced Intracellular Accumulation in Malignant Cells via Cholesterol-Dependent Endocytosis. *Small* **2009**, *5* (2), 221–228.

(15) Bhattacharjee, S.; Rietjens, I. M. C. M.; Singh, M. P.; Atkins, T. M.; Purkait, T. K.; Xu, Z.; Regli, S.; Shukaliak, A.; Clark, R. J.; Mitchell, B. S.; Alink, G. M.; Marcelis, A. T. M.; Fink, M. J.; Veinot, J. G. C.; Kauzlarich, S. M.; Zuilhof, H. Cytotoxicity of Surface-Functionalized Silicon and Germanium Nanoparticles: The Dominant Role of Surface Charges. *Nanoscale* **2013**, *5* (11), 4870–4883.

(16) Erogbogbo, F.; Yong, K.-T.; Roy, I.; Hu, R.; Law, W.-C.; Zhao, W.; Ding, H.; Wu, F.; Kumar, R.; Swihart, M. T.; Prasad, P. N. In Vivo Targeted Cancer Imaging, Sentinel Lymph Node Mapping and Multi-Channel Imaging with Biocompatible Silicon Nanocrystals. *ACS Nano* **2011**, *5* (1), 413–423.

(17) Liu, J.; Erogbogbo, F.; Yong, K.-T.; Ye, L.; Liu, J.; Hu, R.; Chen, H.; Hu, Y.; Yang, Y.; Yang, J.; Roy, I.; Karker, N. A.; Swihart, M. T.; Prasad, P. N. Assessing Clinical Prospects of Silicon Quantum Dots: Studies in Mice and Monkeys. *ACS Nano* **2013**, *7* (8), 7303–7310.

(18) Park, J. H.; Gu, L.; Von Maltzahn, G.; Ruoslahti, E.; Bhatia, S. N.; Sailor, M. J. Biodegradable Luminescent Porous Silicon Nanoparticles for in Vivo Applications. *Nat. Mater.* **2009**, *8* (4), 331–336.

(19) Warner, J. H.; Hoshino, A.; Yamamoto, K.; Tilley, R. D. Water-Soluble Photoluminescent Silicon Quantum Dots. *Angew. Chemie Int. Ed.* **2005**, *44* (29), 4550–4554.

(20) Shiohara, A.; Prabakar, S.; Faramus, A.; Hsu, C.-Y.; Lai, P.-S.; Northcote, P. T.; Tilley, R. D. Sized Controlled Synthesis, Purification, and Cell Studies with Silicon Quantum Dots. *Nanoscale* **2011**, *3* (8), 3364–3370.

(21) Liu, C.-Y.; Holman, Z. C.; Kortshagen, U. R. Hybrid Solar Cells from P3HT and Silicon Nanocrystals. *Nano Lett.* **2009**, *9* (1), 449–452.

(22) Mitra, S.; Cook, S.; Švrček, V.; Blackley, R. A.; Zhou, W.; Kovač, J.; Cvelbar, U.; Mariotti, D. Improved Optoelectronic Properties of Silicon Nanocrystals/Polymer

Nanocomposites by Microplasma-Induced Liquid Chemistry. *J. Phys. Chem. C* **2013**, *117* (44), 23198–23207.

(23) Hessel, C. M.; Rasch, M. R.; Hueso, J. L.; Goodfellow, B. W.; Akhavan, V. A.; Puvanakrishnan, P.; Tunnel, J. W.; Korgel, B. A. Alkyl Passivation and Amphiphilic Polymer Coating of Silicon Nanocrystals for Diagnostic Imaging. *Small* **2010**, *6* (18), 2026–2034.

(24) Zachariah, M. R.; Carrier, M. J.; Blaisten-Barojas, E. Properties of Silicon Nanoparticles : A Molecular Dynamics Study. *J. Phys. Chem.* **1996**, *100* (36), 14856–14864.

(25) Zhou, Z.; Steigerwald, M. L.; Friesner, R. A.; Brus, L.; Hybertsen, M. S. Structural and Chemical Trends in Doped Silicon Nanocrystals: First-Principles Calculations. *Phys. Rev. B* **2005**, *71* (24), 245308.

(26) Lopez, T.; Mangolini, L. On the Nucleation and Crystallization of Nanoparticles in Continuous-Flow Nonthermal Plasma Reactors. *J. Vac. Sci. Technol. B* **2014**, *32* (6), 61802.

(27) Mangolini, L.; Thimsen, E.; Kortshagen, U. High-Yield Plasma Synthesis of Luminescent Silicon Nanocrystals. *Nano Lett.* **2005**, *5* (4), 655–659.

(28) Chen, S.; Coleman, D.; Abernathy, D. L.; Banerjee, A.; Daemen, L. L.; Mangolini, L.; Li, C. W. Giant Low-Temperature Anharmonicity in Silicon Nanocrystals. *Phys. Rev. Mater.* **2020**, *4* (5), 56001.

(29) Huq, A.; Kirkham, M.; Peterson, P. F.; Hodges, J. P.; Whitfield, P. S.; Page, K.; Hugle, T.; Iverson, E. B.; Parizzi, A.; Rennich, G. POWGEN: Rebuild of a Third-Generation Powder Diffractometer at the Spallation Neutron Source. *J. Appl. Crystallogr.* **2019**, *52* (5), 1189–1201.

(30) Taylor, J.; Arnold, O.; Bilheaux, J.; Buts, A.; Campbell, S.; Doucet, M.; Draper, N.; Fowler, R.; Gigg, M.; Lynch, V.; Markvardsen, A.; Palmen, K.; Parker, P.; Peterson, P.; Ren, S.; Reuter, M.; Savici, A.; Taylor, R.; Tolchenov, R.; Whitley, R.; Zhou, W, J. *Mantid, A High Performance Framework for Reduction and Analysis of Neutron Scattering Data*; 2012.

(31) Hubbard, C. R.; Swanson, H. E.; Mauer, F. A. A Silicon Powder Diffraction Standard Reference Material. *J. Appl. Crystallogr.* **1975**, *8* (1), 45–48.

(32) Hom, T.; Kiszenik, W.; Post, B. Accurate Lattice Constants from Multiple Reflection Measurements. II. Lattice Constants of Germanium Silicon, and Diamond. *J. Appl. Crystallogr.* **1975**, *8* (4), 457–458.

Chapter 6

Trivial Modifications of Acoustic Phonon Group Velocity in Lightly Cr-doped and Lightly Ti-doped Sapphires

6.1 Abstract

Phonon dynamics play an important role in the thermal transport of materials. Modifying phonon dynamics will provide tremendous opportunities for manipulating materials' properties and expanding materials' applications, however, phonon engineering in bulk systems has been challenging without substantial modifications of materials' chemical and mechanical properties. We measured transverse acoustic phonon group velocities of lightly Cr-doped and Ti-doped sapphires using inelastic neutron scattering to investigate the effects of small concentrations of dopants on the phonon dynamics of materials. Our results show trivial modifications of acoustic phonon group velocity in sapphire along [0 0 1] direction near the Brillouin zone centers from small concentrations of Cr and Ti dopants. Our results shed light on phonon engineering in bulk systems and will benefit further investigations about the dopant effect on phonon dynamics in crystalline systems.

6.2 Introduction

Thermal conductivity is a very important physical property of materials and is closely related to their applications. Materials with low thermal conductivity, which are good candidates for thermal barrier coatings and thermoelectric applications, are desirable to alleviate the global energy crisis and improve operating efficiencies in energy.[1–3] On the other hand, materials with high thermal conductivity are extremely useful and bear great potential for high-efficiency thermal interface and thermal management applications.[4–9] In addition, materials with tunable thermal conductivity can be used as highly efficient thermal energy storage to answer energy conservation and environmental protection issues for humanity.[10]

Lattice (phonon) thermal conductivity is proportional to heat capacity, phonon velocity, and phonon mean free path. Previous works show phonon mean free path can be controlled by controlling phonon-boundary scattering, making complex structures, creating nanostructures, and other methods which can control phonon scattering cross sections and rates.[11–13] On the other hand, directly controlling phonon group velocity, especially for acoustic phonon modes whose group velocities are normally larger than those of optical phonon modes, is more challenging and the corresponding approach is relatively limited. Reductions of acoustic phonon group velocity were observed in open-frame structures with guest insertions (rattlers) which can also alter other physical properties such as the heat capacity of materials, and nanostructures whose thermal-related applications are limited.[12,14–16]

Surprisingly, a recent work reported large reductions of acoustic phonon group velocities in lightly Nd-doped bulk sapphires using Brillouin light scattering.[17] In this chapter, to better understand phonon engineering in the bulk system, we measured transverse acoustic (TA) phonon energies of pristine and doped sapphires with inelastic neutron scattering and observed trivial modifications of TA phonon group velocity along [0 0 1] direction near the Brillouin zone center of lightly Cr-doped and lightly Ti-doped bulk sapphire.

6.3 Materials and methods

Undoped, lightly Ti-doped, and lightly Cr-doped sapphire samples were synthesized using Verneuil mothed.[18] The nominal dopant concentrations of lightly Cr-doped and lightly Ti-doped sapphires are 0.1% and 0.4%, respectively.

Inelastic neutron scattering measurements were performed on the Cold Neutron Triple-Axis Spectrometer (CTAX), a conventional cold neutron triple-axis spectrometer with variable incident energy and sample-analyzer distances at Oak Ridge National Laboratory. The undoped and the lightly Ti-doped sapphire samples were oriented at [1 0 -2] direction. Their TA phonon spectra were measured at [1 0 -1.93], [1 0 -1.925], [1 0 -1.92], [1 0 -1.915], [1 0 -1.91], [1 0 -1.905], and [1 0 -1.9] along [0 0 1] direction near the Brillouin zone at room temperature with the final energy of 4 meV and energy step size of 0.2 meV. The Cr-doped sample was oriented at [-1 0 2] direction. Its TA phonon spectra were measured at [-1 0 1.93], [-1 0 1.925], [-1 0 1.92], [-1 0 1.915], [-1 0 1.91], [-1 0 1.905], and [-1 0 1.9] at room temperature with the same energy setups.

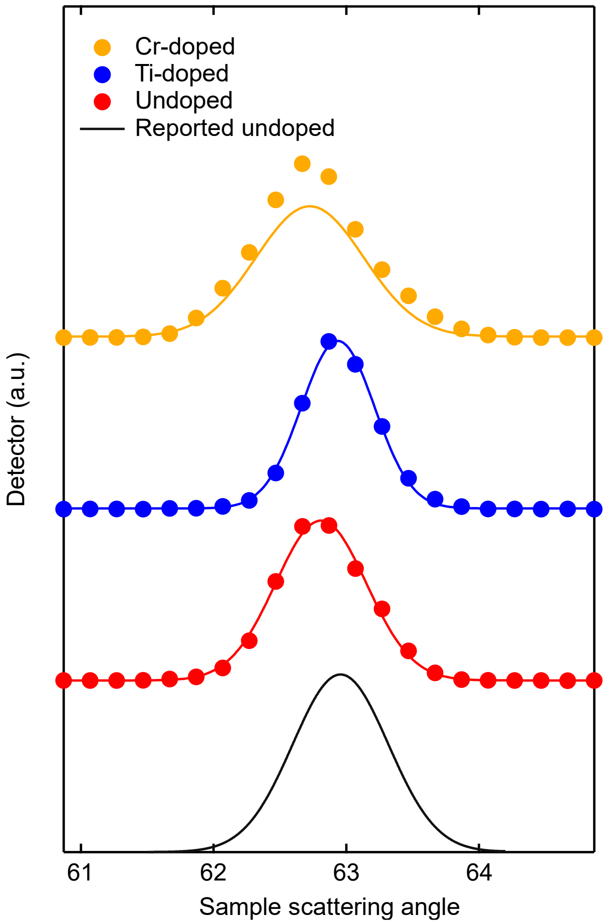

Figure 6.1 Neutron diffraction of (0 0 6) planes of our samples and the reported diffraction pattern of the pristine sapphire (ICSD #63647) for comparison.

Figure 6.1 shows neutron diffraction spectra of (0 0 6) planes of our samples as well as the reported diffraction spectrum measured by X-ray scattering.[19] The lattice parameters were extracted from the diffraction spectra using Bragg's law:

$$d = \frac{\lambda}{2Sin(\theta)} \tag{6.1}$$

$$\lambda = \frac{h}{mv}$$

Where λ, θ, h, m, and v are neutron wavelength, sample scattering angle, Planck's constant, the mass of a neutron, and speed of neutron, respectively. The differences among the measured lattice parameters of our samples are less than 0.2%. Such slight inconsistencies likely come from the instrument resolution.

6.4 Data processing

The event data of CTAX measurement contains information about the energies of the incident and scattered neutrons, the scattering geometry, and the number of scattered neutrons that reach the detector for each given number of incident neutrons. The energy (E) transfers of neutrons correspond to phonon energy profiles, while the scattering geometries contain the information of the momentums (q) of phonon modes. The phonon energy at each q point was determined by fitting the resolution-function-convoluted theoretical cross section to the experimental data S(q, E) with an iterative method. The resolution function was calculated from the shapes and dimensions of the source, monochromator, sample, analyzer, and detector, as well as the Soller collimators, the mosaic spread of monochromator and analyzer crystals with the Cooper-Nathans approximation.[20,21]

Figure 6.2 shows interpolated phonon spectra of undoped, lightly Cr-doped, and lightly Ti-doped sapphire samples. The phonon spectra were corrected by the Phonopy-calculated coherent one-phonon dynamic structure factors (at 300 K) at each measured q point and normalized, as discussed in the following section. Elastic intensities were removed below 1 meV.

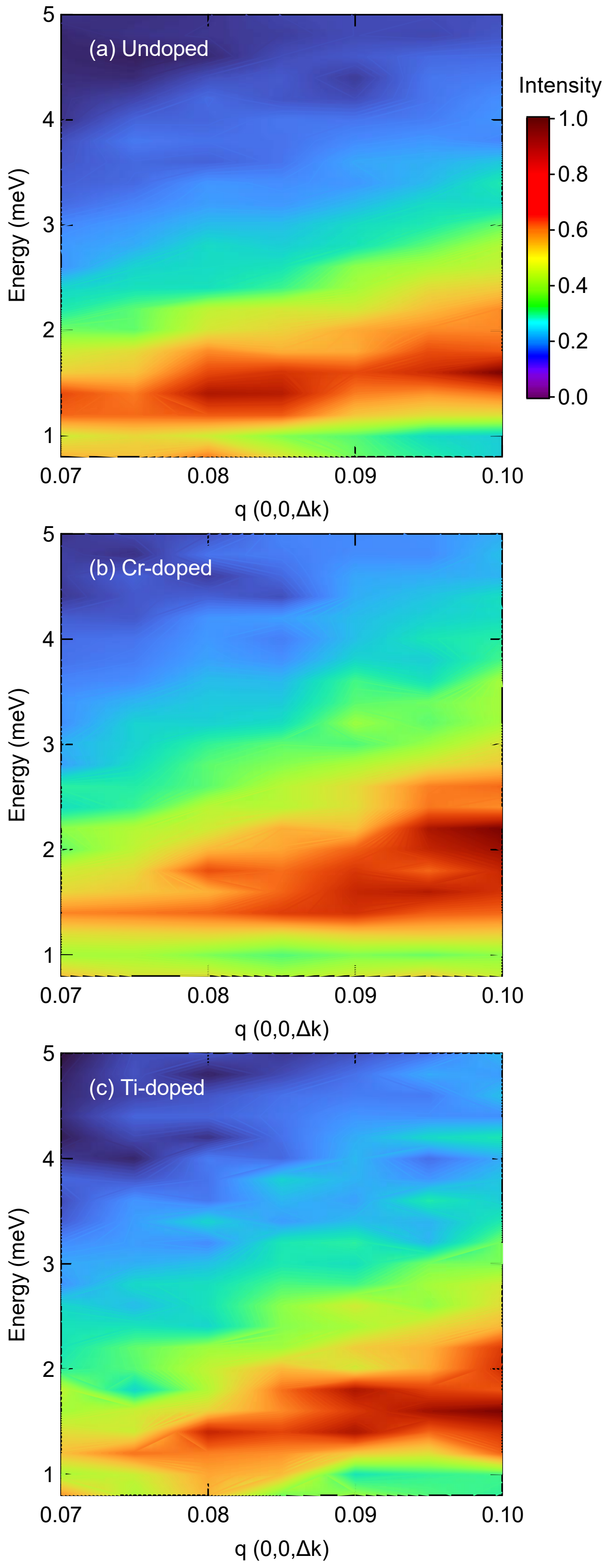
(a) Undoped
Intensity
1.0
0.8
0.6
0.4
0.2
0.0
Energy (meV)
5
4
3
2
1
0.07
0.08
0.09
0.10
q (0,0,Δk)
(b) Cr-doped
Energy (meV)
5
4
3
2
1
0.07
0.08
0.09
0.10
q (0,0,Δk)
(c) Ti-doped
Energy (meV)
5
4
3
2
1
0.07
0.08
0.09
0.10
q (0,0,Δk)

Figure 6.2 (a-c) Normalized TA phonon spectra in [0 0 1] direction of undoped, Cr-doped, and Ti-doped sapphire samples measured by inelastic neutron scattering at room temperature. The signal intensity at each q point was corrected with the DFT calculated dynamic structure factor.

6.5 Calculation

The TA phonon dispersion, the coherent one-phonon dynamic structure factors, and the mode isothermal Grüneisen parameters of pristine sapphire were calculated along [0 0 1] direction using VASP and Phonopy based on DFT with GGA projector augmented wave potential and quasi-harmonic approximation (QHA).[22,23] In DFT calculation, a 2 × 2 × 1 relaxed α-Al_2O_3 ($R\bar{3}c$) supercell was used as a model to calculate force sets, from which a dynamical matrix was computed. Phonon dispersion of the pristine silicon was calculated from the dynamical matrix along [0 0 1] direction. The coherent one-phonon dynamic structure factors were calculated at 300 K using 3.449 Å and 5.803 Å as the scattering lengths of aluminum and oxygen, respectively. The mode isothermal Grüneisen parameters were obtained from DFT calculations with QHA on smaller and larger unit cells with 1% differences in lattice parameters.

6.6 Result and discussion

The measured phonon spectra of the undoped, lightly Cr-doped, and lightly Ti-doped sapphire samples agree well with their resolution-function-convoluted theoretical cross section fits at all the measured points along [0 0 1] direction in the reciprocal space, as shown in Figure 6.3. It is observed that the fitted phonon energy increases in a linear manner with increasing phonon wavevector for all three samples. Such phonon behaviors are expected because the measurements were carried out close to the Brillouin zone centers, where phonon dispersions are supposed to be linear, of sapphire samples.

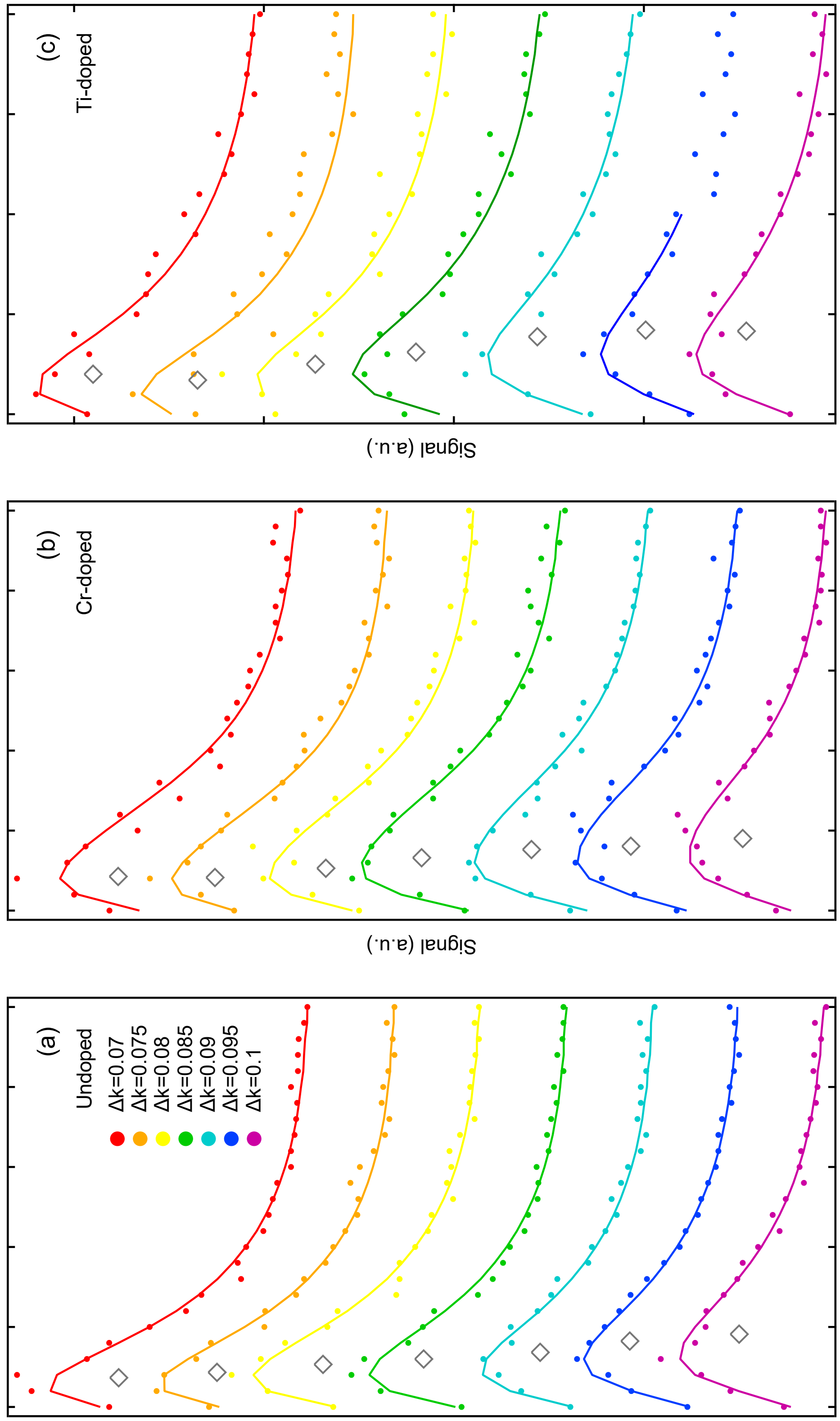
(a)
Undoped
Δk=0.07
Δk=0.075
Δk=0.08
Δk=0.085
Δk=0.09
Δk=0.095
Δk=0.1
(b)
Cr-doped
(c)
Ti-doped
Signal (a.u.)
Energy (meV)
1
2
3
4
5
6

Figure 6.3 The experimentally measured phonon spectra along [0 0 1] direction (colored dots) and their resolution-function-convoluted theoretical cross section fits (colored lines) of the undoped (a), Cr-doped (b), and Ti-doped (c) sapphire samples. The fitted phonon energies at different phonon wavevectors are illustrated with grey markers.

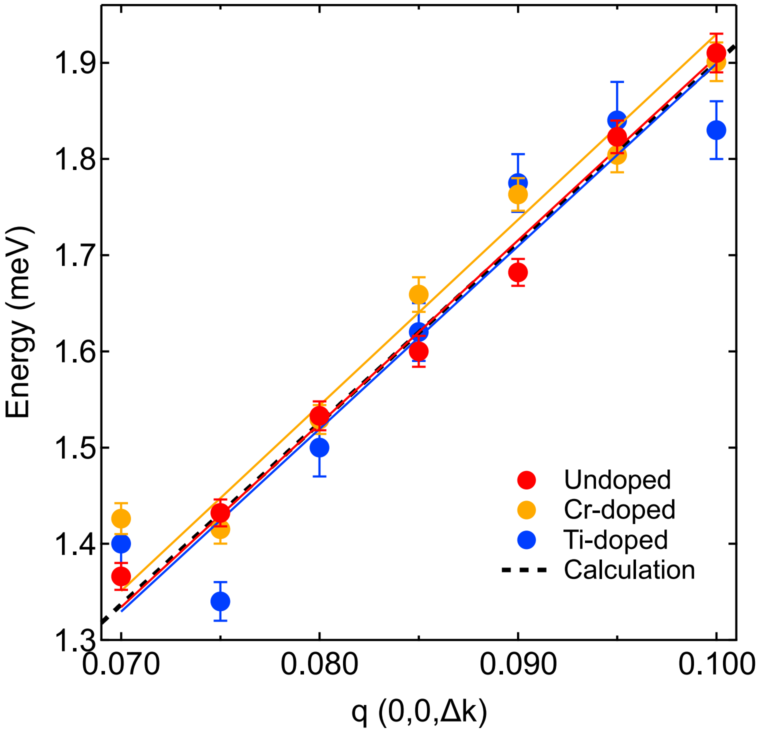

Figure 6.4 (a) The fitted phonon energies (colored markers) near Brillouin zone centers along [0 0 1] direction of the undoped, Cr-doped, and Ti-doped sapphire samples. The error bars show fitting uncertainties. The colored lines are linear fits to the phonon energies. The black dash line shows the DFT calculated TA phonon dispersion of sapphire.

The phonon dispersions near Brillouin zone centers along [0 0 1] direction of the undoped, lightly Cr-doped, and lightly Ti-doped sapphire samples were obtained by fitting the phonon energies with linear functions, as shown in Figure 6.4. The fitted phonon dispersions of all three samples are similar to each other. We extract phonon group velocities from the fitted phonon dispersions using:

$$v = \frac{E}{q} \tag{6.1}$$

where E and q are phonon energy and phonon wavevector, respectively. The extracted phonon group velocity of the undoped sapphire sample agrees with the previously measured values, which confirms the accuracy of our measurements and the viability of our analysis method.[24,25] The differences among the phonon group velocities are smaller than 2%, as shown in Table 6.1, which likely comes from measurement uncertainties and fitting errors. Such small differences in phonon dispersion indicate that the small concentrations of Cr and Ti dopants do not have substantial effects on the phonon dynamics near Brillouin zone centers along [0 0 1] direction in sapphire. This dopant effect is also expected to be small in the whole Brillouin zone. In addition, the fitted phonon dispersion of the undoped sapphire sample also has similar profiles to the DFT calculated TA phonon dispersion of undoped sapphire. Such similarity further shows the accuracy of our measurements and confirms that the phonon spectra from our measurements are TA phonon signals.

TABLE 6.1. Fitted phonon group velocities from the experimental data of the undoped, lightly Cr-doped, and lightly Ti-doped sapphire samples.

Sapphire sample	Fitted phonon group velocity (m/s)
Undoped	6040 ± 30
Lightly Cr-doped	6110 ± 60
Lightly Ti-doped	6010 ± 90

Unlike the previously reported huge decrease in the TA phonon energy of sapphire caused by small concentrations of Nd dopant,[17] our measurements show no significant changes in the TA phonon energy in lightly Cr-doped and lightly Ti-doped sapphire, as shown in Figure 6.5. Such discrepancies may come from the different dopant sizes and masses in sapphire samples. In contrast to Nd, whose ionic radius and atomic mass are about 2 times and 6 times larger than those of Al, respectively, the Cr^{3+} and Ti^{3+} are less than 2 times heavier than Al^{3+} and have similar ionic radius to that of Al^{3+}. In addition, previous studies show the Cr defect in sapphire is likely to be only substitutional and can not significantly distort the lattice.[26–28] This result in the small effect of Cr dopant on the phonon dynamics of sapphire as observed from our result. On the other hand, even though the Ti defect in sapphire can be both substitutional and interstitial and the unit cell of Ti_2O_3 is about 13% bigger than that of sapphire,[29–31] the low concentration of the Ti dopant likely cannot substantially distort the long-range lattice structure, which is closely related to phonon dynamics close to Brillouin zone centers. As a result, the low concentration of Ti dopant likely also has a small effect on the phonon dynamics near the Brillouin zone centers of sapphire, which agrees with our observations, as shown in Figure 6.4.

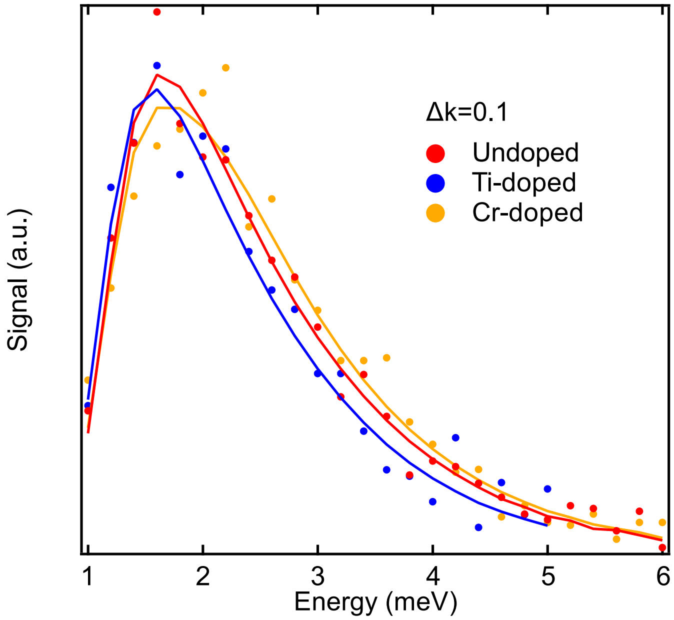

Figure 6.5 A direction comparison of the experimental phonon spectra and their resolution-function-convoluted theoretical cross section fits of the undoped, Cr-doped, and Ti-doped sapphire samples at q = 0.1.

6.7 Conclusion

We measured transverse acoustic phonon group velocities of lightly Cr-doped and Ti-doped sapphires using inelastic neutron scattering to investigate the effects of small concentrations of dopants on the phonon dynamics of materials. Our results show similar phonon behaviors along [0 0 1] direction near the Brillouin zone centers in all three of our sapphire samples likely because of the small concentrations of Cr and Ti dopants. Our results will benefit further investigations about the dopant effect on phonon dynamics as well as phonon engineering in bulk systems

6.8 References

(1) Klemens, P. G.; Gell, M. Thermal Conductivity of Thermal Barrier Coatings. *Mater. Sci. Eng. A* **1998**, *245* (2), 143–149.

(2) Clarke, D. R. Materials Selection Guidelines for Low Thermal Conductivity Thermal Barrier Coatings. *Surf. Coatings Technol.* **2003**, *163–164*, 67–74.

(3) Wood, C. Materials for Thermoelectric Energy Conversion. *Reports Prog. Phys.* **1988**, *51* (4), 459–539.

(4) Shahil, K. M. F.; Balandin, A. A. Graphene–Multilayer Graphene Nanocomposites as Highly Efficient Thermal Interface Materials. *Nano Lett.* **2012**, *12* (2), 861–867.

(5) Li, M.; Xiao, Y.; Zhang, Z.; Yu, J. Bimodal Sintered Silver Nanoparticle Paste with Ultrahigh Thermal Conductivity and Shear Strength for High Temperature Thermal Interface Material Applications. *ACS Appl. Mater. Interfaces* **2015**, *7* (17), 9157–9168.

(6) QU, X.; ZHANG, L.; WU, M.; REN, S. Review of Metal Matrix Composites with High Thermal Conductivity for Thermal Management Applications. *Prog. Nat. Sci. Mater. Int.* **2011**, *21* (3), 189–197.

(7) Ghosh, S.; Calizo, I.; Teweldebrhan, D.; Pokatilov, E. P.; Nika, D. L.; Balandin, A. A.; Bao, W.; Miao, F.; Lau, C. N. Extremely High Thermal Conductivity of Graphene: Prospects for Thermal Management Applications in Nanoelectronic Circuits. *Appl. Phys. Lett.* **2008**, *92* (15), 151911.

(8) Chen, H.; Ginzburg, V. V; Yang, J.; Yang, Y.; Liu, W.; Huang, Y.; Du, L.; Chen, B. Thermal Conductivity of Polymer-Based Composites: Fundamentals and Applications. *Prog. Polym. Sci.* **2016**, *59*, 41–85.

(9) Hussain, A. R. J.; Alahyari, A. A.; Eastman, S. A.; Thibaud-Erkey, C.; Johnston, S.; Sobkowicz, M. J. Review of Polymers for Heat Exchanger Applications: Factors Concerning Thermal Conductivity. *Appl. Therm. Eng.* **2017**, *113*, 1118–1127.

(10) Lin, Y.; Jia, Y.; Alva, G.; Fang, G. Review on Thermal Conductivity Enhancement, Thermal Properties and Applications of Phase Change Materials in Thermal Energy Storage. *Renew. Sustain. Energy Rev.* **2018**, *82*, 2730–2742.

(11) Toberer, E. S.; Zevalkink, A.; Snyder, G. J. Phonon Engineering through Crystal Chemistry. *J. Mater. Chem.* **2011**, *21* (40), 15843–15852.

(12) Balandin, A. A. Nanophononics: Phonon Engineering in Nanostructures and Nanodevices. *Journal of Nanoscience and Nanotechnology*. pp 1015–1022.

(13) Hosseini, S. A.; Davies, A.; Dickey, I.; Neophytou, N.; Greaney, P. A.; de Sousa Oliveira, L. Super-Suppression of Long Phonon Mean-Free-Paths in Nano-Engineered Si Due to Heat Current Anticorrelations. *Mater. Today Phys.* **2022**, 100719.

(14) Christensen, M.; Abrahamsen, A. B.; Christensen, N. B.; Juranyi, F.; Andersen, N. H.; Lefmann, K.; Andreasson, J.; Bahl, C. R. H.; Iversen, B. B. Avoided Crossing of Rattler Modes in Thermoelectric Materials. *Nat. Mater.* **2008**, *7* (10), 811–815.

(15) Zebarjadi, M.; Esfarjani, K.; Yang, J.; Ren, Z. F.; Chen, G. Effect of Filler Mass and Binding on Thermal Conductivity of Fully Filled Skutterudites. *Phys. Rev. B* **2010**, *82* (19), 195207.

(16) Chen, S.; Coleman, D.; Abernathy, D. L.; Banerjee, A.; Daemen, L. L.; Mangolini, L.; Li, C. W. Giant Low-Temperature Anharmonicity in Silicon Nanocrystals. *Phys. Rev. Mater.* **2020**, *4* (5), 56001.

(17) Kargar, F.; Penilla, E. H.; Aytan, E.; Lewis, J. S.; Garay, J. E.; Balandin, A. A. Acoustic Phonon Spectrum Engineering in Bulk Crystals via Incorporation of Dopant Atoms. *Appl. Phys. Lett.* **2018**, *112* (19), 191902.

(18) Dobrovinskaya, E. R.; Lytvynov, L. A.; Pishchik, V. *Sapphire: Material, Manufacturing, Applications*, 1st ed.; Springer Publishing Company, Incorporated, 2009.

(19) Cooper, A. S. Precise Lattice Constants of Germanium, Aluminum, Gallium Arsenide, Uranium, Sulphur, Quartz and Sapphire. *Acta Crystallogr.* **1962**, *15* (6), 578–582.

(20) Cooper, M. J.; Nathans, R. The Resolution Function in Neutron Diffractometry. I. The Resolution Function of a Neutron Diffractometer and Its Application to Phonon Measurements. *Acta Crystallogr.* **1967**, *23* (3), 357–367.

(21) Chesser, N. J.; Axe, J. D. Derivation and Experimental Verification of the Normalized Resolution Function for Inelastic Neutron Scattering. *Acta Crystallogr. Sect. A* **1973**, *29* (2), 160–169.

(22) Kresse, G.; Furthmüller, J. Efficiency of Ab-Initio Total Energy Calculations for Metals and Semiconductors Using a Plane-Wave Basis Set. *Comput. Mater. Sci.* **1996**, *6* (1), 15–50.

(23) Togo, A.; Tanaka, I. First Principles Phonon Calculations in Materials Science. *Scr. Mater.* **2015**, *108*, 1–5.

(24) Rösch, F.; Weis, O. Phonon Transmission from Incoherent Radiators into Quartz, Sapphire, Diamond, Silicon and Germanium within Anisotropic Continuum Acoustics. *Zeitschrift für Phys. B Condens. Matter* **1977**, *27* (1), 33–46.

(25) Hao, H.-Y.; Maris, H. J. Dispersion of the Long-Wavelength Phonons in Ge, Si, GaAs, Quartz, and Sapphire. *Phys. Rev. B* **2001**, *63* (22), 224301.

(26) Heuer, A. H. Oxygen and Aluminum Diffusion in α-Al2O3: How Much Do We Really Understand? *J. Eur. Ceram. Soc.* **2008**, *28* (7), 1495–1507.

(27) Na-Phattalung, S.; Limpijumnong, S.; T-Thienprasert, J. First-Principles Study of Chromium Defects in α-Al2O3: The Origin of Red Color in Ruby. *Phys. status solidi* **2020**, *257* (9), 2000159.

(28) Xiang, X.; Zhang, G.; Yang, F.; Peng, X.; Tang, T.; Shi, Y.; Wang, X. An Insight to the Role of Cr in the Process of Intrinsic Point Defects in α-Al2O3. *Phys. Chem. Chem. Phys.* **2016**, *18* (9), 6734–6741.

(29) Lacovara, P.; Esterowitz, L.; Kokta, M. Growth, Spectroscopy, and Lasing of Titanium-Doped Sapphire. *IEEE J. Quantum Electron.* **1985**, *21* (10), 1614–1618.

(30) Abrahams, S. C. Magnetic and Crystal Structure of Titanium Sesquioxide. *Phys. Rev.* **1963**, *130* (6), 2230–2237.

(31) ROY, S. K.; COBLE, R. L. Solubilities of Magnesia, Titania, and Magnesium Titanate in Aluminum Oxide. *J. Am. Ceram. Soc.* **1968**, *51* (1), 1–6.

Chapter 7

Conclusions and future work

Phonon engineering makes it possible for people to manipulate materials' physical and mechanical properties for broader applications and has drawn an increasing amount of attention during the past decades. Within this dissertation, the phonon dynamics as a function of intrinsic and extrinsic effects in silicon nanocrystals and bulk sapphire were deeply investigated using neutron scattering techniques. We found that phonon dynamics in the silicon nanocrystals are greatly different from that in bulk silicon due to structure variations inside nanocrystal systems and can be controlled more easily. On the other hand, the challenge of phonon engineering in bulk systems, such as bulk sapphire in this dissertation, is non-trivial. Even though a more than 10% energy decrease of transverse acoustic (TA) phonon modes was reported in lightly Nd-doped sapphire, our study shows lightly Cr-doped and lightly Ti-doped sapphire likely have similar phonon dynamic profiles to that of their undoped counterparts due to the small modifications of crystalline structure.

Chapter 2 discussed the large particle size effect and the temperature effect on the phonon dynamics of 4 – 7.4 nm spherical silicon nanocrystals as a result of their structure variations. Such large modifications to the phonon dynamics lead to a giant phonon anharmonicity in small-sized silicon nanocrystals at low temperatures. In addition, the TA phonon dispersions near the Brillouin zone centers in silicon nanocrystals were found to be non-linear and disobey the Debye model that works for bulk silicon.

Chapter 3 talked about the oxidation effect as well as the particle size and the temperature effects on bigger-sized silicon nanocrystals. TA phonon dynamics, which are closely related to long-range atomic structures, were found to be much more dependent on these effects compared to optical phonon modes. As a result, a relatively large difference between the vibrational entropy per atom of the silicon nanocrystal and the bulk silicon systems was observed at the intermediate temperature compared to those under higher and lower temperatures.

Extending this study, Chapter 4 goes into the investigation of the phonon dynamics in surface-functionalized silicon nanocrystals. The phonon dynamics in the 1-dodecene terminated 3-nm silicon nanocrystals were found to be heavily dominated by the hydrogen-related modes in the organic ligands thanks to the large neutron cross section and small atomic mass of hydrogen atoms. High-resolution inelastic x-ray scattering experiments, which can provide more information on heavier atoms, are desirable for further investigations into this subject. In addition, the photoluminescence experiments of our silicon nanocrystal samples are also desirable and will greatly benefit the study of the photoluminescent mechanism in spatially confined silicon systems.

The atomic structures of 3-nm silicon nanocrystals were discussed in Chapter 5. Anisotropic structure variations were observed in our samples. Unfortunately, the counting statistics were too low to provide any information on the temperature-induced lattice evolution in silicon nanocrystals, which is expected to be different from the bulk behaviors. Such an issue can be likely solved by using the Nanoscale-Ordered Materials Diffractometer at Oak Ridge National Laboratory in future experiments.

The attempt at phonon engineering in bulk systems using small concentrations of dopants was discussed in Chapter 6. However, we found that phonon engineering in bulk systems is rather challenging. Our results showed similar phonon behaviors in undoped, lightly Cr-doped, and lightly Ti-doped sapphire samples along [0 0 1] direction near the Brillouin zone centers. Inelastic neutron scattering measurements of phonon dynamics in light Nd-doped sapphire, which was reported to have modified acoustic phonon group velocities near the Brillouin zone centers, are desirable for a deeper understanding of phonon engineering in bulk systems.

Our works provide valuable information on phonon engineering in both spatially confined and bulk systems and will benefit further investigations into phonon-participated physical mechanisms, such as the elusive photoluminescence phenomenon in silicon nanocrystals, and the continuous development of advanced functional materials for better industrial performance and energy efficiency. We believe the topic of phonon engineering will remain attractive and its outcomes will make changes to people's lives in the future.